Theses and Dissertations

2011

# Flow Analysis in the Extrusion of Tellurite Glass Preforms for Enhanced Optical Fibers

Amit Ajit Belwalkar
*Lehigh University*

Follow this and additional works at: http://preserve.lehigh.edu/etd

**FLOW ANALYSIS IN THE EXTRUSION OF TELLURITE GLASS PREFORMS**

**FOR ENHANCED OPTICAL FIBERS**

by

# Amit Ajit Belwalkar

**Presented to the Graduate and Research Committee
of Lehigh University
in Candidacy for the Degree of
Doctor of Philosophy**

**in**

**Mechanical Engineering**

**Lehigh University**

**September 2011**

Approved and recommended for acceptance as a dissertation in partial fulfillment of the requirements for the degree of Doctor of Philosophy.

_____
Date

_____
Prof. Wojciech Misiolek,
Committee Chair and Dissertation Co-Advisor

_____
Accepted Date

**Committee Members**:

_____
Prof. Jean Toulouse, Dissertation Co-Advisor

_____
Prof. Jacob Kazakia

_____
Prof. Raymond Pearson

_____
Prof. Alparslan Oztekin

_____
Prof. John Coulter

_____
Prof. Andriy Kovalskyy

iii

# ACKNOWLEDGMENT

I would also like to acknowledge all IMF group members, past and present, for their terrific support. Special thanks to Yan Xu who taught me to operate DEFORM and just for being a great lab-mate. I would like to acknowledge Andrew Thome for his help with SEM and EDAX. I want to thank the technicians Mike Rex and Joe Zelinski for helping out with the tools fabrication. I thank Sam Laurence for helping me out not only with the optical microscopy but all the little things which made a big impact in the completion of this research.

I am profusely grateful to my parents, Ajit and Megha Belwalkar, for the love and support they have given me over the years. I am also thankful to my in-laws for being very supportive and providing steady encouragement. Finally, I would like to thank my wife Mugdha, without her love, support and understanding, this would not have been possible. Thanks so much for always being there for me and believing in me.

# TABLE OF CONTENTS

**TABLE OF CONTENTS**
**(Continued)**

# LIST OF TABLES

## LIST OF FIGURES

# Flow Analysis in the Extrusion of Tellurite Glass Preforms for Enhanced Optical Fibers

## Abstract

Tellurite glasses have excellent optical properties such as good transmission in the mid infrared, high linear and nonlinear refractive indices and physical properties such as good thermal and chemical stability and low temperature forming ability. All these makes tellurite glass an excellent candidate for the fabrication of fiber performs with a variety of geometric profiles which can be tailored to different optical applications, particularly nonlinear applications such as the development of ultra-broad laser sources based on supercontinuum generation. Towards such applications, various tube preforms with excellent surface quality were extruded from the tellurite glass $75TeO_2$-$20ZnO$-$5Na_2O$ (TZN-75) on our laboratory press. However, the presence of optical inhomogeneity in the form of "flow lines" (FL) was noticed in the cross-sections of the extruded preforms, which can be detrimental for optical applications because they can distort optical modes in fibers and contribute to losses through the scattering of light. A numerical model was developed to estimate the shear rate and shear stress distribution within the extrusion die, and determine the range of values that would produce extrudates free of these FLs. A theoretical flow analysis and dynamic and steady state shear tests were also performed and their results compared with those of the numerical simulation. An extrusion forming diagram of shear stress distribution for TZN-75 was developed showing the range of values of the extrusion parameters that would produce extruded preforms free of FLs. Such performs should result in fibers with much lower loss and better propagation characteristics.

# CHAPTER 1

## INTRODUCTION

Fiber optic systems have many attractive features that are superior to electrical systems in communication engineering. These features include greatly increased bandwidth and capacity which results in reduced size and weight, improved system performance, immunity to electrical noise, signal security, improved safety, electrical isolation, environmental protection, and overall system economy. For these advantages optical fiber has been very widely used in communication purposes such as cable TV, telephone and internet but the technology has continued to expand into many areas outside of communications including fiber-optics bundles for illumination and imaging, endoscopes to view inside the body and treat diseases with light and without surgery and optical sensors to measure rotation, pressure, sound waves, magnetic fields and many other quantities.
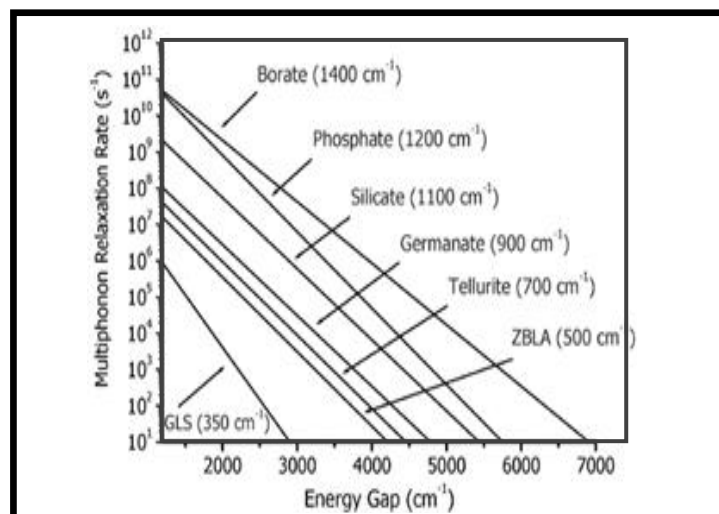


**Figure 1.1** Multi-phonon edge of different glasses

The fiber used in today's optical fiber technology is made from silica glass since the information loss per kilometer for the silica fiber is as low as 0.02 dB/km. Because of such a low loss, these fibers are ideal for intercontinental connections. Silica fibers have inherent high energy phonons, therefore usable rare-earth ions that are optically active for optical amplifications are limited in silica-based fibers. As shown in Figure 1.1, phonon energy for silica is 1100 cm$^{-1}$ while that for tellurite glass is about 700 cm$^{-1}$. Thus, heavy metal oxide glass fibers such as tellurite glass fibers demonstrate expanded amplification bandwidths as many rare-earth ions become optically active in them. Tellurite glasses also possess high rare-earth solubility and thus stronger and broader rare-earth emission [1] than silica glasses. Because of broader rare-earth emission and low phonon energy, $Er^{3+}$ tellurite glass fiber amplifiers were able to realize broadband operation [2]. The tellurite glass has higher linear refractive and much higher nonlinear index and other nonlinear coefficients [3] than silica. Because of the higher indices, the self-phase modulation spectrum (SPM) of the tellurite glass fiber exhibits small output peaks on both sides of the input signal (Figure 1.2) which are not observed in silica glass. This property is under investigation of their use in all optical switching.
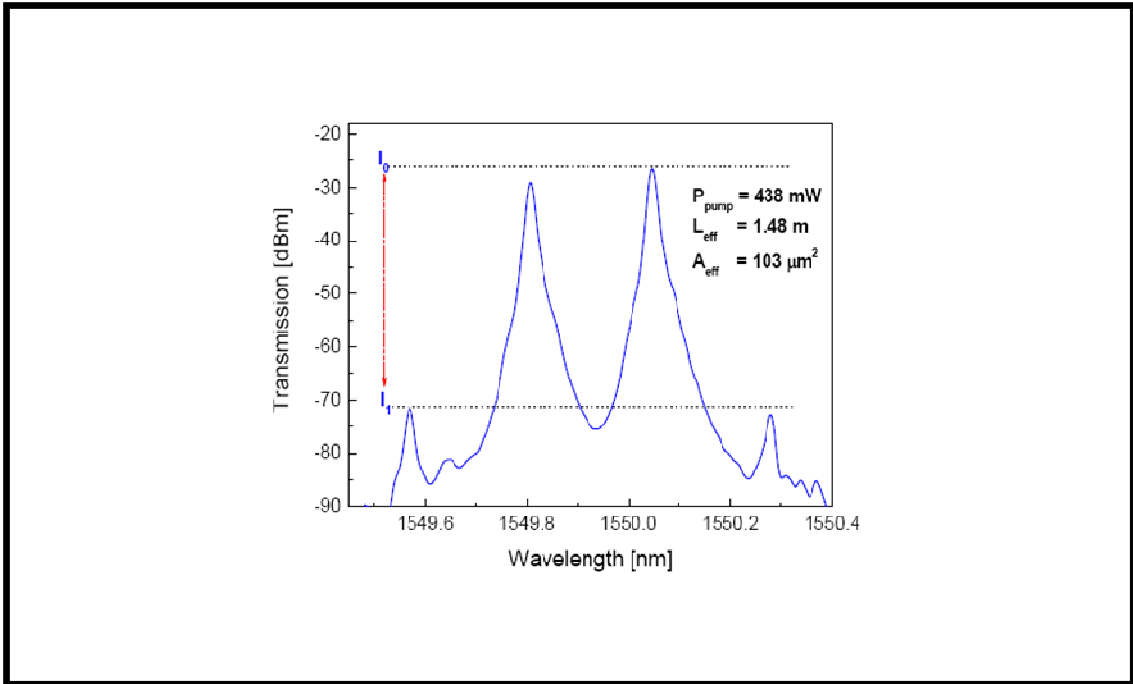
**Figure 1.2** Cw-SPM spectrum of TZN-80 fiber

But the most important optical property of the tellurite glass is good optical transmission in the mid-infrared. Tellurite glass as shown in Figure 1.3 demonstrates transmission up to 6.1 µm at 50% and up to 3 µm wavelength at 80% efficiency. This is much wider IR transmission window compared to silica which transmits light up to 2 µm wavelength.
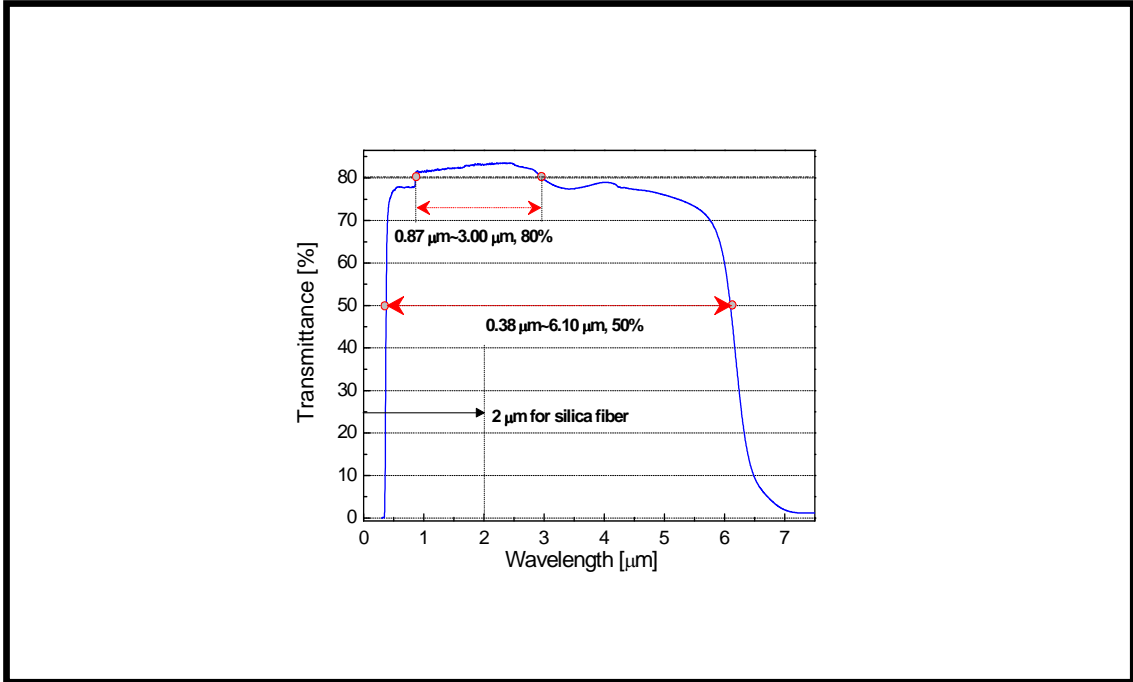
**Figure 1.3** UV-VIS FTIR transmission spectrum of $80TeO_2$-$10ZnO$-$10Na_2O$ (TZN-80)

Furthermore, tellurite glasses possess better thermal stability and chemical durability than the chalcogenide glasses that have been extensively investigated. Finally, because they are soft, tellurite glasses are easier to form than silica. These properties make tellurite glass particularly attractive for mid-IR fibers with a variety of geometries, solid core/clad and microstructured, which can be used in fiber lasers and amplifiers for optical communications or fiber sensors for environmental and bio-medical applications. Microstructured fibers containing air holes (holey fibers, HF) have attracted considerable attention recently because their geometry can be designed for desired dispersion and polarization properties, small confinement and enhanced nonlinearities, thus providing new functionalities compared to conventional core/cladding fibers [4]. Thus, HFs appear promising for a number of applications in areas such as all-optical applications (broad band sources, amplification, switching etc.) and power delivery. HFs are a single-

5

material-based novel type of fibers with air channels arranged in specific patterns surrounding a solid or air core and running through the entire length of the fiber. HF preforms can be made using several techniques such as capillary stacking, drilling and casting, but all of these have certain limitations.



(a)                    (b)                    (c)
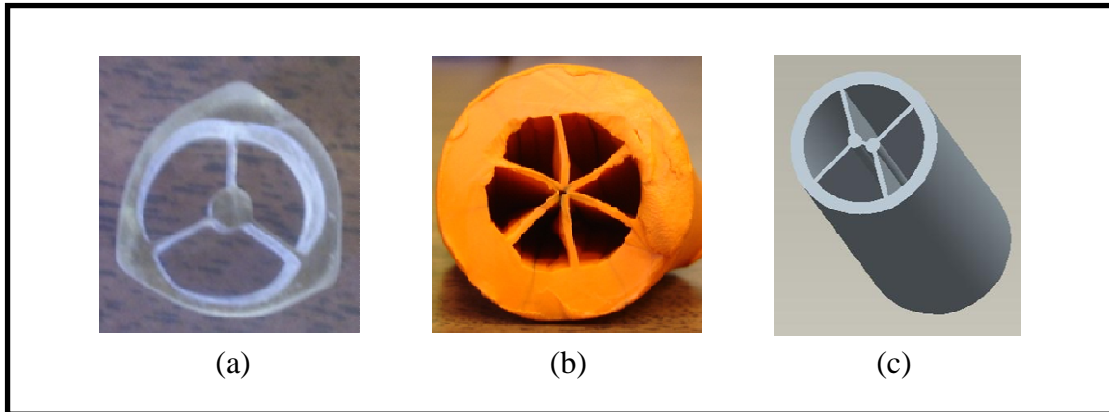
**Figure 1.4** Examples of Holey Fiber preforms with complex geometry profiles: (a) Extruded suspended core with three spokes (b) Suspended core with six spokes having circular outer wall and (c) Suspended double-core with four spokes

Suction or rotational casting techniques are limited to simple geometries. Capillary stacking is laborious and time consuming and presents reproducibility problems, while drilling is limited to relatively short preform lengths. By contrast, extrusion offers great flexibility in preform and, ultimately, fiber geometry. It is a one-step, reproducible and versatile process that can conveniently produce complex cross-sections of different sizes, shapes and cross section reductions. Extrusion is most suited to produce HF preforms with complex geometry to give better control over light propagation providing wide range of optical functionality. It is also favored over other bulk forming processes due to the advantageous state of stress when forming brittle materials like ceramics and glasses. Figure 1.4 exhibits different geometric profiles of HF

6

preforms designed in our lab. HF preform in Figure 1.4 (a) has been already developed into a fiber [5] while geometric profiles shown in Figure 1.4 (b) and (c) are under development.

Silica HFs have now been produced with a variety of geometries. However, silica does not transmit light past 2 μm wavelength and new glasses and fibers are needed for mid-IR applications. Little work has been done so far on soft glass HFs in general and even less on soft glass HFs produced by extrusion and they are now attracting growing interest [6]. Recently, a number of researchers successfully produced HF preforms of several glasses such as bismuth [7], SF6 [8], SF57 as well as tellurite-based glasses [9-11]. Hongsheng Xiao conducted extrusion experiments on various compositions of tellurite glass to fabricate jacketing tubes and HF performs for solid and suspended core fibers respectively. He established profile of the HF preform that was successfully drawn into fibers [12]. The overall goal in this project was to optimize extrusion process to make better quality extrudate preforms which when drawn into fibers would give fibers with greater optical performance. Extruded preforms with good physical attributes such as excellent surface quality and dimensional accuracy are shown in Figure 1.5. Dimensional accuracy depends on the extrusion parameters and is discussed in detail in Chapter 4.
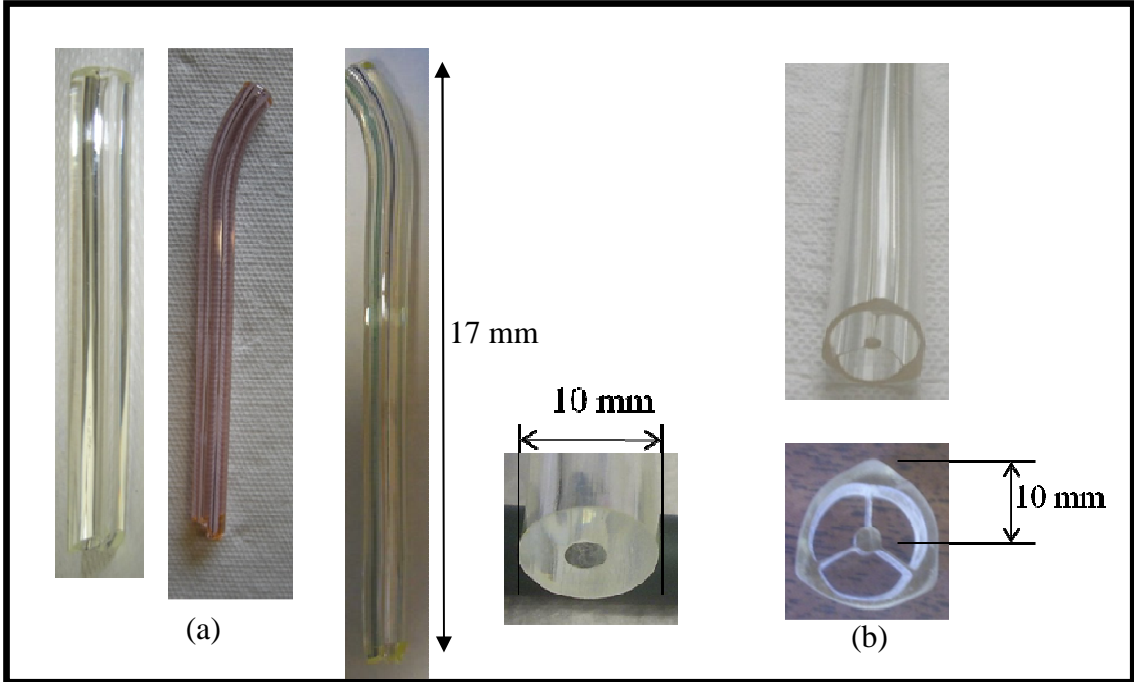
**Figure 1.5** Examples of (a) round tube and (b) holey fiber preforms exhibiting excellent surface quality

Cross-sectional images of the round tube and cladding preforms extruded between $10^6$~$10^7$ Pa.s viscosity at 0.003 mm/s ram speed is shown in Figure 1.6. Both images show optical inhomogeneities in the form of flow lines (FLs) or shear bands. These spatial inhomogeneities in the refractive index of the glass become visible because the light rays are transmitted at different angles due to the index variations, thus producing an optical contrast between the flow lines and rest o the glass in the preform. The details of the extrusion process are given in Chapter 2. Extrusion parameters and the flow lines are described in detail in Chapter 4.

10 mm

(a)

10 mm

(b)
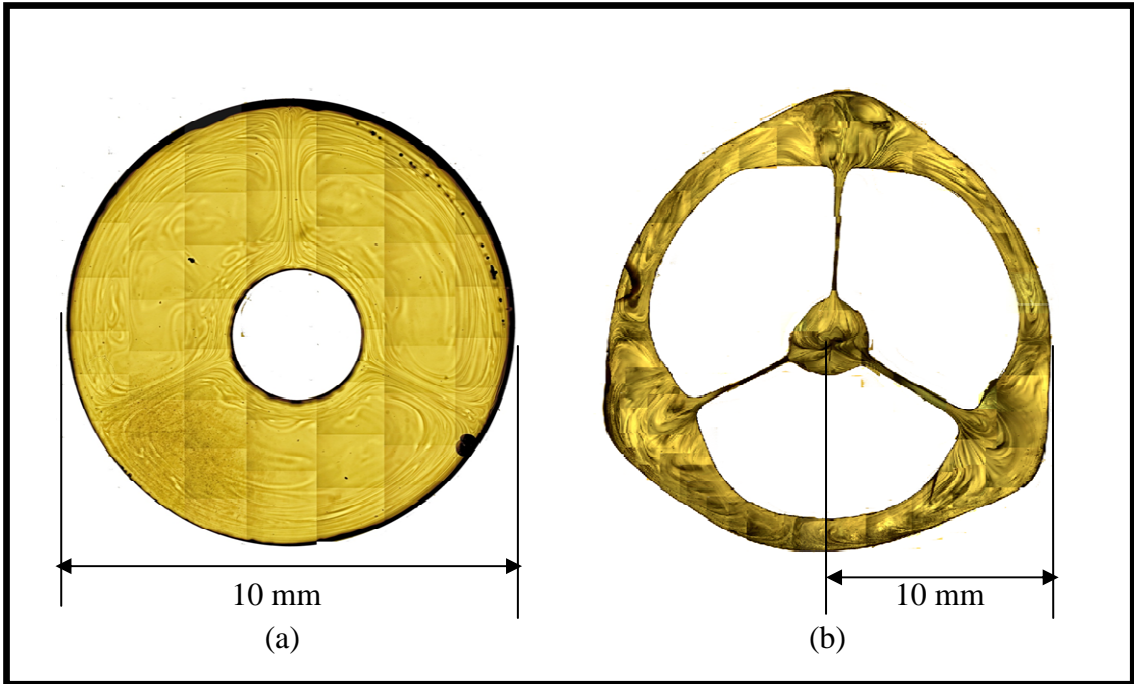
**Figure 1.6** Examples of (a) round tube and (b) holey fiber preforms exhibiting excellent surface quality

Although the preforms have excellent physical robustness and surface quality, they contain optical inhomogeneities in the form of flow lines. Note that they are not transferred directly from the billet to the extrudate but are introduced in the preform during the extrusion. Nonetheless, the optical inhomogeneities will be transferred into the fiber as seen in the Figure 1.7. Notice the flow lines in the cladding of the solid core fiber as indicated.
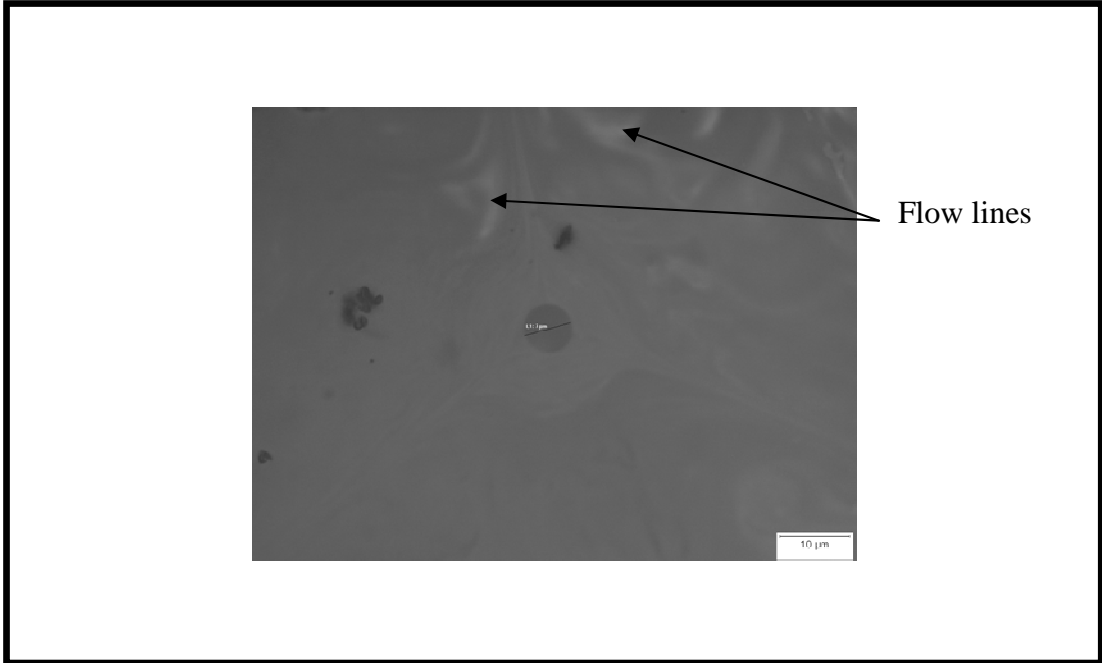
**Figure 1.7** Solid core fibers with the central core (dark) and cladding surrounding it. Flow lines are visible in the extruded cladding tube

If a laser light is transmitted through the fibers having such optical inhomogeneities, the light will be scattered. This was demonstrated by performing a pre-raman scattering experiment to measure the intensity of laser light diffracted from the billet and the extruded preform. Note that the preform was extruded from the same billet. The schematic of the experimental set up is shown in Figure 1.8 (a). In the experiment, a laser light is shone on the tellurite glass sample having optically polished surfaces 90° to each other.
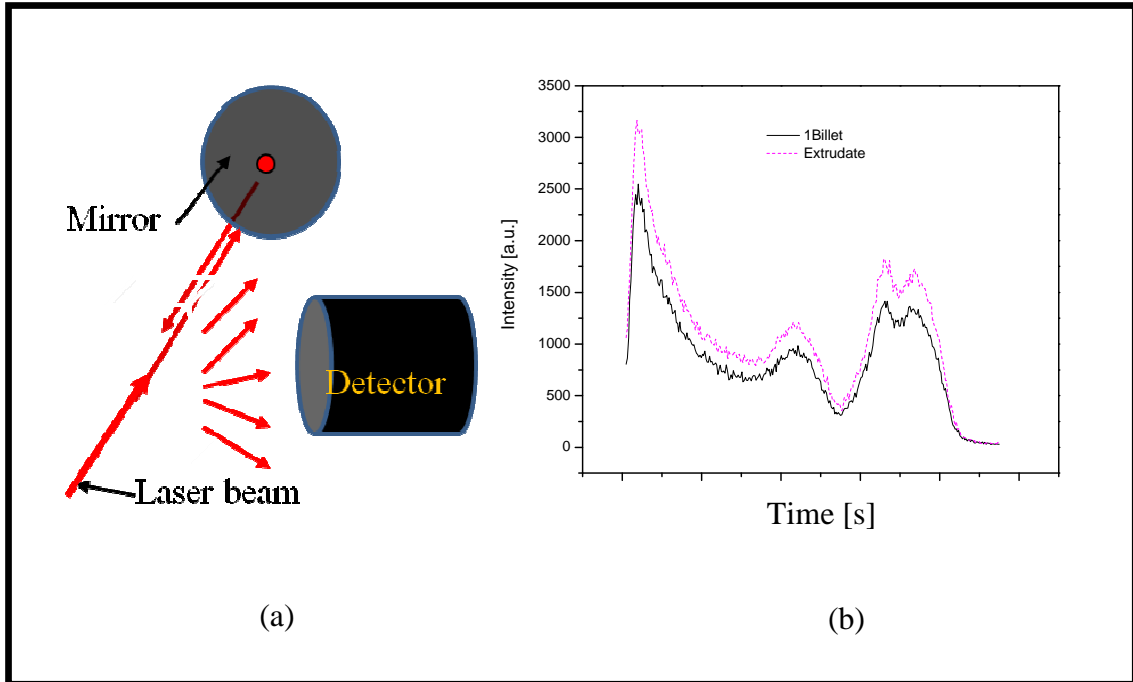
**Figure 1.8** (a) Experiment measuring scattered light intensity (b) Intensity measured by the detector as a function of time

The light was reflected back to the sample by a reflective mirror mounted on the opposite side. This mirror was adjusted in such a way that the reflected and transmitted lights were collinear to each other. The intensity of the scattered light was then measured by a detector and then plotted as a function of time shown in Figure 1.8 (b). The extruded preform having the optical inhomogeneities in the form of flow lines scattered more than the billet which had no flow lines.

Billet with no optical inhomogeneities (flow lines) scatter least amount of light and therefore has Gaussian modal shape having the highest intensity in the center of the laser beam as shown in Figure 1.9 (a). Conversely, the extruded preform scattered more light and modal shape does not remain Gaussian anymore as shown in Figure 1.9 (b).
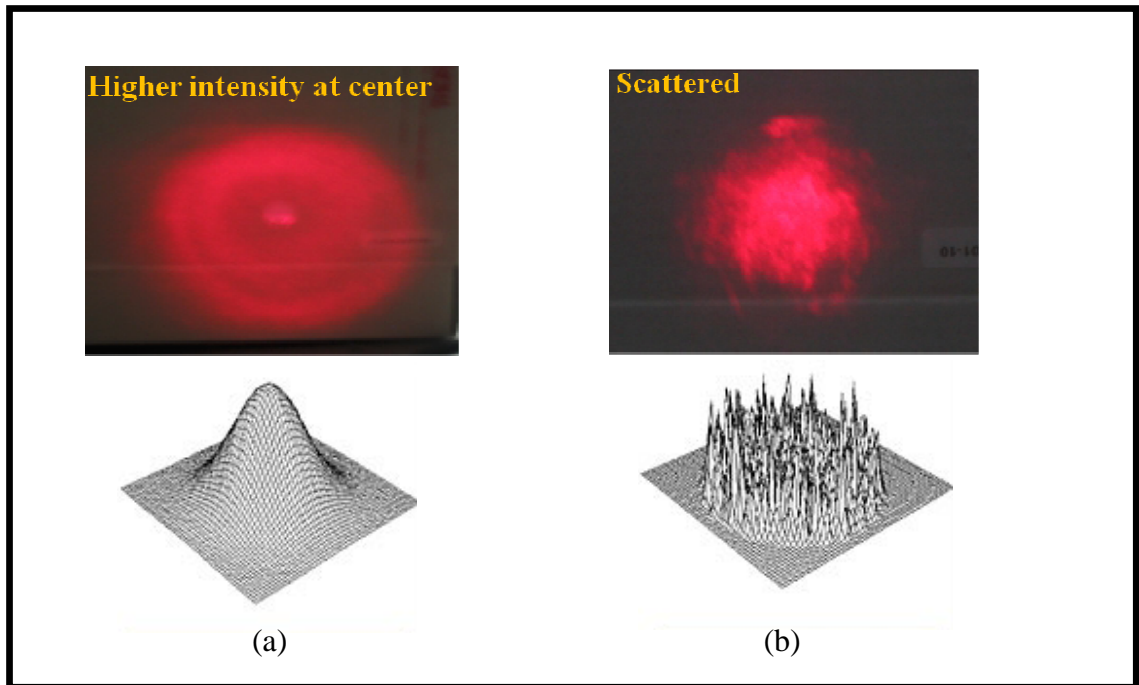
**Figure 1.9** Top (a) and (b) images are the images of the laser speckles on the mirror and bottom (a) and (b) are the mode shapes for the tellurite glass billet and extrudate respectively. Intensity of laser light diffracted by billet and extruded preform samples. Scattered light in the extrudate preform demonstrated broken mode shapes while the mode shape is continuous for billet having higher intensity in the center

Light intensity transmitting through the extrudate preform is distributed and not converged in the center of the beam. Therefore, all of the light would not be carried into the core but would be leaked out into the cladding. Thus the fiber would be inefficient in transmitting light due to these optical inhomogeneities in the form of flow lines and therefore need to be eliminated. More light would be transmitted through the preform and subsequently drawn fibers if the flow lines are minimized or eliminated. Thus, elimination of flow lines in the extruded preform is very important step toward having a low loss optical fiber.

## 1.1 Research Objective

Overall objective of this research was to fabricate tellurite glass optical cladding and holey fiber preforms having good optical homogeneity so that the subsequently made fibers from those preforms would provide improved optical performance in the fibers. After conducting several extrusion experiments, flow lines were discovered and concluded that the flow lines were the cause of light scattering which in turn could cause transmission losses in the fibers. Thus, the objective was narrowed down to the elimination of flow lines. To eliminate the flow lines, experimental optimization of the extrusion parameters was proposed. Rheological studies were proposed for the optimization of extrusion parameters; they would also be useful in developing a numerical model for the tellurite glass extrusion. For the numerical model, a simple case of steady, incompressible, viscous glass flow through a tapered extrusion die was considered (round tube and not the holey fiber preform). The model would be useful in determining the extrusion parameters at which flow lines being formed thus helping to determine the extrusion conditions which would provide preforms without flow lines. Preforms free of flow lines would be optically homogeneous and therefore provide fibers with improved optical performance.

## 1.2 Dissertation Structure

Chapter two will present background information on the processes involved in the fiber fabrication and glass extrusion. It will also discuss the structure and properties of tellurite glass. This will be followed by the introduction to the third, fourth and fifth chapter which covers the research conducted in this project. In chapter three, rheological

properties of tellurite glass through dynamic and steady shear measurements will be discussed. The information obtained via these measurements, will not only be helpful in the optimization of the extrusion parameters such as viscosity and shear rate to obtain better optical quality extruded preform but also helps in the numerical modeling of the glass extrusion discussed in the fifth chapter. Chapter 4 will discuss the results of the tellurite glass extrusion experiments conducted at different extrusion parameters to obtain optically homogeneous preforms. Chapter 5 will discuss the numerical modeling of the steady, incompressible, viscous flow of glass through tapered extrusion die. The model will provide information on the extrusion parameters to obtain extruded preforms free of flow lines. The dissertation will end with a detailed conclusion and future plan.

# CHAPTER 2

# BACKGROUND

## 2.1      Optical Fibers

Optical fibers are characterized by their structure and their properties of transmission. By transmission mode, optical fibers are classified into two types: single-mode and multi-mode. The basic structural difference between them is the core size. Structurally, they are classified into core/clad and micro-structured optical fibers. The most widely used optical fibers are made of glass and of a core-cladding structure, with the refractive index of the core being normally being higher than that of the cladding.
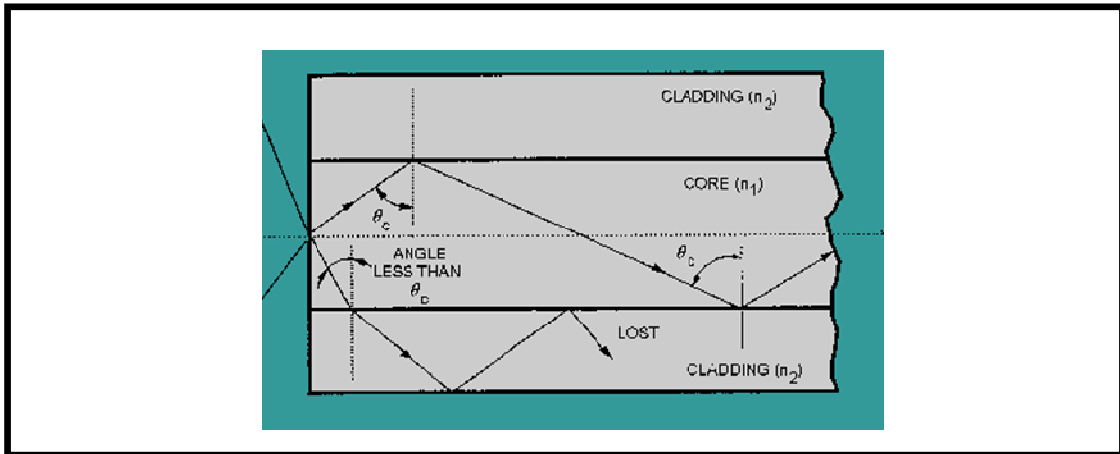


**Figure 2.1** Propagation of light along a fiber with a core-cladding structure [13]

Incident light from the core to the core-cladding interface will propagate along the fiber if the incident angle is greater than the critical angle of incidence $\theta_c$, and the light is

totally reflected back into the core. Critical angle is calculated as $\theta_c = n_2/n_1$ where $n_1$ and $n_2$ being the refractive indices of the core and the cladding respectively. When the incident angle is less than $\theta_c$, the incident light will be refracted and lost, not be able to propagate along the fiber, see Figure 2.1.

The overall objective of this research is to make tellurite glass optical fibers; so in the next two sections, the preparation of bulk tellurite glass and the fabrication of the tellurite glass optical fibers with core-cladding and holey structure are described.

## 2.2     Preparation of Tellurite Glass

Primary composition described in this dissertation is of TZN-75. The flow diagram for the preparation of TZN-75 is shown in Figure 2.2. This tellurite glass composition was prepared by mixing 75mol% $TeO_2$, 20 mol% ZnO and 5 mol% $Na_2O$ powders that were carefully ground and well mixed into a fine powder (step 1). The powder mixture was placed in a golden crucible and heated in a furnace where the temperature was raised to the 800°C in 30~40 minutes and held there for another 100 minutes (step 2). Before casting, the melt was perturbed by shaking the crucible few times to make the melt more homogenous. The billet was prepared by pouring the melt into a 32.5 mm diameter brass mold, kept on a brass plate, both preheated at 240°C (step 3). The billet was then annealed at 311°C for 7 hours and slowly cooled to 50°C to remove the residual stresses (step 4). Lastly, it's allowed to cool down naturally to room temperature and is ready for extrusion.
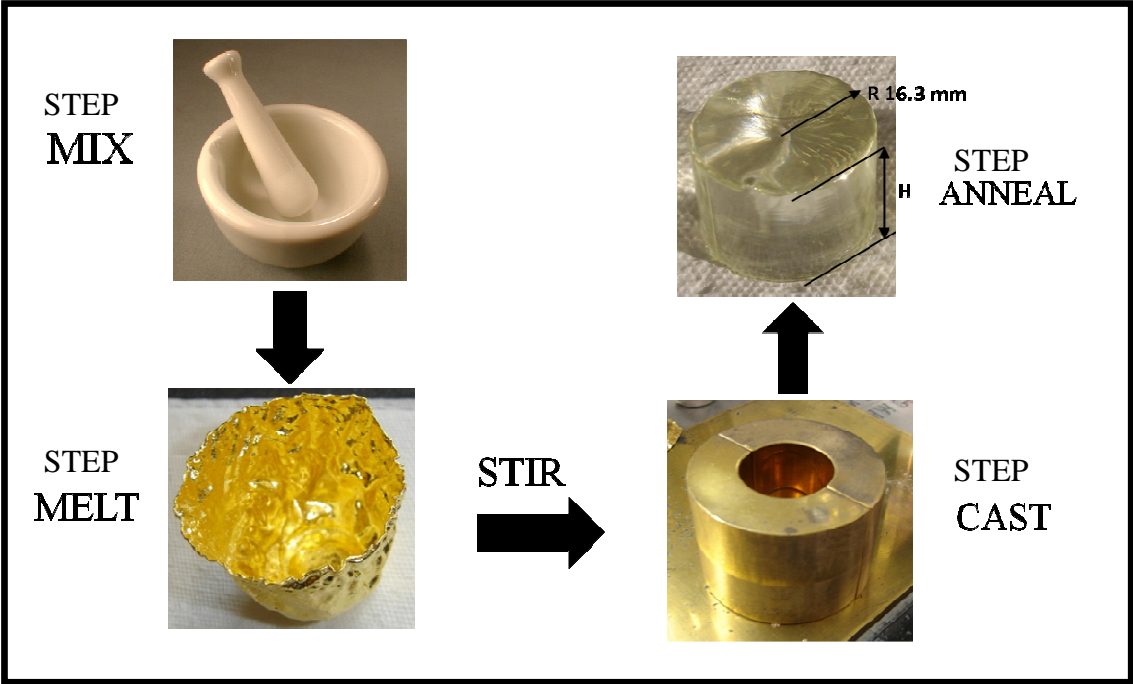
**Figure 2.2** Bulk tellurite glass preparation
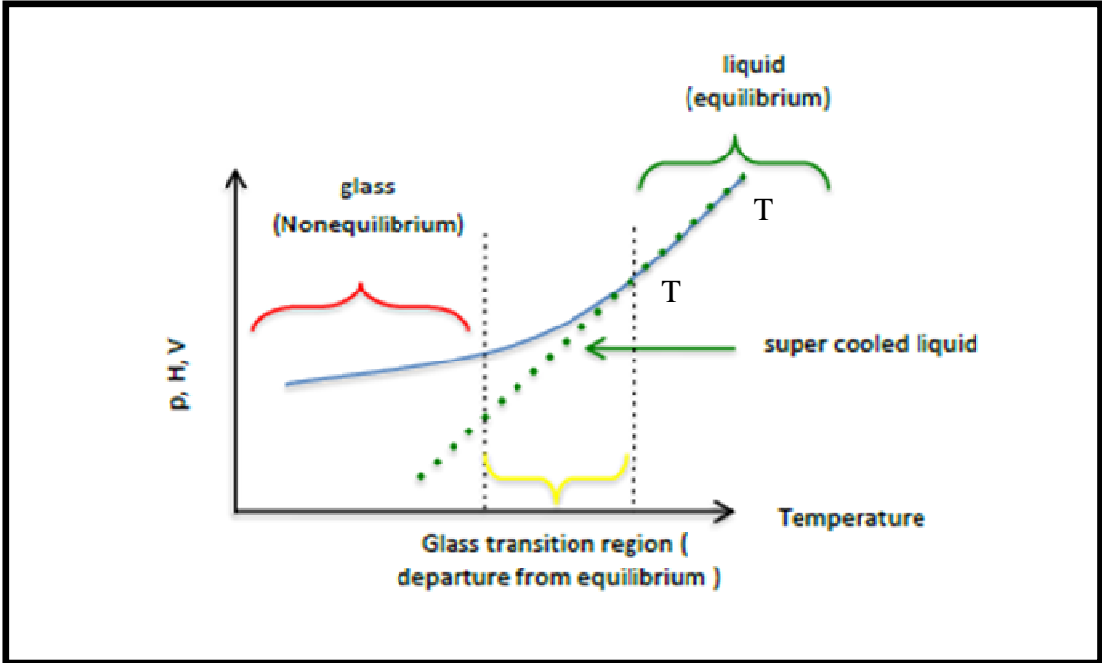


**Figure 2.3** The property-temperature diagram for a glass-forming material [14]

The formation of the glass can be explained from the property-temperature diagram for as shown in Figure 2.3. The property can be volume, enthalpy, entropy or even density, refractive index etc. There are three district regions: liquid (equilibrium) region, glass transition region and glass (non-equlibrium) region. When the glass is at 800°C, it is in the liquid region. The natural relaxation processes occurring in this region are fast enough and thus the melt considered being at equilibrium. When the melt is cooled down past the liquid region, it enters the glass transition region. Here, the liquid begins to depart from the equilibrium (going away from the equilibrium supercooled liquid line shown as dotted). This happens when the molecules in the liquid barely get enough time to relax to their equilibrium states and the liquid becomes metastable. When such a structure is further cooled down, glass is formed.
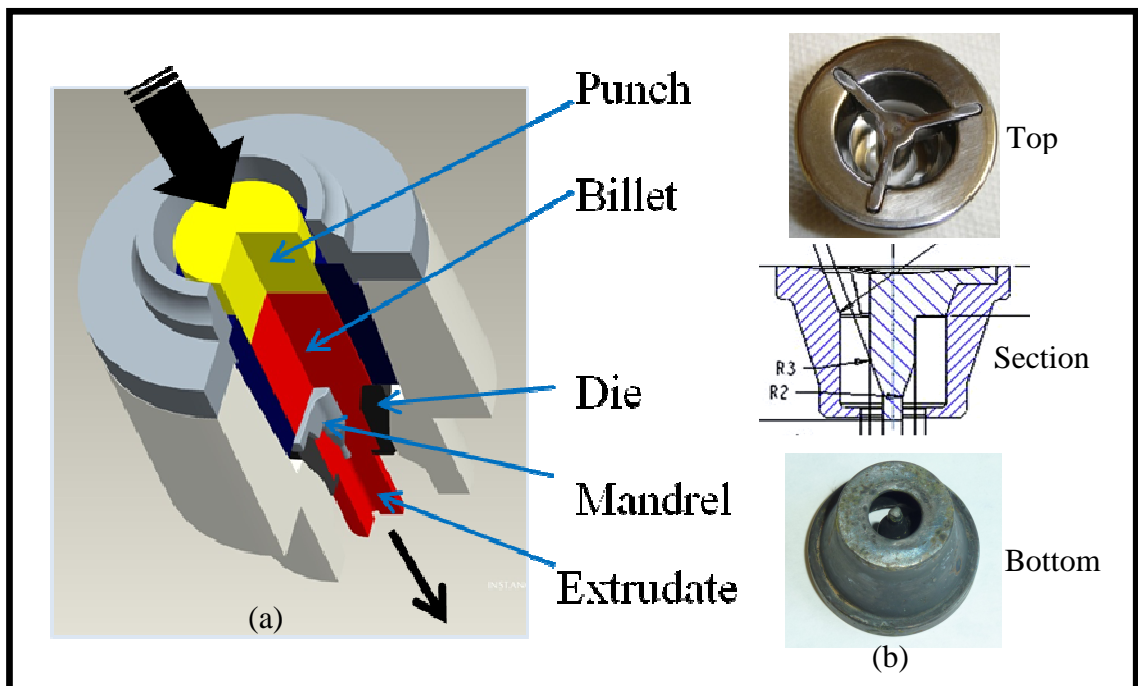


**Figure 2.4** Direct extrusion

18

The optical fiber fabrication process primarily involves two major glass processing techniques: extrusion and drawing. As mentioned in the introduction, extrusion is advantageous because very complex cross-sections can be created (Figure 1.4) and brittle materials such as glass can be formed because the material only encounters compressive and shear stresses. In the extrusion of glass, the glass billet (bulk glass) is heated to a temperature at which the glass is a rubbery material having a viscosity high enough not to slump under its own weight and but low enough so that it can be extruded without any fracture or surface defects. The billet is pushed through the die of desired cross-section to form the extrudate preform. To make preforms having hollow cavities or holes e.g. a tube with a center hole, a center barrier that obstructs the glass flow is required. This central barrier generally called the mandrel is supported at the die entry by three spokes going radially outward from the central section and supported by peripheral die wall as shown in Figure 2.4 (b). The die shape along with the shape of the central barrier then changes along its length (Figure 2.4 (b) Section) into the final shape, with the suspended center piece supported at the die entry (Figure 2.4 (b) Bottom). This kind of die is called the spider die. The disadvantage of spider die is that the glass flowing over the mandrel spokes gets divided and when it's reunited, if the extrusion conditions are not right enough would form weld lines as shown in Figure 1.6 (a) that are weaker strength wise and are the cause of light scattering as well.

In fiber drawing, the core and clad glass held together as shown in Figure 2.5 (a) and heated in the drawing furnace (Figure 2.5 (b)) to a drawing temperature, the temperature at which the glass starts to flow by itself or by gravity. Glass starts to soften at one particular zone where the clad glass collapses onto the core rod to form a neck (as

19

shown in Figure 2.5 (c)) i.e. a diameter reduces almost 25~50 times. The diameter of the fiber can be further reduced by adjusting the pulling speed and drawing temperature. The fiber eventually is wound onto a drum shown in Figure 2.4 (d).
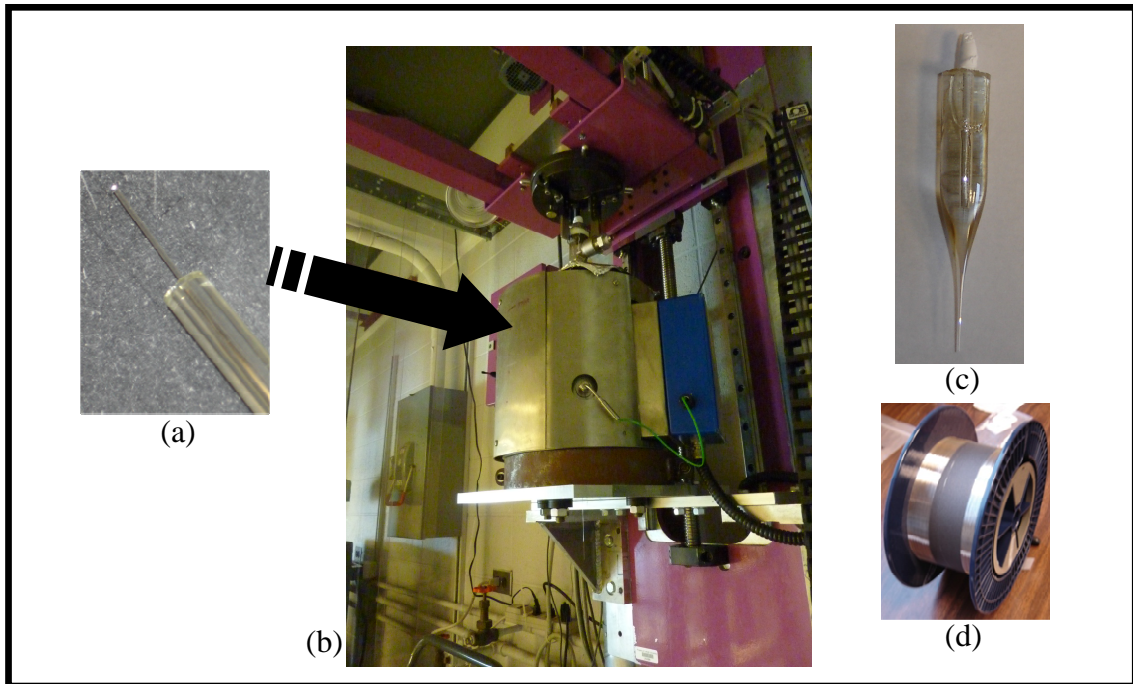


**Figure 2.5** Fiber drawing (a) cane inserted into cladding tube (b) drawing tower (c) neck formation and (d)

In order to obtain good optical preforms from extrusion and high performance optical fibers from the fiber drawing processes, the viscosity of the glass being extruded or drawn should be in the correct range. As shown in the viscosity vs. temperature curve in Figure 2.6, there are four important viscosity ranges suitable for various processes. Drawing is carried out near working point, viscosity=$10^3$ Pa.s. Extrusion is carried out at softening point, viscosity $10^{6.65}$ Pa.s. The range between working point and softening point is called working range. Strain point ($10^{13.5}$ Pa.s) and annealing point ($10^{12}$ Pa.s) are the points of higher and lower limits for annealing. All of the above points are used in the

20

optical fiber processing.
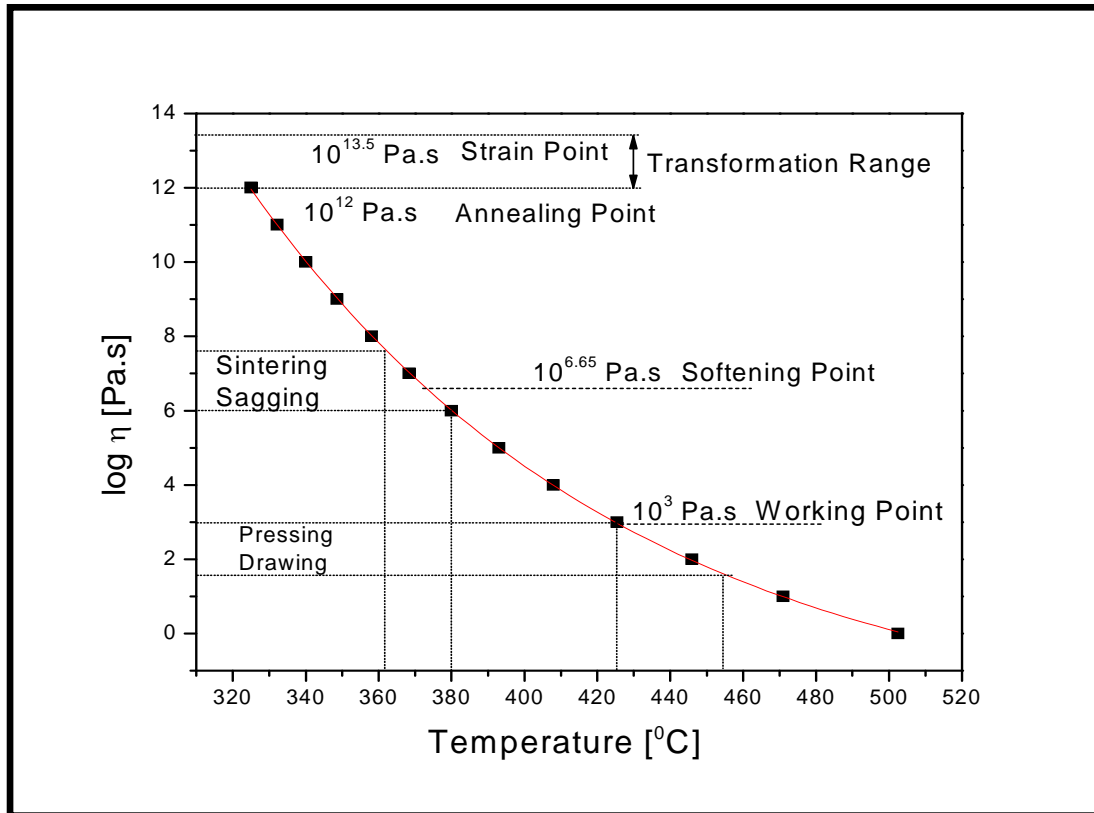


**Figure 2.6** Viscosity vs. temperature for tellurite glass [15]

### 2.3    Optical Fiber Fabrication

The fabrication processes of core-cladding fibers can be classified into three methods: vapor deposition process, double-crucible method (direct melt process) and rod-in-tube method. The vapor deposition process is now the most widely used fabrication process for the optical fiber preforms with core-cladding structure. In the double-crucible method, glass rods with different compositions are used to form the core-cladding structure of the preform by pouring glass from two concentric crucibles and then the preform is directly

drawn into fiber. The method that's' been used in this research for the fiber fabrication is rod-in-tube method. The rod-in-tube method is described in the flow diagram shown in Figure 2.5. In the Figure, holey fiber fabrication is shown on the left hand side and the fabrication of solid-core fiber is described on the right hand side. The fiber preparation starts with forming bulk tellurite glass or billet. The preparation of billet is described in the previous section. In the holey fiber fabrication, the billet is extruded into a holey fiber preform and this preform is drawn into a holey fiber cane of size 1~2 mm. A cladding or tube preform is separately extruded. The holey fiber cane is inserted into the cladding tube and is drawn together into a holey fiber (Figure 2.7).
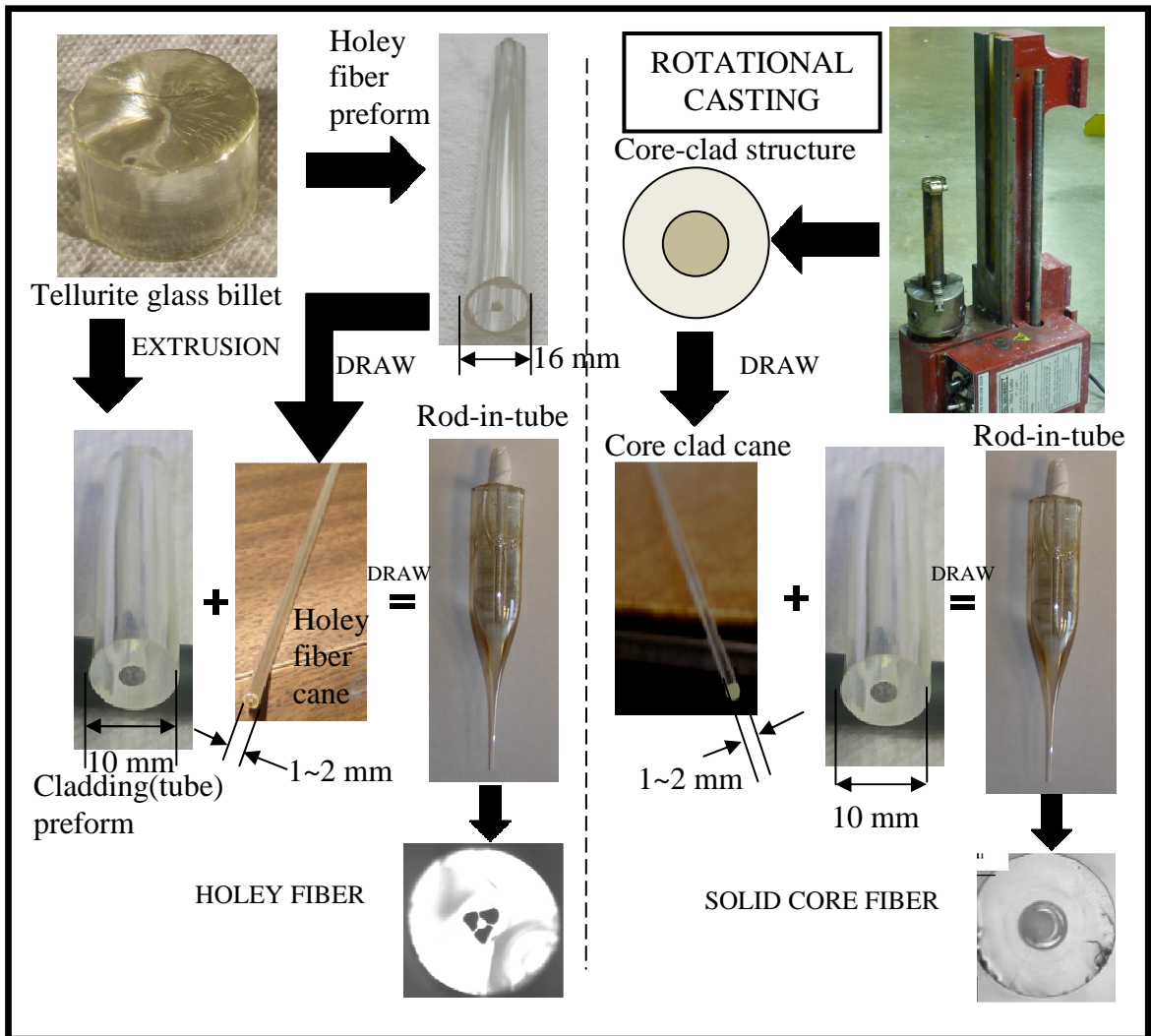
**Figure 2.7** Tellurite glass optical fiber fabrication

In the fabrication of single mode solid-core fibers (right hand side, Figure 2.7), in addition to the extrusion, rotational casting is used to make the solid-core cane. In rotational casting, the core and clad melts are poured in succession into a circular cylindrical mold and the mold is rotated along its axis using a mechanical lathe at 2500~3000 rpm for about 30~40 seconds until the melt is solidified into a core-clad structure. The core-clad structure is then annealed near the glass transition temperature ($T_g$) of the cladding glass to remove the residual stresses. Core-clad structure made by rotational casting has an interface without any defects such as trapped air or dust particles and thus there is less chance of light scattering at the interface and better light transmission

The core-clad structure made such as way is drawn into a cane with 1~2 mm diameter. A cladding glass tube preform is separately extruded. The cane is then inserted into the cladding tube and is drawn together to form solid-core fiber. The solid core fiber is drawn twice and has two claddings and a small core. The rotational casting along with rod-in-tube method is used to make single-mode solid-core optical fibers.

## 2.4    Tellurite Glass Structure
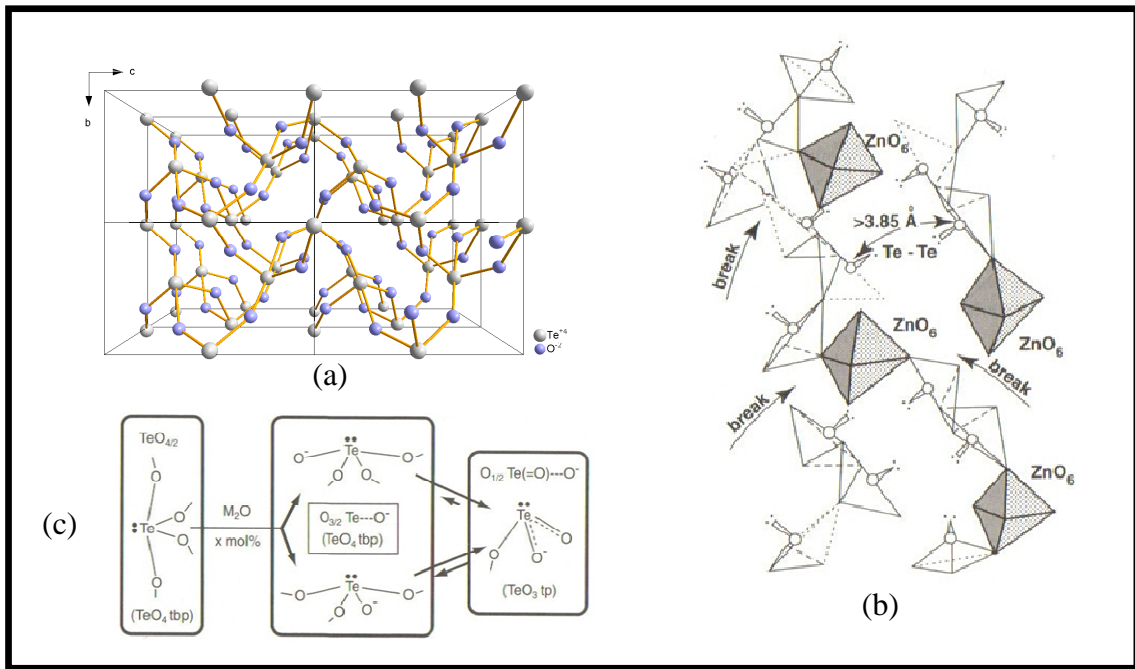


**Figure 2.8** Atomic arrangement in (a) Tellurium oxide powder and (b) 80TeO$_2$-20ZnO (mol%) glass (c) Effect of M$_2$O on tellurite glass

Tellurite glass has similar structure and thermo properties to those of common glasses. Tellurium oxide (TeO$_2$) itself cannot form glass. Commercial tellurium dioxide is white powder with parallel crystal structure (Tetragonal α- TeO$_2$) and its structure is shown in Figure 2.8 (a) [16]. But when modifiers such as ZnO or Na$_2$O are added into TeO$_2$, the regular crystal structure would be broken by the ZnO$_6$ structure unit or non-bridge O atoms introduced by Na$_2$O, and glass can be formed. See Figures 2.8 (b) [17] and 2.8 (c) [18].

# CHAPTER 3

## RHEOLOGICAL PROPERTIES OF TELLURITE GLASSES

### 3.1 Introduction

Viscosity is the most important physical and technological property of a glass in the fabrication of preforms and fibers. It is especially important for determining the processing conditions such as shear rate and temperature when using extrusion to make preforms prior to drawing fibers. Likewise, modeling extrusion of glass depends critically on understanding the viscosity behavior in the appropriate range of shear rates and temperatures. Using parallel plate rheometry, the viscosities encountered in the extrusion and fiber drawing processes ($10^4$ - $10^8$ Pa.s) can be easily reproduced and measured. The method utilizes inexpensive parallel plates and easily prepared samples and is simple to use. Therefore, this technique has become increasingly popular for studying the viscosity-temperature-shear rate relations of promising optical materials with potential use in optical fiber technology [19].

Viscosity of several glasses has been studied previously using parallel plate rheometry [15, 19, 20]. While measurements on the viscosity of tellurite based glasses such as $TeO_2$-$V_2O_5$-$BaO$ [21] and $TeO_2$-$Li_2O$ [22] have been performed in the past, viscosity of $TeO_2$-$WO_3$-$Na_2O$-$Nb$  and $TeO_2$-$ZnO$-$Na_2O$ glasses has not been extensively studied. The purpose of this study was to measure the steady state viscosity ($\eta_s$) and dynamic viscosity ($\eta^*$) of tellurite glasses having composition $75TeO_2$-$15WO_3$-$8Na_2O$-$2Nb$ (TWN-Nb) and $75TeO_2$-$20ZnO$-$5Na_2O$ (TZN-75) at temperatures and shear rates typically occurring in glass forming processes such as extrusion and drawing. This

chapter presents the results and derived glass characteristics obtained from the tellurite glass viscosity measurements such as the type of flow (Newtonian/non-newtonian), activation energies and fragility.

### 3.2 Experimental procedure for glass transition temperature and viscosity measurements

Tellurite glass was prepared by mixing 75mol% $TeO_2$, 20 mol% $ZnO$ and 5 mol% $Na_2O$ powders that were carefully ground and well mixed into a fine powder. The powder was dried at 473 K for 1.5 hours and the temperature was then raised to a melting temperature of 1073 K in 1.5 hours. The melt was held at 1073 K for another 3 hours. The samples were prepared by pouring the melt into 2 mm thick ring-like steel molds which were kept on a brass plate preheated to 505 K. The samples were then annealed at 572 K for 7 hours and were finally allowed to cool down to room temperature. The samples were carefully polished to about 2 mm thickness using a precision polishing machine. Thermal analysis was performed on glass pieces weighing between 10 and 12 mg sealed in aluminum pans, using a DSC 2910 Differential Scanning Calorimeter under flowing $N_2$ at a heating rate at 10 K/min. The glass transition temperature, $T_g$, and the crystallization temperature, $T_x$, were measured and the thermal stability of the glass was determined as the difference between the $T_g$ and the temperature at the onset of crystallization, $T_x$. Similar procedure was used to make TWN-Nb glass samples.

The steady state shear viscosity was measured at multiple temperatures between $T_g$ and $T_x$ by applying a steady state shear strain using an Advanced Rheometric Expansion System (ARES) from TA Instruments in a parallel plate configuration. The

samples used in the experiment were 8 mm in diameter with thicknesses between 1.5 and 2 mm. Measurements were made over a wide range of shear rates to study the shear rate dependence of the viscosity. The rheometer was used in the continuous rotation mode to apply strain. The viscosity was obtained from the following expression:

$$\eta_s = \tau/\dot{\gamma} \tag{3.1}$$

where $\eta_s$ is the steady state viscosity, $\tau$ is the shear stress and $\dot{\gamma}$ is the shear rate. Shear stresses were measured for logarithmically incremental shear rates and the shear stress to shear rate ratio was calculated to yield the viscosity $\eta_s$.

Unlike steady state measurements, where continuous strain was applied, dynamic measurements involved applying a smaller strain by rotating the bottom plate by an angle corresponding to that particular strain and then the frequency of the rotation was increased logarithmically.

### 3.3      Steady State Viscosity Measurement Results

As shown in Figure 3.1, $T_g$ and $T_x$ for TWN-Nb glass were measured to be around 639 K (366°C) and 813 K (540°C) respectively and for TZN-75, around 580 K (307°C) and 682 K (409°C) respectively, defining the lower and upper limits of the glass transformation region. Accordingly, the temperature range selected for the rheometry measurements was from 673 (400°C) to 753 K (480°C) for TWN-Nb and 609 (336°C) to 663 K (390°C) for TZN-75 in order to accommodate the torque limit of the instrument as well as to avoid crystallization in the glass samples during the measurements. The steady state viscosity was measured between shear rates 0.01 and 50 s$^{-1}$ in the above temperature range with a temperature step of 5 K and 10 K for TZN-75 and TWN-Nb samples. The shear rate

dependence of the viscosity of the TWN-Nb and TZN-75 glasses are shown in Figures 3.2 and 3.3 respectively.
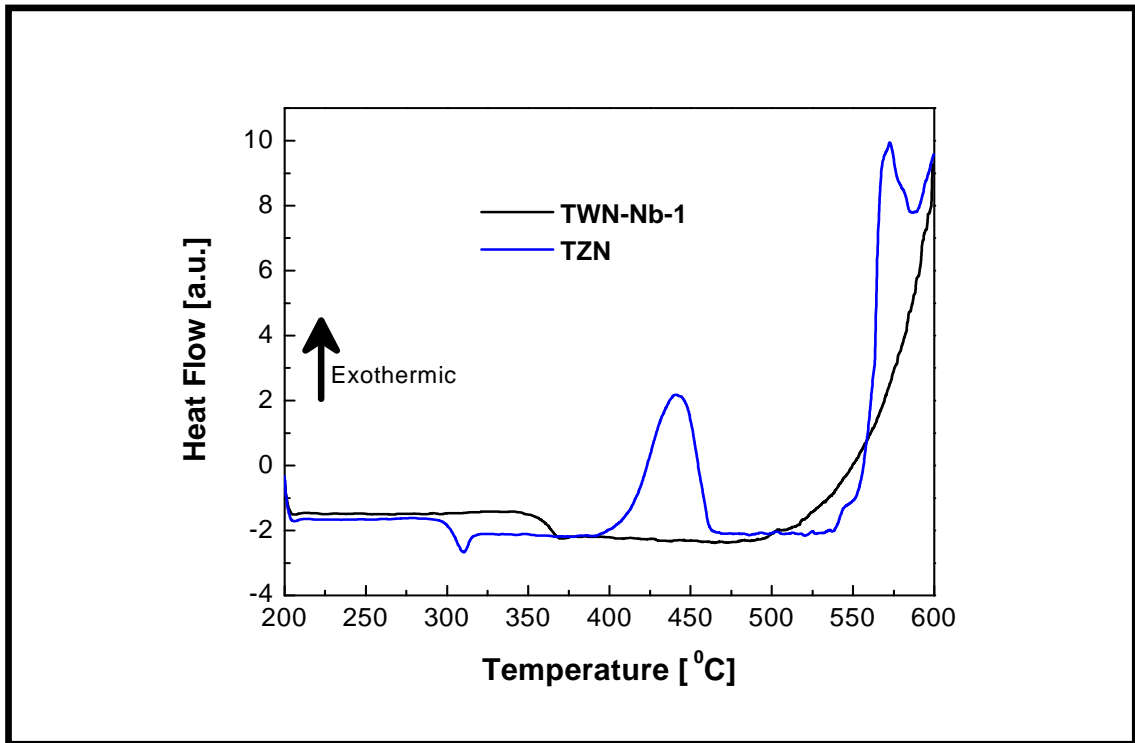


**Figure 3.1** DSC curve of the TWN-Nb and TZN glass obtained at 4.72 K/s under flowing N2

(a)



(b)
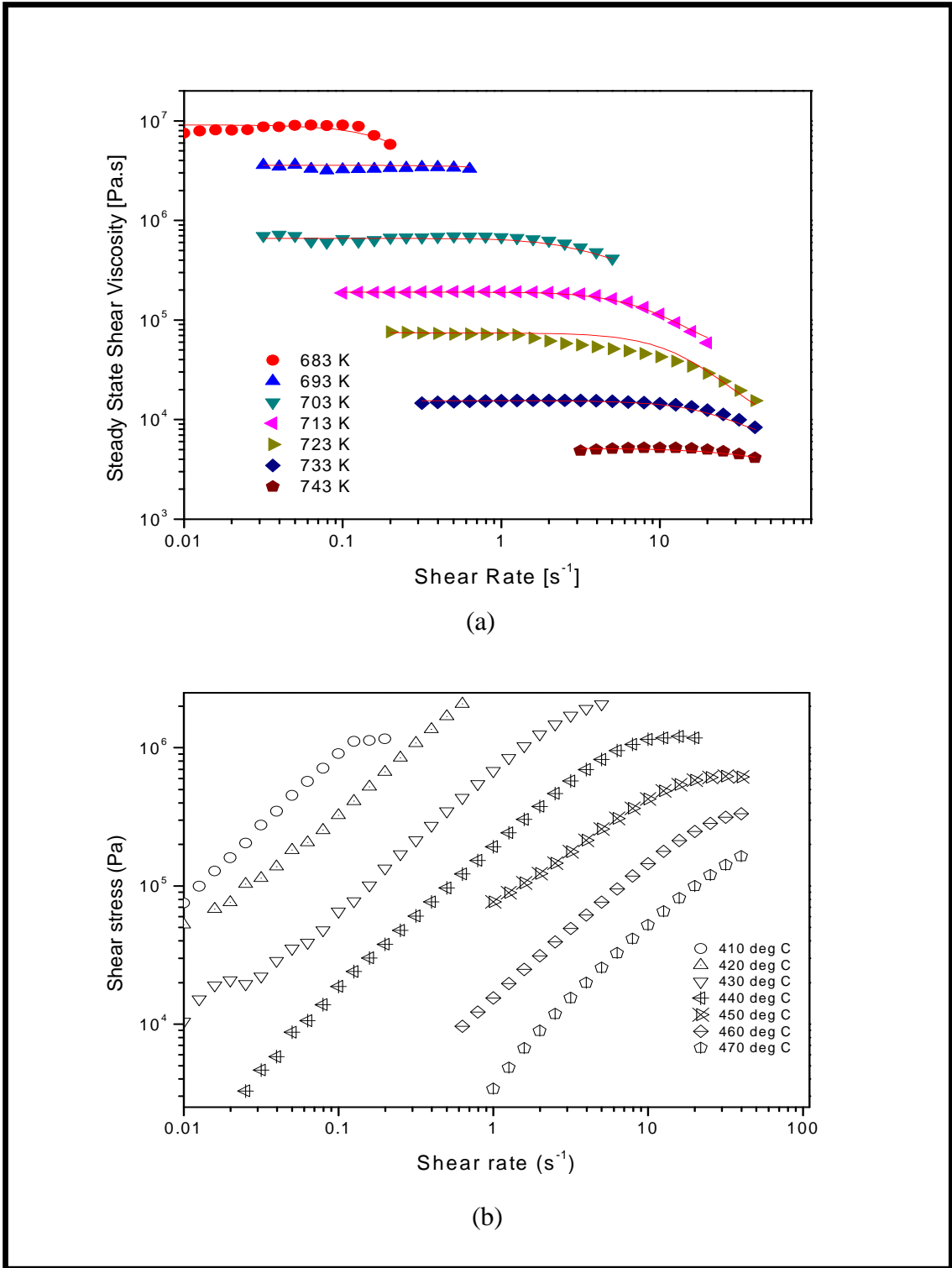
**Figure 3.2** (a) Steady shear viscosity and (b) shear stress with respect to shear rate for the TWN-Nb glass. Shear thinning is seen in TWN-Nb glass as the viscosity drops with shear rate in addition to increasing rate of shear stress

### 3.3.1 TWN-Nb Glass

At each temperature between 683 and 743 K, and for $\dot{\gamma} < \dot{\gamma}_c$, the viscosity, $\eta_s$ is seen to be constant and independent of shear rate while for $\dot{\gamma} > \dot{\gamma}_c$, $\eta_s$ decreases gradually with increasing shear rate except for 683 and 693 K. At 683 K, viscosity drops abruptly with shear rate which may indicate the sample experiencing slippage between the two parallel plates. At 693 K, the viscosity drop was not seen because before the drop, the torque limit of the instrument was reached. So, for temperatures from 703 to 743 K, the shear rate at which the flat section of the curve intersects the linear drop is defined as critical shear rate $\dot{\gamma}_c$ and appears to increase with temperature. The section of the viscosity curve that is flat with respect to the shear rate spans the newtonian viscosity range, and that for $\dot{\gamma} > \dot{\gamma}_c$ the non-newtonian viscosity range. This glass composition is said to behave as non-newtonian or shear thinning fluid in this case because viscosity decreases with shear rate even though rate of shear stress kept on increasing. If the viscosity drops wit shear rate but also shear stress drops, that means slipping and is not a shear thinning behavior. As seen in Figure 3.2 (a), the newtonian viscosity decreases by more than three orders of magnitude over 70 degrees, from $8 \times 10^6$ Pa.s at 683 K to around $5 \times 10^3$ Pa.s at 743 K.

### 3.3.2 TZN-75 Glass

Similar behavior is observed as shown in Figure 3.3. At each temperature between 609 and 663 K, and for $\dot{\gamma} < \dot{\gamma}_c$, the viscosity, $\eta_s$ is seen to be constant and independent of shear rate while for $\dot{\gamma} > \dot{\gamma}_c$, $\eta_s$ decreases rapidly with increasing shear rate. The shear rate at which the flat section of the curve intersects the linear drop is defined as critical shear rate $\dot{\gamma}_c$ and appears to increase with temperature. The newtonian viscosity decreases by

31

more than three orders of magnitude over 50 degrees, from $2 \times 10^7$ Pa.s at 609 K to around $10^4$ Pa.s at 663 K.
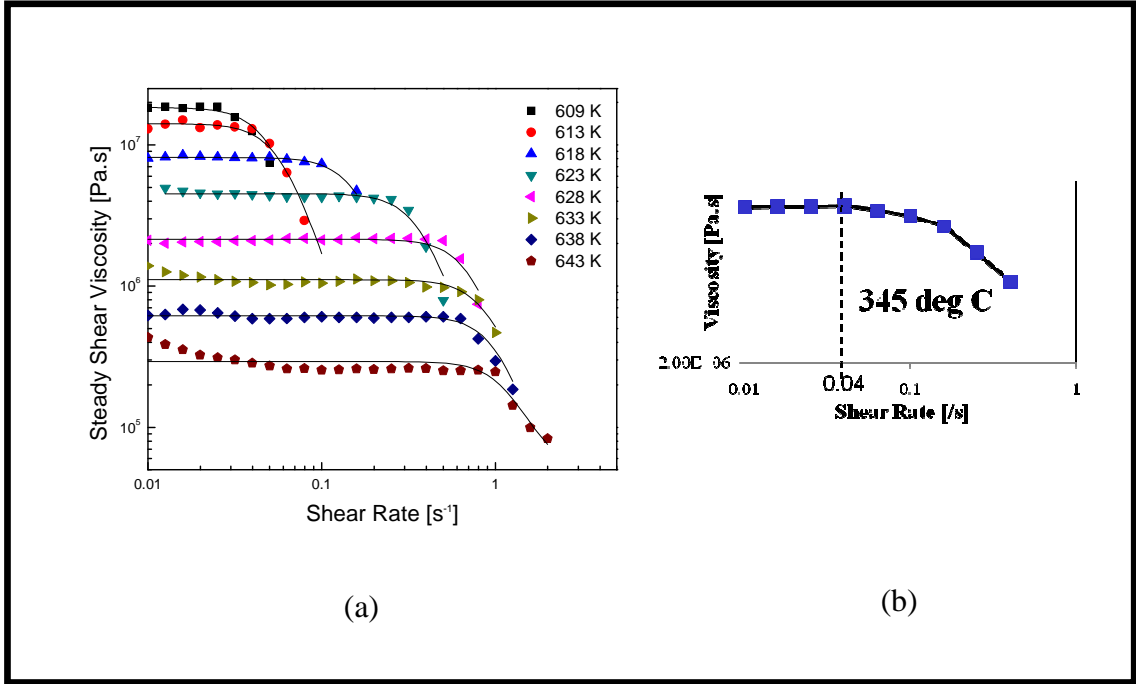


**Figure 3.3** (a) Steady state viscosity with respect to shear rate for the TZN glass and corresponding best-fit curves based upon Eq. 3.2 (Cross model) at different temperatures in the glass transformation range investigated. (b) Steady shear viscosity with respect to shear rate at 618 K. The drop in viscosity is less abrupt than the drop observed at other temperatures investigated

In Figure 3.3 (a), viscosity drops abruptly compared to the viscosity curves shown in Figure 3.2 for TWN-Nb glass. At lower temperature such as 609 and 613 K, the sample slips between the parallel plates causing the drop and at higher temperatures such as from 623 to 643 K, the glass samples were observed to undergo surface crystallization and therefore the drop in viscosity and shear stress was observed. But at 618 K (345°C) as shown in Figure 3.3 (b), the sample did not slip and did not crystallize indicating the viscosity dropped with respect to shear rate as the rate of shear stress increased i.e. shear

thinning was observed at 618 K. Useful information such as relaxation time constant, activation energy and fragility was obtained for TZN-75 glass from Figure 3.3 as discussed in the following sections.

### 3.3.3 Relaxation time constant, activation energy and fragility

Various models have been used to describe the dependence of viscosity on shear rate and temperature. For polymers such as polystyrene, poly(methyl methacrylate) and polycarbonates, the temperature and shear rate dependence of the viscosity have been modeled using the generalized Cross/Carreau [23] and the Carreau-Yasuda model [24], both providing a great deal of flexibility. Here, the Cross model was used to fit the experimental data in Figure 3.3 (a), which is an alternate form of the generalized Cross/Carreau model with the same functional form as that of the Cole-Cole equation representing dielectric relaxation. In the Cross model, the viscosity is represented in the following form [23]:

$$\eta = \eta_\infty + \frac{\eta_0 - \eta_\infty}{1 + (\dot{\gamma}\tau_s)^p} \tag{3.2}$$

where $\eta_\infty$ is the viscosity at infinite shear rate, $\eta_0$ the viscosity at zero shear rate, $\tau_s$ is the time constant and $p$ determines the slope of the viscosity curve in the non-newtonian regime. The parameters $\eta_0$ and $\eta_\infty$ are respectively the maximum and minimum viscosities for each viscosity-shear rate curve at that particular temperature. As seen in Figure 3.3 (a), the quality of the fit obtained with this model is good. However, it is important to note that, because of the limited extent of the experimental data at higher shear rates, the parameter $\eta_\infty$ is not precisely determined. Consequently, in the fitting $\eta_\infty$ was chosen to be the average value between zero and the viscosity value measured at the

highest shear rate at that temperature. In any case, the $\tau_s$ determined from the fit was found not to be very sensitive to the choice of $\eta_\infty$, primarily because of the rapid drop in viscosity for $\dot\gamma > \dot\gamma_c$ ($\dot\gamma_c \tau_s \approx 1$) or, equivalently, the large value of the parameter $p \approx 4$ at all temperatures. As explained below, this determination of $\tau_s$ is also useful because it allows an independent measurement of the activation energy, which can then be compared to that, determined from the viscosity measurements at low shear rates.
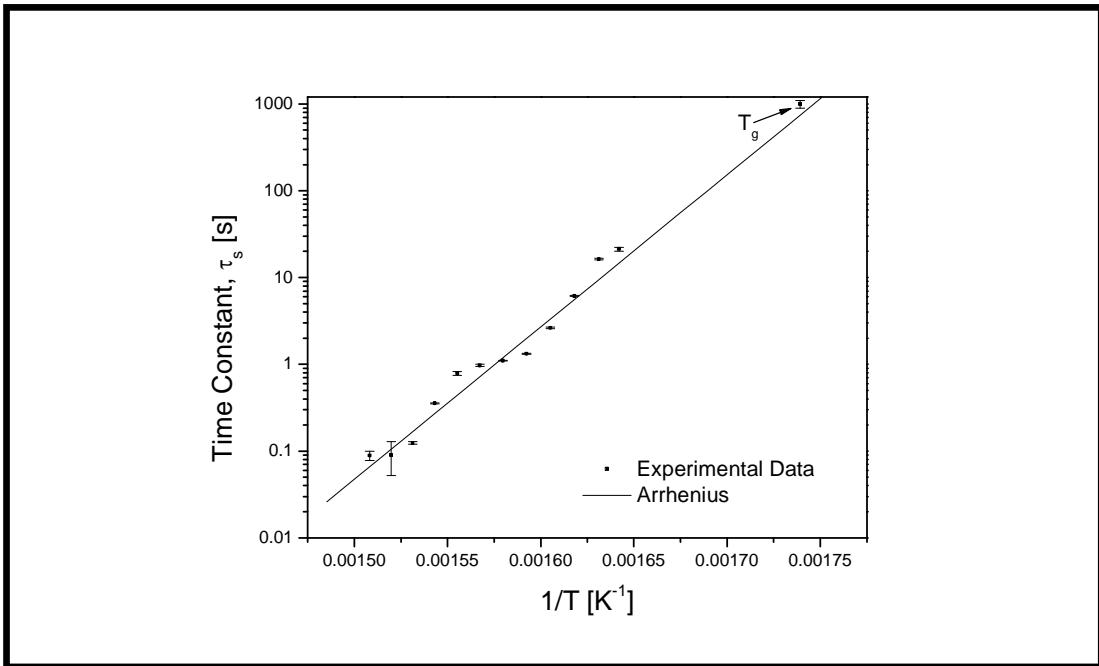


**Figure 3.4** Temperature dependence of time constant in the temperature range from 572 to 663 K. Relaxation time at $T_g$ is taken to be approximately equal to $10^3$ s as per [10]. The experimental data is observed to follow the Arrhenius law quite well

The time constant, $\tau_s$, obtained from the fitting is plotted in Figure 3.4 as a function of temperature. In the same figure, the relaxation time at $T_g$ is reported, typically chosen to be on the order of $10^3$ s [25]. Many equations such as Arrhenius, Vogel-Fulcher-Tamman (VFT) and Cohen-Grest can be used to fit the relaxation time-

temperature curve of the TZN glass. The Arrhenius law was found to fit the data as well as the two other equations over the limited temperature range investigated and was therefore chosen for its simplicity. The Arrhenius equation is given as [26]:

$$\eta_0 = A_\tau e^{\Delta H_\tau/RT} \tag{3.3}$$

where $A_\tau$ is a constant for a given material, $R$ is 8.314 $JK^{-1}mol^{-1}$ or 1.987 $calK^{-1}mol^{-1}$ and $\Delta H_\tau$ is the activation energy for relaxation. The fit in Figure 3.4 yields the following parameter values, $A_\tau$ = -28.4 Pa.s and $(\Delta H_\tau/R)$ = 1.81 $\times$ $10^4$ $K^{-1}$ which makes the activation energy of relaxation to be about 83 kcalmol$^{-1}$.
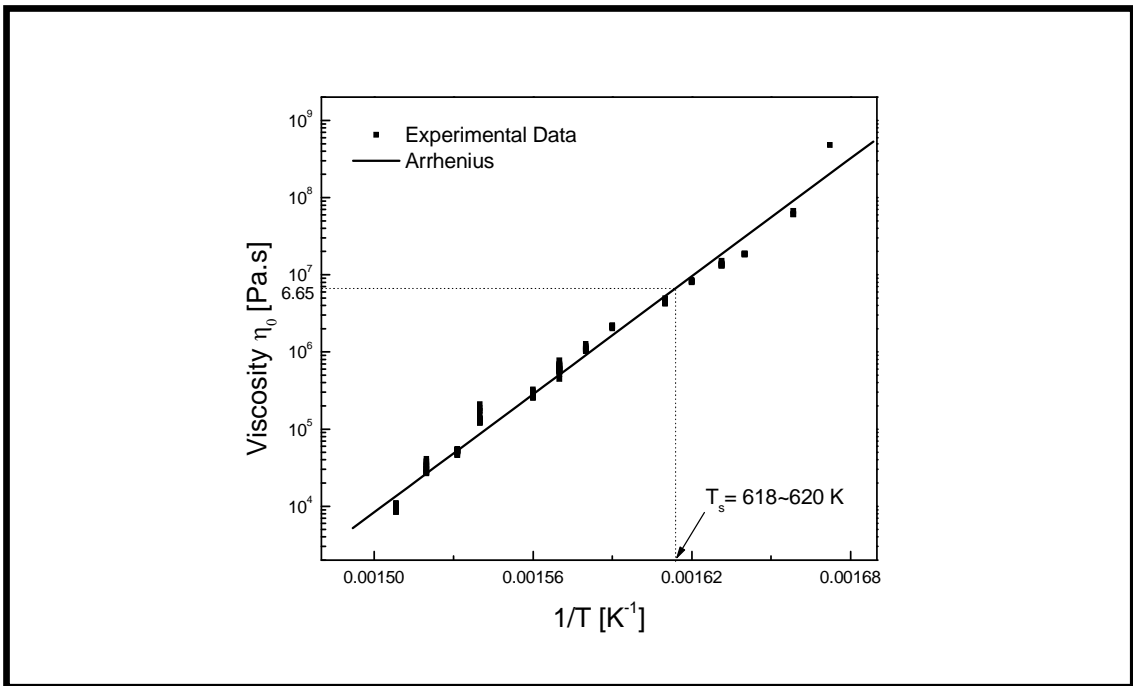


**Figure 3.5** Temperature dependence of newtonian viscosity following the Arrhenius behavior in the glass transformation range investigated. The softening point $T_s$ for the TZN glass, corresponding to log $\eta_0$=6.65 Pa.s [26], is about 618 to 620 K

The newtonian viscosity, also called zero-shear rate viscosity $\eta_0$, is plotted in Figure 3.5 in the Arrhenius coordinates $\eta_0$ vs. $1/T$. In the temperature range studied, the

zero-shear rate viscosity of the TZN glass is also observed to follow an Arrhenius law. According to our fit, $A_\eta$ = -37.4 Pa.s and $(\Delta H_\eta/R)$ = 2.74 × $10^5$ $K^{-1}$; thus the activation energy for viscosity of the TZN glass is calculated to be about 200±20 kcal/mol. Also obtained from the fit, softening temperature $T_s$ for the TZN is shown in Figure 3.5. This is an important piece of information, since glass forming processes such as extrusion or pressing are usually carried out around this temperature [27].
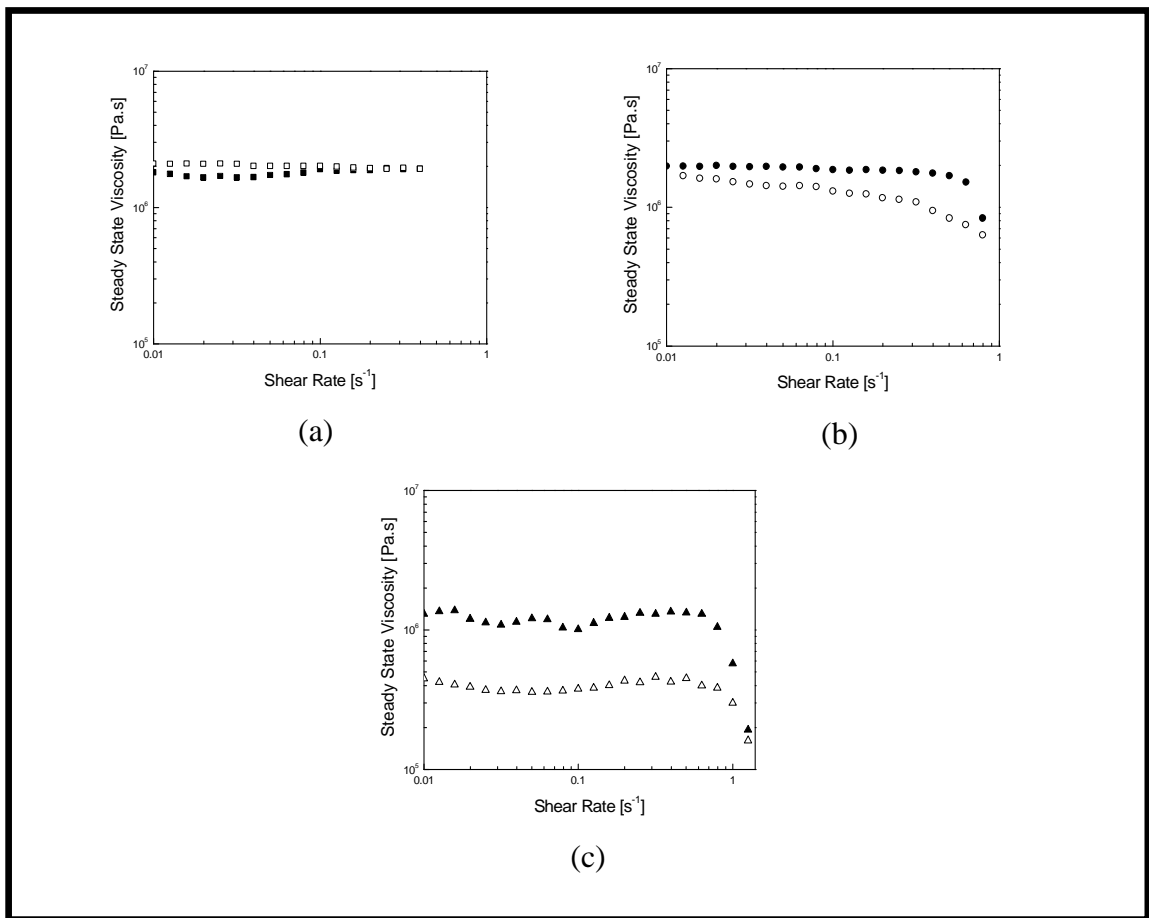


**Figure 3.6** Steady state viscosity with respect to increasing (close symbols) and decreasing (open symbols) shear rates measured at 628 K. TZN glass structure exhibits (a) full recovery (b) partial recovery (c) no recovery demonstrating breaking of Te-O bonds.

It is important to note the difference between $A_\tau$ and $A_\eta$ and the corresponding activation energies $\Delta H_\tau$ and $\Delta H_\eta$. The higher activation energy, $\Delta H_\eta$, is obtained from the measurement conducted using the viscosity measured at low shear rates while the lower activation energy, $\Delta H_\tau$, is obtained from fitting the full viscosity curve in Figure 3.3 (a), including the higher shear rate measurements. This result is actually surprising for a relaxation process, the measurements of which should be reversible. Instead, it suggests that a structural change takes place in the glass when it is sheared past a certain critical shear rate, $\dot{\gamma}_c$. In order to verify this point, a simple experiment was conducted using ARES, the results of which are shown in Figure 3.6. In this experiment, viscosities of three TZN glass samples were measured at increasing shear rates from 0.01 to 0.4 $s^{-1}$, 0.01 to 0.8 $s^{-1}$ and 0.01 to 1.25 $s^{-1}$ and then, immediately following, measured at decreasing shear rates, from the highest rate back to 0.01 $s^{-1}$. The glass sheared up to 0.4 $s^{-1}$ was observed to retrace its path reversibly, indicating full recovery of the network structure without the breaking of bonds in Figure 3.6 (a). Upon increasing the shear rate from 0.8 $s^{-1}$ (Figure 3.6 (b)), the viscosity was seen to have dropped sharply indicating changes in the network structure and the breaking of a few Te-O bonds. Partial recovery of the network structure nevertheless occurred since the viscosity returned to its starting value at 0.01 $s^{-1}$. Finally, when sheared up to 1.25 $s^{-1}$, a significantly lower but constant viscosity was observed upon decreasing the shear rate (Figure 3.6 (c)), indicating breaking of a significant number of Te-O bonds and negligible recovery of the network structure.

Viscosity data for the TZN glass at low shear rates are plotted in Figure 3.7 along with data for vitreous silica [28], $GeO_2$ [29] and $67SiO_2$. $33Na_2O$ [30] glasses from the

literature in an 'Angell plot' in the coordinates *log η₀* vs. *normalized temperature $T_g/T$*
[31]. Although our viscosity data fall in the lower temperature range, not far from the
glass transition temperature, $T_g$, Figure 3.7 also show a fit to the data using a Vogel-
Fulcher-Tammann (VFT) function [26]  extended to the entire range from 0 to 1. It is
interesting to note that, in the fit, $T_g$ corresponds to a viscosity of $10^{12}$ Pa.s, which is the
value of viscosity usually found at the glass transition [32]. As seen in the figure, the
viscosity curve for the TZN glass is significantly rounded when compared to the viscosity
curves for $SiO_2$ and $GeO_2$, a characteristic of 'soft' or 'fragile' glasses as compared to
'strong' ones.
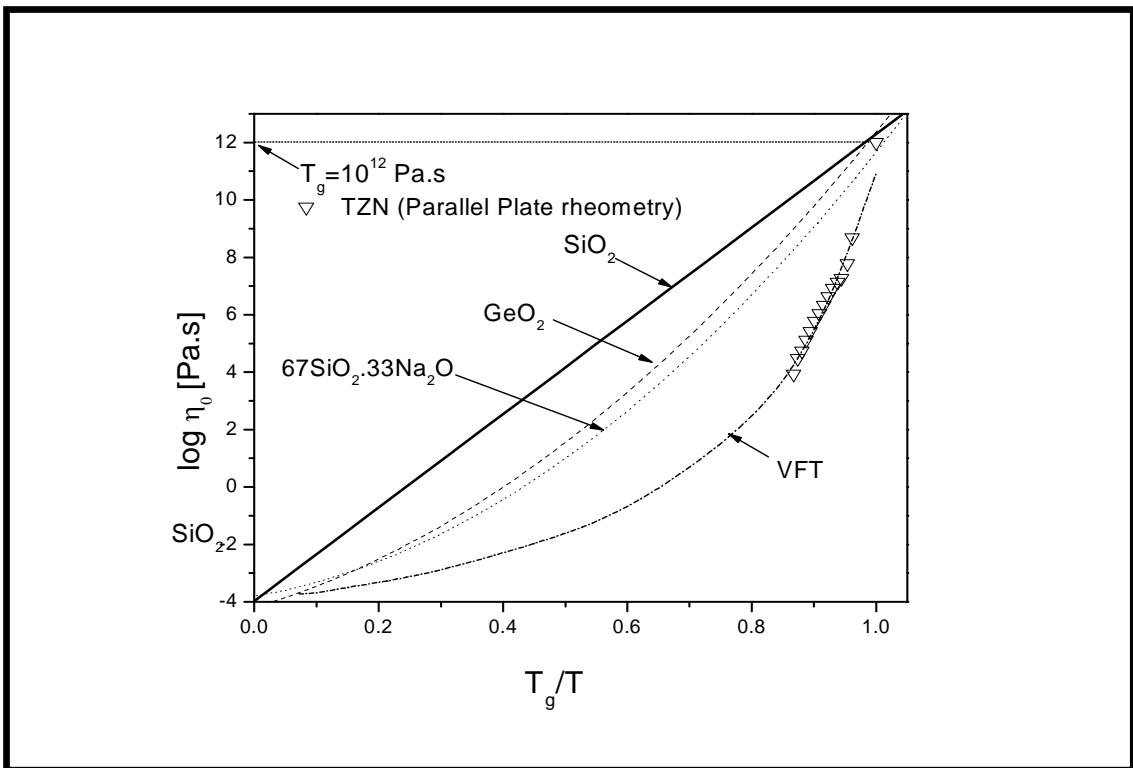


**Figure 3.7** Variation of *log η₀* vs. $T_g/T$ for different glasses. Activation energies are
calculated from the slope of the curves. The viscosities from vitreous silica, germania and
sodium silicate glasses are obtained from [28], [29] and [30] respectively

38

Using the results shown in Figure 3.7, we calculated the fragility index of the TZN glass and compared it with that of other glasses. The fragility of a glass is measured by the degree to which the viscosity deviates from an Arrhenius behavior and is defined by the quantity *m*:

$$m = \frac{d\log \eta_0}{d\frac{T_g}{T}}\bigg|_{T=T_g} \Rightarrow m = \frac{\Delta H_\eta}{2.302RT}\bigg|_{T=T_g} \tag{3.4}$$

From Eq. 3.4, it is clear that the fragility index m depends on the temperature at which the slope is measured; it is common practice to choose the slope at the glass transition temperature. Also in the equation, activation energy obtained in the low shear rate region $(\Delta H_\eta)$ is used to calculate the fragility index since $\Delta H_\eta$ is a better defined quantity than $\Delta H_\tau$ for the reason mentioned earlier. The former value is used in Table 3.1 along with the activation energies of other glasses. Based on the activation energy of $200\pm20$ kcal/mole, the fragility index of the TZN glass is calculated to be about $78\pm7$ and is also compared with that of other well known glasses in Table 3.1.

**Table 3.1** Fragility and activation energy of the TZN glass along with other simple glasses

| Glass | Temperature (deg K) | $T_g$ (K) | Activation Energy (kcal/mol) | Fragility, m $(\Delta H_\eta/2.302RT_g)$ |
|---|---|---|---|---|
| Vitreous Silica | 1400- 1900 | 1476 | 134 | 20 |
| $GeO_2$ | 749-1000 | 749 | 83 | 24 |
| $67SiO_2$-$33Na_2O$ | 700-900 | 711 | 109 | 34 |
| TZN | 572-663 | 572 | $200\pm20$ | $78\pm7$ |

### 3.4 Dynamic Viscosity Measurement Results

Since it was observed above that steady state viscosity measurements induce high deformations in the samples leading to crystallization and/or slippage. Therefore the results at higher shear rates where the viscosity drops abruptly do not reflect the actual behavior of the glass. Thus the dynamic viscosity measurements were performed by applying an oscillating sinusoidal strain at a particular frequency and measuring the resulting stress. To determine the range in which viscosity does not depend on the applied strain, viscosity vs. strain measurements were carried out at different temperatures while keeping constant frequency and increasing the rotation angle of the plate.

### 3.4.1 Dynamic Strain Sweep Test

Dynamic strain sweep measurements were conducted at different temperatures and constant angular frequency. The frequency was held constant at 1.5 Hz and the strain was increased logarithmically from 0.1% to 50% by increasing the rotation angle of the bottom plate.

Figure 3.8 (a) shows strain sweep curves obtained for TZN-75 glass at temperatures ranging from 360°C to 375°C. At 360°C, the viscosity is relatively constant over a wide strain rate interval although it starts to drop slightly for strains in excess of 20%. At higher temperatures, the viscosity curves show a step, which becomes more pronounced and appears at lower strains with increasingtemperature. The step in viscosity was attributed to the breaking of bonds between $TeO_3$ and/or $TeO_4$ structural units [33]. This behavior is shown in Figure 3.8 (b) [18]. At room temperature, $TeO_4$ trigonal bipyramid (tbp) units are higher in number than $TeO_3$ trigonal pyramid (tp) units and

form a well connected structure. As temperature is increased, $TeO_3$ tp units with terminal Te-O bonds (with non-bridging oxygen) such as Te=O and Te-O⁻ increase in numbers relative to $TeO_4$ tbp units and the structure becomes relatively less constrained [22]. Then, even with small strain applied, the glass flows easily with less resistance thereby exhibiting lower activation energy and lower viscosity as depicted in Figure 3.8 (b).



(a)



(b)
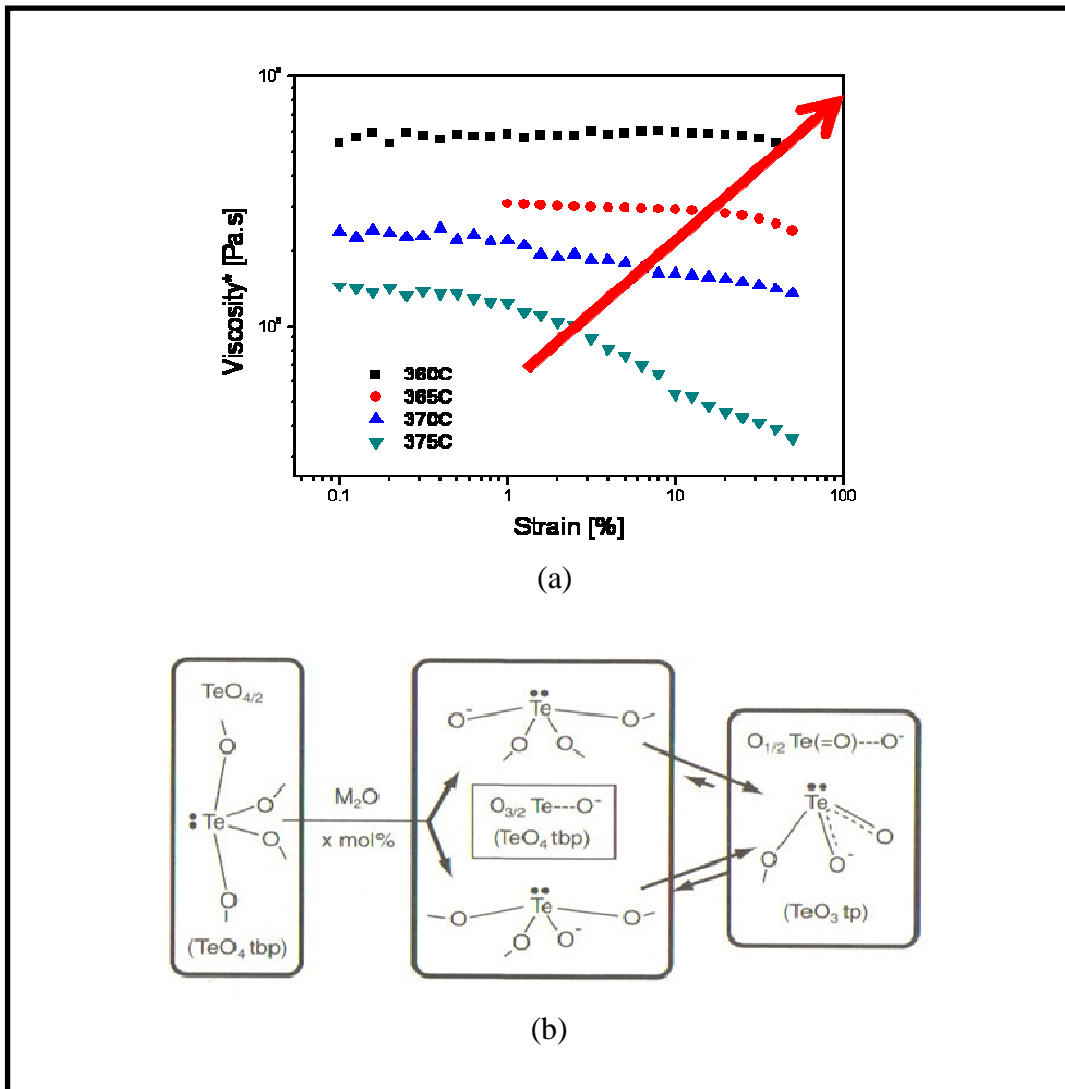
**Figure 3.8** (a) Dynamic strain sweep of TZN-75 glass samples at frequency 1.5 Hz (b) Structural change (TeO4 tbp → TeO3 tp) takes place after drop in viscosity

41

Note that the dynamic strain sweep measurements were not performed at lower temperatures than 360°C. This is either because of the viscosity did not show a step in the strain range investigated or because torque limit of the instrument was reached before appearance of the step. We chose 5% strain for the dynamic frequency sweep measurements because 5% strain would certainly fall with the linear strain range (strain corresponding to the step in the viscosity curve) for extrusion temperatures ranging from 335°C to 350°C.


### 3.4.2 Dynamic Frequency Sweep Test

Dynamic frequency sweep measurements were conducted at 5% strain for the temperatures ranging from 350 °C to 365 °C within the glass transformation range of 307°C and 413°C at frequencies from 0.1 to 50 Hz. The viscosity curves are shown in Figure 3.9 (a).  Drop in viscosity was observed at each temperature and the drop was seen to be shifting to higher frequency ($f$) with increasing temperature.

The frequency range investigated was converted into angular $f$ (rad/s) using the factor (3 $f$ *π/180) and then the dynamic $f$ sweep measurements were converted into steady shear rheological data using modified Cox-Merz rule defined by: $\eta^*(\omega) = \eta(c\dot{\gamma})$

with $\omega = c\dot{\gamma}$ and c a constant equals to 0.41 in the present case [34]

The plot of complex viscosity with respect to ω/c or shear rate is shown in Figure 3.9 (b).
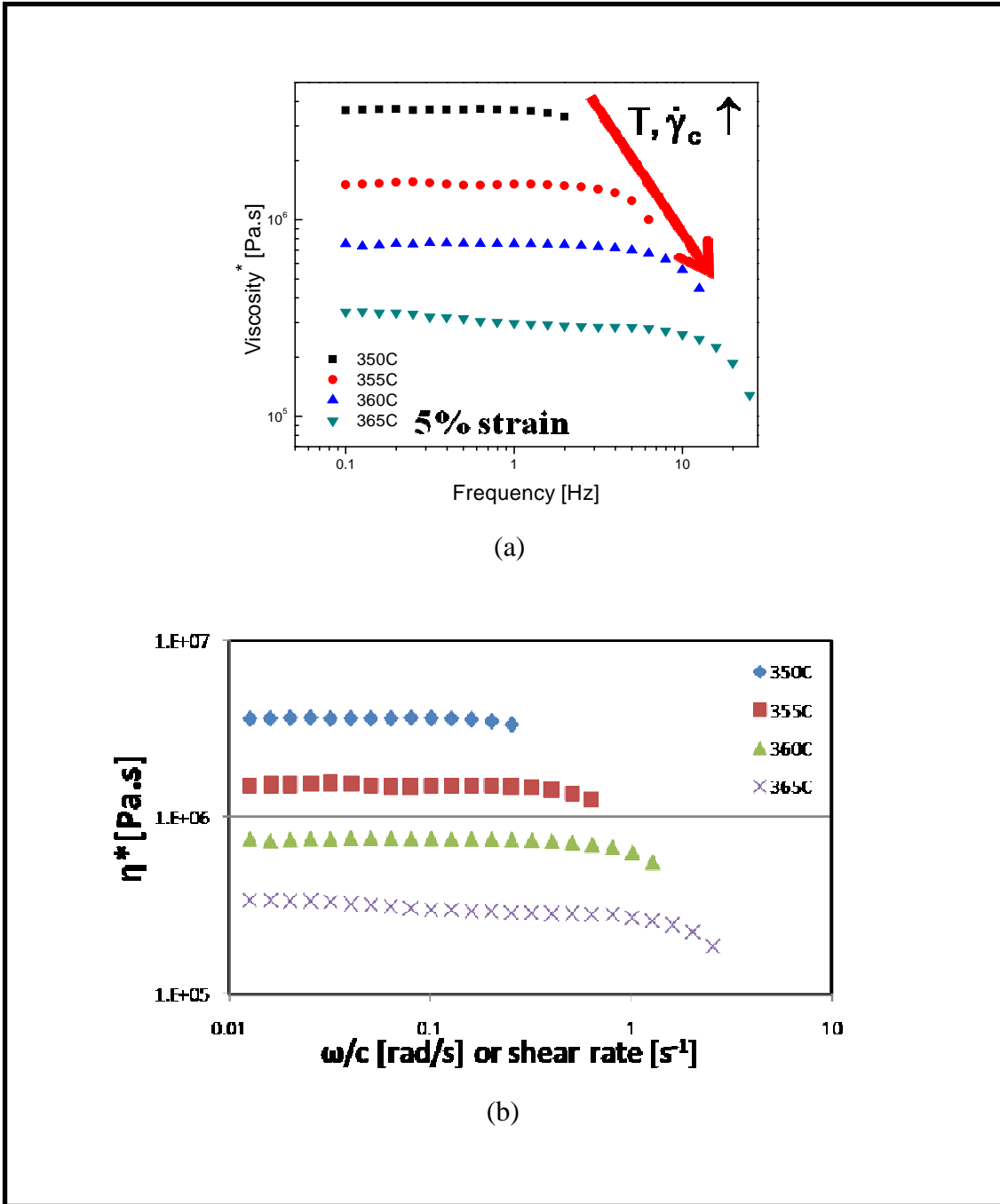
**Figure 3.9** (a) Dynamic frequency sweep of TZN-75 glass samples at 5% strain (b) Viscosity with respect to angular frequency or shear rate

At each temperature, for $\dot{\gamma} < \dot{\gamma}_c$, the viscosity is seen to be constant and independent of shear rate while for $\dot{\gamma} > \dot{\gamma}_c$, the viscosity decreases with increasing shear

rate. Note that the measured shear stress increased while viscosity decreased which renders TZN-75 as a shear thinning fluid. The shear rate at which the flat section of the curve intersects the linear drop is defined as critical shear rate $\dot{\gamma}_c$ and increases with temperature. The section of the viscosity curve that is flat with respect to the shear rate spans the newtonian viscosity range, and that for $\dot{\gamma} > \dot{\gamma}_c$ the non-newtonian viscosity range. A master curve was obtained from Figure 3.9 (b) curves by shifting the curves along x and y axes. The master curve is shown in Figure 3.10 (a). Note that the shift factors $a_{T1}$ and $a_T$ are not equal to each other. Slope of the curve was obtained using power law which is defined as: $\tau = C\dot{\gamma}^n$

But,
$$\eta = \frac{\tau}{\dot{\gamma}}$$

So,
$$\eta = \frac{C\dot{\gamma}^n}{\dot{\gamma}} = C\dot{\gamma}^{n-1} \tag{3.5}$$

where $C = $ Consistency factor

$n = $ Power law index

$n$ is calculated to be $0.7\pm0.1$. $n$ being less than 1 confirms that the glass is shear thinning. $C$ is plotted with respect to temperature in Figure 3.10 (b). The $C$ values at lower temperatures were predicted from the linear fit. The $C$ and $n$ values were utilized in the numerical analysis of tellurite glass flow through the extrusion die for the calculation of pressure gradient and pressure difference as described in Chapter 5.

44
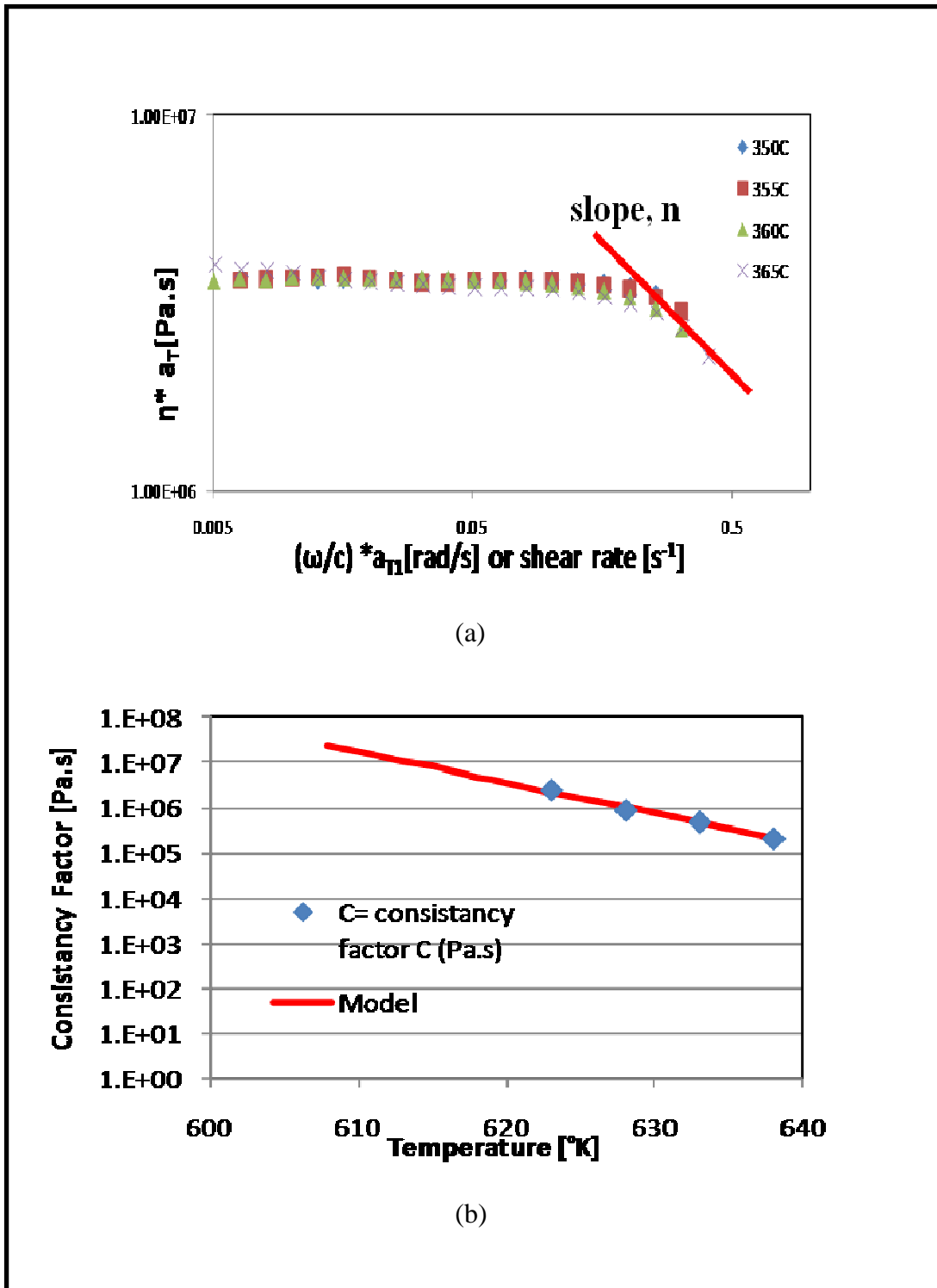
**Figure 3.10** (a) Master curve of TZN-75 glass (b) Variation of Consistency factors with temperature

### 3.5　Discussion

As revealed by Raman studies [35], the tellurite glass network is composed of $TeO_4$ trigonal bipyramid (tbp) and $TeO_3$ trigonal pyramid (tp) structural units. At room temperature and up to moderately high temperatures above $T_g$, the tellurite glass exhibits a well connected structure consisting of tbp and tp units, tbp being higher in number than tp. As the temperature is increased further, $TeO_3$ tp units with terminal Te-O bonds such as Te=O and Te-O$^-$ increase in numbers relative to $TeO_4$ tbp units and the structure becomes relatively less constrained. Thus, the glass flows more easily, thereby exhibiting lower activation energy and lower viscosity as depicted in Figure 3.2 (a), 3.3 and 3.6. A similar argument can be made for the TZN glass samples sheared, first at an increasing and subsequently at a deceasing rate, for which the results were presented in Figure 3.6. For the sample sheared up to 0.4 s$^{-1}$ (Figure 3.6 (a)), the glass structure remained fully connected and any rearrangement of the glass network took place without breaking bonds, simply by a change of local configurations (relaxation), and the viscosity was observed to retrace its path reversibly. With increasing shear rates (up to 1.25 s$^{-1}$), exceeding the relaxation rate of the network, Te-O bonds begin to break, causing an increase in the number of $TeO_3$ units relative to $TeO_4$, and visco-elastic stretching of the network occurs without a corresponding increase in stress. At these higher shear rates, the glass structure shear-thins, thus offering lower resistance to flow or exhibiting lower viscosity. Upon decreasing the shear rate from 1.25 s$^{-1}$, the viscosity remained considerably lower than upon increasing, indicating negligible recovery and a permanent change in the network structure (Figure 3.6 (b)). As suggested earlier, this explains why the two activation energies, one obtained from the low shear rate viscosity data and the

46

other obtained from a relaxation fit of the entire viscosity curve, were found to be different. The viscosity curve, although it might appear at first as a typical relaxation curve which could be described by Eq. 3.2, is not exactly so. If a relaxation, the same curve should have been obtained upon increasing or decreasing the shear rate. Instead, these results reveal the existence of a critical shear rate beyond which the glass structure becomes shear-thinned and resulting in a lower viscosity.

Finally, the structural characteristics of the TZN network and its changes with temperature suggest an explanation for the shape of the Angell viscosity curve for fragile glasses. As shown in Figure 3.7, the viscosity increases more slowly (lower slope) than that of strong glasses at high temperature (left side of the plot) but faster (steeper slope) than that of strong glasses at lower temperature (right side of the plot). In an Arrhenius model, this behavior can be ascribed to a lower activation energy at higher temperature and higher activation energy at lower temperature, due to cross linking between chains. Therefore, tellurite glass may be said to exhibit a viscosity behavior like that of certain polymers, possibly due to the large anisotropy of its elongated basic $TeO_4$ molecular unit, forming chains at higher temperatures that can cross link at lower temperatures. Because of this, TZN exhibits a variable activation energy and higher fragility index compared to strong glasses such as $SiO_2$ or $GeO_2$ in which the bonding and short range network structure evolves very little with temperature, exhibit relatively constant activation energies and an Arrhenius-type behavior over the whole temperature range above $T_g$ and lower $m$ values (20 and 24 respectively). Since their $m$ values are less than 35, these glasses are termed "strong" while the $m$ value of TZN with a fragility index of 78±7 can be considered to be a "fragile" glass ($m$ between 50 to 150) [25]. The TZN glass also has

a much higher fragility index than glasses with a similar composition $80TeO_2.10Li_2O-10Na_2O$ but no zinc, which has a fragility index equal to 41. This indicates that alkalis are stronger glass modifiers than Zn, which is also partially a glass former element, as shown by the existence of crystalline forms such as $Zn_2Te_3O_8$. Furthermore, for glasses with composition (80 mol $TeO_2$ -(20-x) mol $LiO_2$-x mol $Na_2O$, the fragility index m ranges from 41 for $80TeO_2-10Li_2O-10Na_2O$ to 57 for $80TeO_2-20LiO_2$ glass. This further indicates that mixed alkali-tellurite glasses are less fragile than the single alkali-tellurite ones such as $TeO_2-LiO_2-$ glass [36], possibly due to the different sizes of the alkalis. It is also interesting to compare TZN with monomers and oligomers of polystyrene (PS), polydimethylsiloxane (PDMS) and polyisobutylene (PIB) whose fragility ranges varies from 60 to 90, and specifically with poly(dimethylsiloxane), having a fragility of 79 [37], i.e. similar to that of the TZN.

### 3.6    Summary

The viscosities of tellurite glass with composition $75TeO_2-20ZnO-5Na_2O$ (TZN-75) and $75TeO_2-15WO_3-8Na_2O-2Nb$ (TWN-Nb) have been measured as a function of shear rate and temperature. TWN-Nb glass is selected for the sole purpose to illustrate the shear thinning behavior in glasses and the parameters such as relaxation time, activation energy and fragilty which were obtained in TZN-75 case are not obtained for TWN-Nb. TZN and TWN-Nb are seen to behave as a newtonian fluid (elastically) up to a critical shear rate, $\dot{\gamma}_c$ but only TWN-Nb is seen to shear-thin beyond (visco-elastic). Viscosity of TZN-75 drops abruptly with respect to shear rate along with the decrease in shear stress indicating the slippage of the sample from the parallel plates, for all temperatures

investigated except at 618 K. Dynamic frequency sweep experiments were conducted at 5% strain resulting in gradual drop in viscosity compared to abrupt drop as in the case of steady shear viscosity. The flow behavior of the TZN glass can be described using power law having power law index equal to $0.7\pm0.1$ and consistency factor decreases with increasing temperature. These parameters would be useful in the numerical modeling of tellurite glass extrusion through the die discussed in chapter 5. In other words, full relaxation in the glass takes place before $\dot{\gamma}_c$, but the relaxation is not reversible beyond $\dot{\gamma}_c$ i.e. the structure does not remain the same at all shear rates and in both directions. This is clearly revealed by the fact that at shear rates up to $\dot{\gamma}_c$, higher activation energy was obtained exhibiting a fully connected network structure and rearrangement of the network structure took place without breaking bonds, simply by change of local configuration; while, a lower activation energy was obtained beyond $\dot{\gamma}_c$ exhibiting visco-elastic stretching and breaking of bonds leading to a permanent decrease in viscosity or shear-thinning. In the temperature range inestigated, an Arrhenius-type equation provides a good fit to the temperature dependence of both the viscosity and the relaxation time. The activation energy for flow and the fragility near $T_g$ are about $200\pm20$ kcal/mole and $78\pm7$ respectively, which makes TZN a fragile glass when compared to "strong" vitreous silica glass with a fragility of 20. Because of the large anisotropy of its elongated basic $TeO_4$ molecular unit, tellurite glasses may be compared to polymers, which also have a relatively high fragility index.

# CHAPTER 4

## EXTRUSION OF TELLUITE GLASS PREFORMS

### 4.1 Introduction

In Chapter 4, fabrication of round tube and three-spoked HF performs from the bulk tellurite glass by extrusion are presented. The basic composition of the glasses considered was $75TeO_2.20ZnO.5Na_2O$ (TZN-75), because it possesses good formability and offers good optical properties but other tellurite glass compositions were also extruded. TZN-75 glass billets were extruded at different temperatures in the TZN-75 glass transition region using a laboratory press. The extruded preforms with precise geometrical features, an excellent surface quality and no crystallization were achieved in the temperatures range from 338 to 346°C (viscosity range from $\sim 2 \times 10^7$ to $5 \times 10^6$ Pa.s) and at ram speeds ranging from 0.002 to 0.01 mm/s. Glasses extruded at viscosities less than $10^6$ Pa.s compromised the geometrical and dimensional integrity of the preforms. Optical inhomogeneities in the form of flow lines were observed in the cross-sections of the preforms extruded at viscosities near $2 \times 10^7$ Pa.s at the ram speeds mentioned above. The flow lines were eliminated by extruding the glass at viscosities ranging from $9 \times 10^6$ to $5 \times 10^6$ Pa.s. Thus, subsequent extrudates were successfully fabricated without flow lines, providing good optical homogeneity that yielded solid and holey fibers that could provide much improved optical performance.

## 4.2    Experimental Method

### 4.2.1    Glass Extrusion Operation
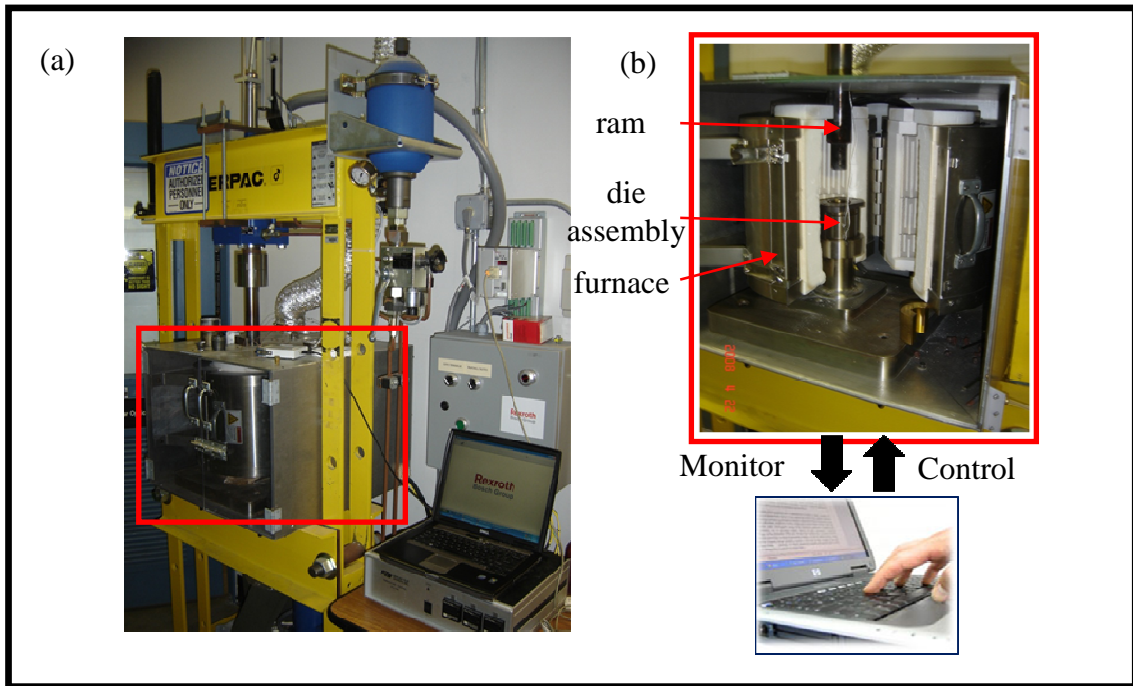


**Figure 4.1** (a) The laboratory vertical glass extrusion press and (b) the tooling assembly inside the furnace

A vertical laboratory glass extrusion press was designed, fabricated and set up for this research by Hongsheng Xiao [12] as shown in Figure 4.1 (a). It is equipped with a furnace for heating the glass billet (furnace marked in red rectangle in Figure 4.1 (a) and enlarged picture shown in Figure 4.1 (b)) and a motion controller connected to a computer for controlling the ram travel. The press maximum load is 300 kN and the ram can travel from 0 to 150 mm with a speed as low as 0.001 mm/s. The temperature inside the furnace is controlled to the desired extrusion temperature by adjusting the temperature

setting of three furnace rings. The billet along with the entire die assembly is situated at the center of the furnace as shown in Figure 4.1 (b) and shown schematically in Figure 4.2 (a).

Two thermocouples are employed to measure the temperatures of the extrusion die ($T_1$) and the container ($T_2$) and to make sure that the extrusion temperature is maintained within the expected range. Once a stabilized extrusion temperature is achieved, the press begins to extrude the glass billet at a temperature in the glass transition region.
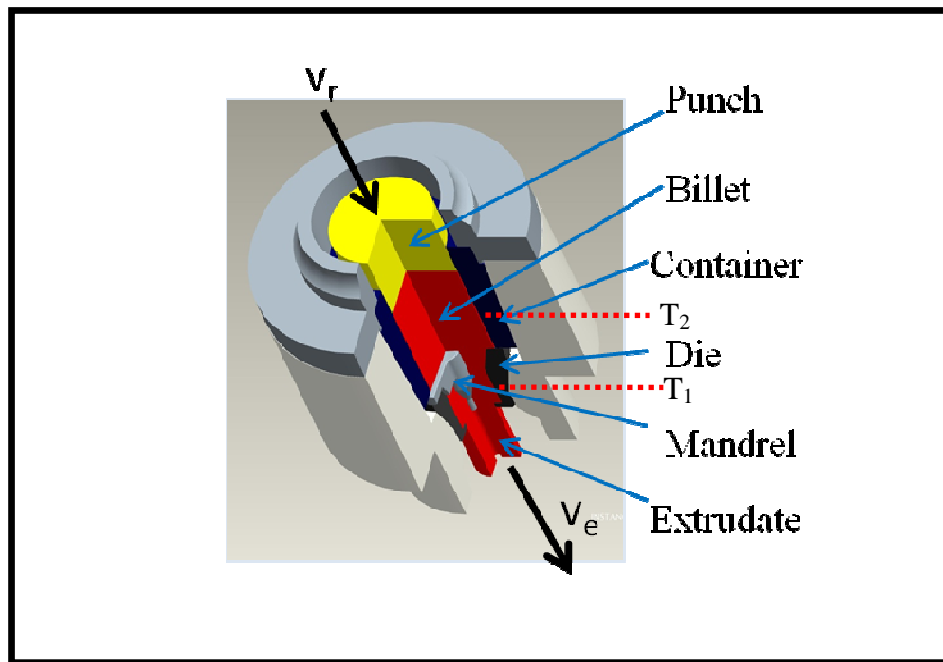


**Figure 4.2** Model of the die assembly used for the extrusion of tube preform

The punch speed is accurately controlled during the extrusion as per the experimental requirements by BODAC software. Typically, three sets of ram speeds ($v_r$) are used: 0.002, 0.003 and 0.01 mm/s. Depending on the height of the billet, the ram is

allowed to accelerate until the punch gets very close to the top of the billet. The speed is then reduced to an intermediate level as soon as the punch touches the billet. Thereafter, the ram speed is reduced to the experimental speeds so as to maintain the requirement of a low strain rate in glass extrusion. The viscoelastic glass experiences deformation (compaction and stretching) when forced through the die clearance formed by the die opening and the mandrel as shown in Figure 4.3 (a) top view because of the high extrusion ratio ($R$) which is the ratio of the areas of the billet ($A_0$) to the exit ($A_e$) of the die (Figure 4.3 (b)) and in the case of spider die, it's about 11.6. $R$ determines the strain induced in the viscous glass flowing through the die.



Die top view

Die bottom view

(a)

$$R = \frac{A_0}{A_e}$$

(b)
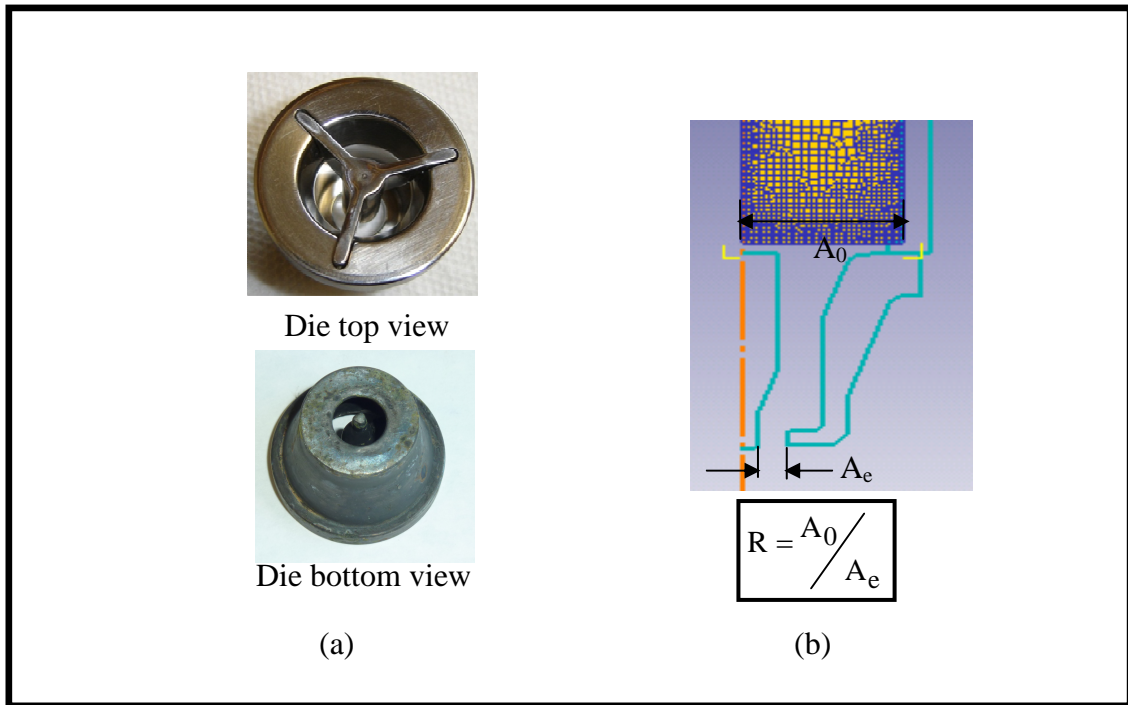
**Figure 4.3** (a) Top and bottom view of the spider die used for extrusion of tube preforms (b) 2D side profile of the die depicting the extrusion ratio

53

In the tube extrusion, as the glass is compressed into the die, the load starts to increase. Once the glass exits the die, it's a steady state extrusion and the load remains constant throughout the extrusion until the end where the load increases exponentially (Figure 4.4). The exponential increase is caused because of the crystallization induced due to high load and also because of the end portion of the glass billet being exposed to the extrusion temperature for the maximum amount of time inducing crystallization. It is also seen that load increases with decreasing extrusion temperature and increasing ram speed as demonstrated from many experiments [38].
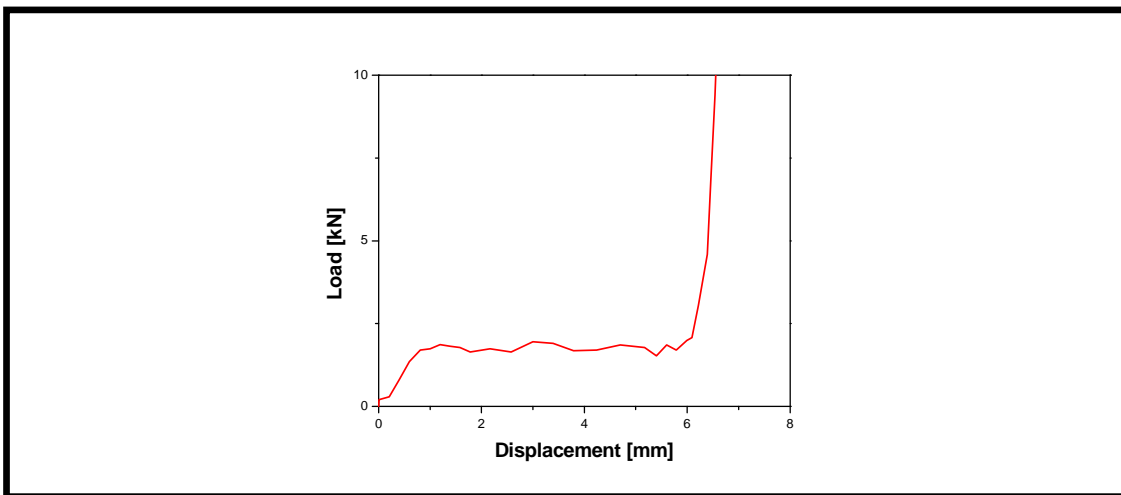


**Figure 4.4** A typical load curve in case of tube extrusion

## 4.3    Extrusion Parameters

In the extrusion of glass, the forming parameters such as temperature, extrusion ratio, extrusion speed and tooling design are appropriately selected so that severe induced tensile stress would be avoided and the preform obtained is free of surface imperfections and crystallization. For an amorphous material to be extruded, the billet should be heated above its glass transition temperature $T_g$, and below its crystallization temperature $T_x$,

54

where the materials can be deformed by viscous flow under shearing stress. Below $T_g$, generally amorphous material will be very brittle and could not be plastically deformed; above $T_x$, the material would crystallize and cannot hold its amorphous state. Similar to polycrystalline materials, in the deformation of amorphous materials, the forming limit of the materials should not be exceeded either, or cracks will occur in the material. So glass is normally extruded at a temperature between $T_g$ and $T_x$ so that it can be readily deformed, under the hydrostatic compressive state of stress. In order to avoid severe induced tensile stress which would cause internal cracking or surface tearing, the appropriate extrusion parameters including temperature, strain, strain rate, tooling design, and lubrication should be properly selected. The extrusion temperature is the temperature measured at the die. The strain ε is determined by the die design, and with the fixed die design, the ram speed determines the strain rate. The extrusion load results from the combined effect of the factors such as temperature, strain, ram speed, and frictional condition. In an extrusion experiment, extrusion load is an important indicator of the deformability of the glass under the conditions of the test. Sometimes, it is possible to obtain different extrusion loads for preforms extruded at the same extrusion temperature and ram speed; almost all of those times, higher optical inhomogeneity would be observed at the higher extrusion load.

### 4.3.1 Extrusion temperature

Mechanical drawing of the die assembly with the furnace is shown in Figure 4.5 (a) and a typical extrusion temperature curve for TZN-75 is shown in Figure 4.5 (b). Temperatures are measured at two locations: thermocouple 1 measures the temperature at liner or the

55

container and thermocouple 2 measures at the die as shown in Figure 4.5 (a). There is a temperature difference between these two measured temperatures and it's ~25°C over 30 mm vertical distance between two measured locations. The extrusion experiments were conducted at several different temperatures between $T_g$ and $T_x$. But the temperature curves shown in Figure 4.5 (a) are for the extrusion temperature of 343°C. The temperature drops by two degrees as the ram starts to push the glass through the die when the ram absorbs some of the heat from the hot glass to lower the extrusion temperature (Figure 4.5 (a)). The extrusion temperature in the furnace is controlled through controlling the temperature of the three ring furnace (Figure 4.5 (a)) with the help of furnace controller. At the start, temperatures are set as 360-460-620°C for furnace rings 1-2-3 respectively for 1 hour till the temperature is around 10~15°C below the desired extrusion temperature. The temperature is reduced to temperatures ranging from 590 to 610 °C for ring 3 and from 460 to 440~450°C for ring 2 of the furnace. Ring 1 temperature is not reduced. With the current tooling setup and the furnace design, the desired extrusion temperature is reached in about 150 minutes.

(a)



(b)
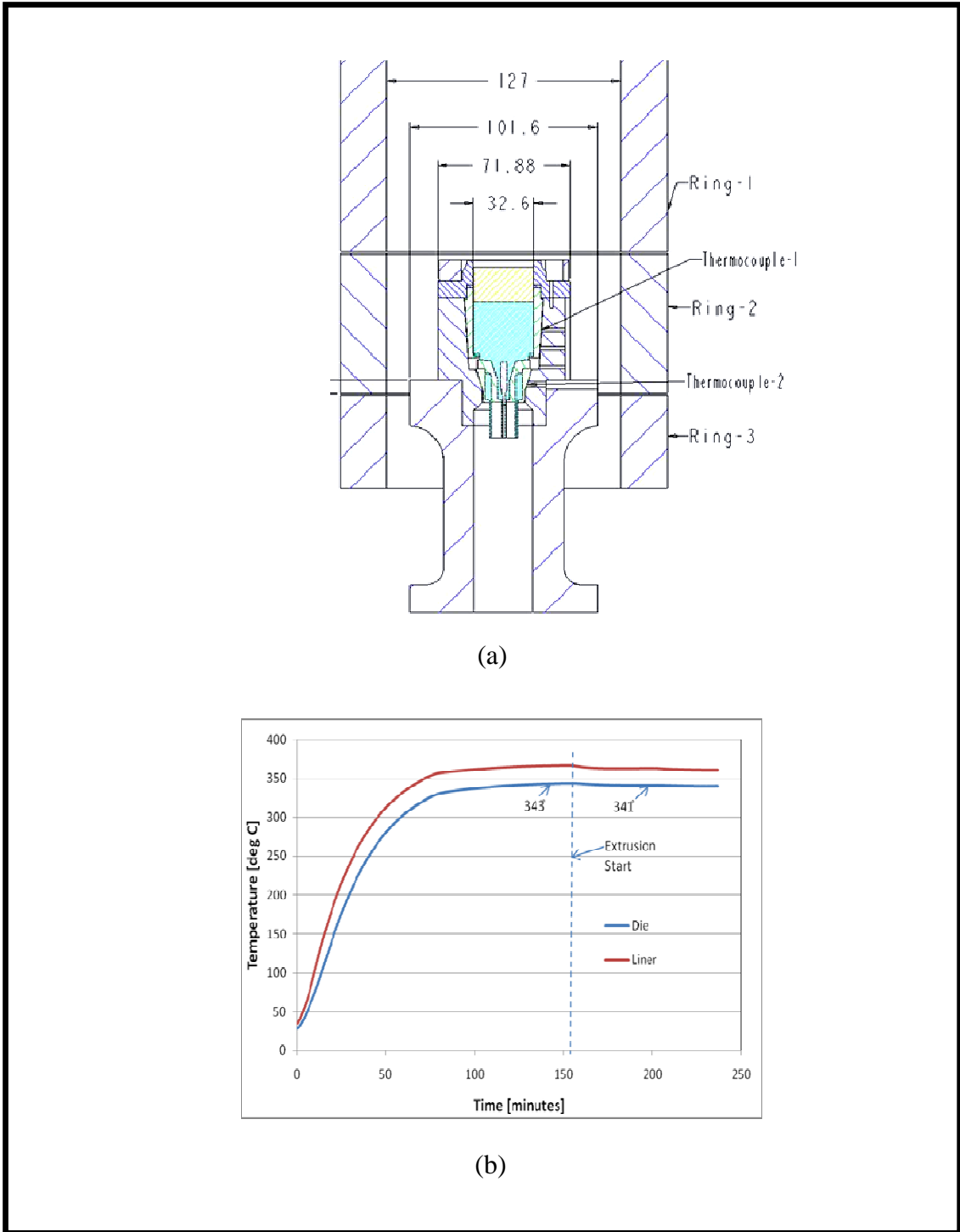
**Figure 4.5** (a) Extrusion die assembly with furnace [12] and (b) a typical temperature distribution in the furnace from the beginning of the billet heating to the end of the extrusion

57

### 4.3.2 Strain ε

A practical measure of the deformation in the extrusion process is the extrusion ratio R which is defined earlier in the chapter. It is a macro measure of strain but very practical in analyzing the extrusion process. It does not show the true strain. The tube extrusion experiments were performed with R≈12. So the engineering strain $e$ is 11/12=0.917 and the true strain can be expressed as ε= ln(R)= ln(12)= 2.485 or ~250%.

### 4.3.3 Friction/ Lubrication condition f

Since the glass extrusion was carried out at high temperatures, a high temperature-resistant, high toughness Ni-based superalloy (Inconel-635) was selected as the tooling material. The tooling is made from Lamm's Machine LLC, Allentown. When the die set is new, its surfaces are highly polished and shiny; the friction is negligible. After a number of experiments, the material starts to form pits seen on the liner and the punch shown in Figure 4.6. Even so, the extrudate preforms have excellent surface quality and optical finish using the tooling shown in Figure 4.6.
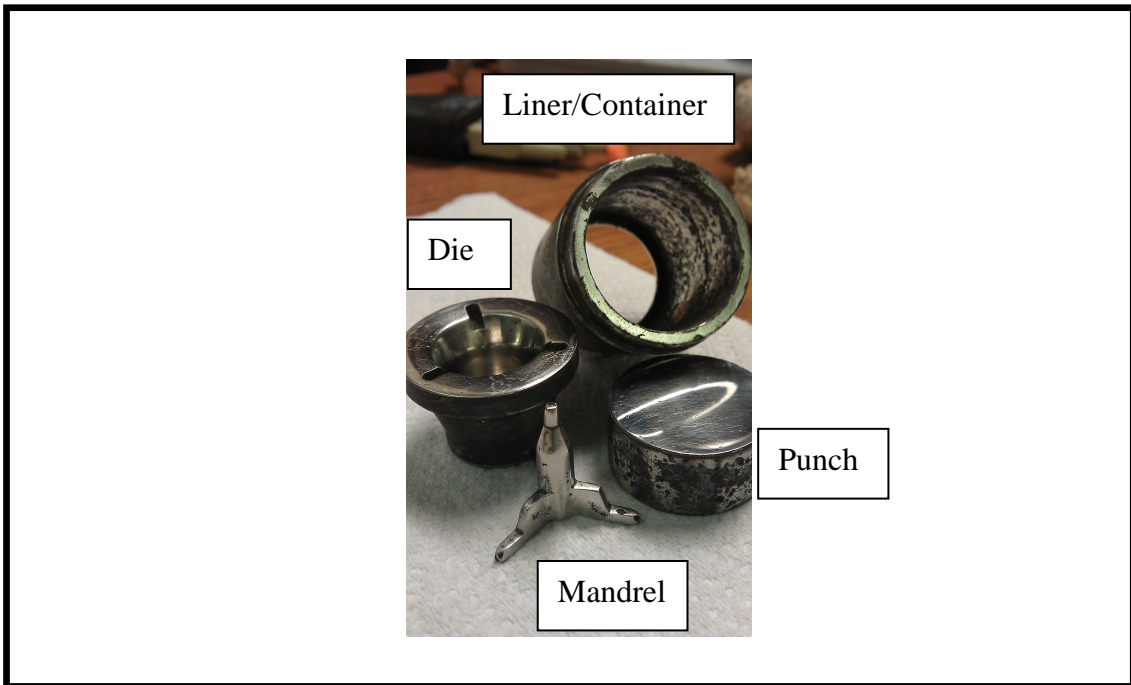
**Figure 4.6** Extrusion die assembly exhibiting the surface finish/friction conditions

Outer surfaces of the die and liner are coated with a high temperature lubricant (BN, boron nitride, ZYP coatings) so that the tooling can be easily disassembled at the end of the extrusion.

### 4.3.4 Strain or shear rate $\dot{\gamma}$

Strain rate or shear rate depends on the tooling geometry and the ram speed used in the extrusion. Determination of the shear rate for the spider die at various extrusion parameters is conducted numerically and the results are shown in Chapter 5. Strain rate can also be determined analytically using relationship given in the literature [39].

## 4.4    Deformation Mechanism

There are two deformation modes for glass forming in the temperature range between $T_g$ and $T_x$. The Newtonian flow or linear stress flow is called when a glass is deformed at lower strain rates and the flow stress $\tau$ is normally linear to strain rate $\dot{\gamma}$:

$$\tau = \eta_N \dot{\gamma} \tag{4.1}$$

where, $\eta_N$ is the Newtonian viscosity of the glass at the deformation temperature.

The other condition is Non-Newtonian flow when glass is deformed with a strain rate above some critical strain rate value $\dot{\gamma}_c$, the linear relationship of equation (4.1) can no longer be retained. Normally, the viscosity of glass is decreased with increased strain rate. This phenomenon is called Non-newtonian flow.

The Newtonian flow mode or Non-Newtonian flow mode are the results of the balance between the relaxation and accumulated deformation under shearing, and the relaxation is also based on atomic diffusion mechanism.  So the flow modes are both temperature and strain rate dependent. The Figure 4.7 shows the dependence of deformation modes on the temperature and strain rate.
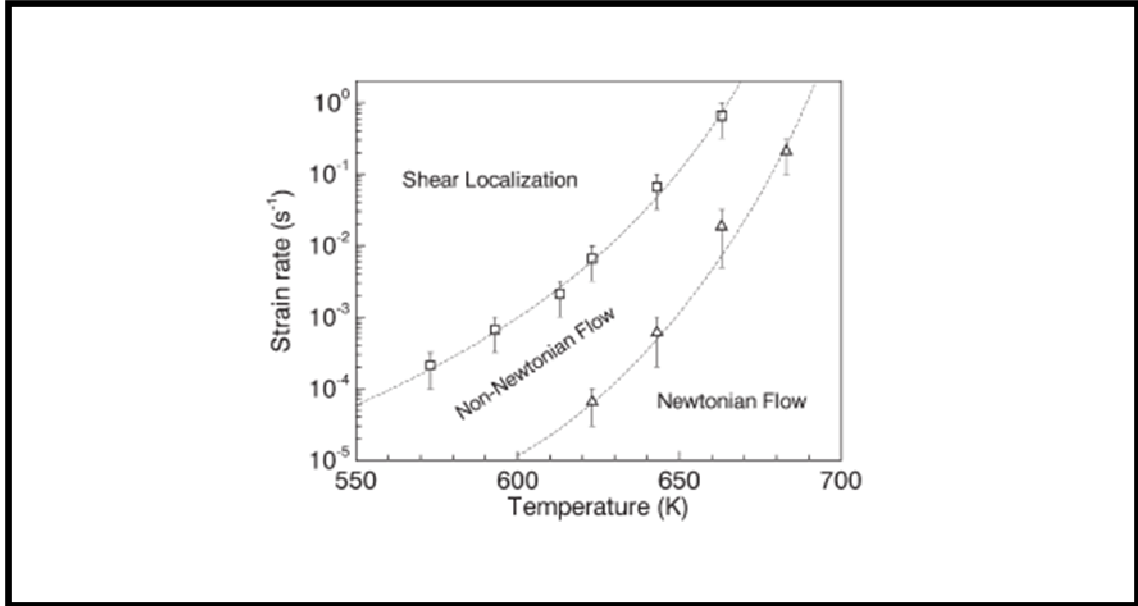
**Figure 4.7** Selection of temperature and strain rate range for glass deformation [40]

## 4.5    Experimental Method

Tellurite glass billet preparation is already described in Section 2.2. Differential scanning calorimetry (DSC) was performed to determine the extrusion temperature range between the glass transition temperature, $T_g$ = 573 K, and the onset of crystallization, $T_x$ = 680 K, as reported in Chapter 3 [41]. The viscosity of the glass was also measured, using an advanced rheometric expansion system (ARES) in a parallel plate configuration between 609 K and 663 K as a function of shear rate from 0.01 to 10 $s^{-1}$. As the glass sample was sheared, two different flow modes were observed, newtonian at lower shear rates and non-newtonian or shear thinning at higher shear rates. The extrusion could then be performed in the appropriate range where the glass can be viscously deformed without crystallization. Temperatures from 617 K to 633 K and shear rates from 0.01 to 1 $s^{-1}$ were

determined as appropriate for extrusion of our glasses. Ram speeds were accordingly selected to vary from 0.002 to 0.01 mm/s.

Besides temperature and ram speed, the two other critical parameters in the glass extrusion process are the degree of friction and die geometry. Friction is mainly determined by the billet geometry, its surface quality and by the die design and die material. Friction between the supercooled glass and the die was minimized by cleaning and polishing the die thoroughly using selected polishing papers each time before extrusion to ensure a smooth finish of the tooling walls.

## 4.6     Experimental Results

Figure 4.8 (a) and (b) shows tube and HF preforms extruded from TZN-75 glass at temperatures in the glass transition region. The outer and inner diameters of the tube preforms were 10 mm and 3 mm respectively and the lengths varied from 80 to 150 mm depending on the size of the billet. The front end of the extrudate was always curved due to non-uniform process conditions at the beginning of extrusion, which resulted from a non-uniform velocity distribution. However, once the steady state process conditions were reached, the extrudate came out straight as seen in Figure 4.8 (a) and (b). The surface quality of both the preforms was excellent. The HF performs have a core diameter, spoke length and spoke thickness of approximately 3 mm, 6 mm and 0.2 mm respectively. The HF preform design is inspired by an earlier one proposed [9, 42]. This design is based on the index guiding principle and a simple microstructure having high index glass core and large air-filled holes surrounding it. The core guides the light and

large air-filled fraction efficiently confines the light in the center core. The center core is held by three spokes having thickness 0.2 mm that also support the outside wall that confines the air-holes. Due to such thin features as the spokes, the losses from the solid core could be negligible compared with the inherent losses from the material itself [42].
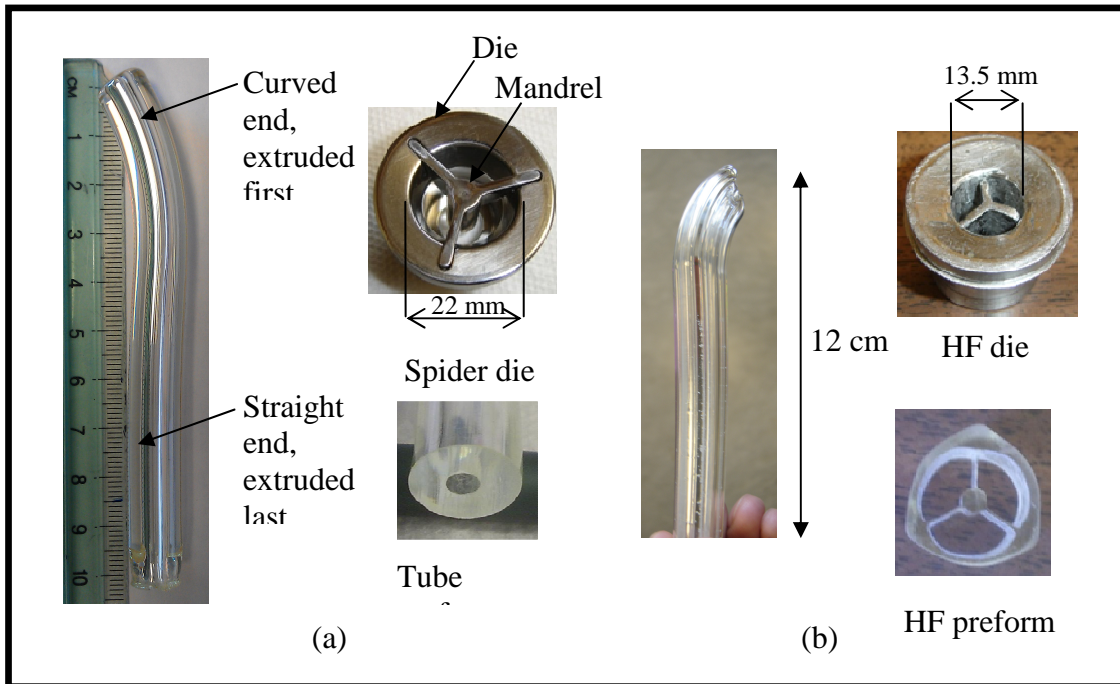


**Figure 4.8** Examples of extruded TZN-75 preforms (a) tube preform along with the spider die used for its creation and (b) HF preform and the die used

In this research, extrusions were performed both for tube and HF preforms; the flow analysis was conducted only on tube preforms. So, in the following section, tube preform results will be discussed. Figure 4.9 shows the load during the extrusion of tube preforms at temperatures 338°C, 342°C and 346°C each extruded at ram speeds 0.002 mm/s, 0.003 mm/s and 0.01 mm/s. At 338°C, the load increased from 1.5±0.25KN at 0.002 mm/s to 2±0.25 KN at 0.003 mm/s and then increased to 4.25±0.25KN at 0.01

mm/s ram speed and appeared to further increase slightly at the end of the extrusion. At 342°C, the load increased in the same manner with the ram speed but decreased as the temperature increased to 342°C. The loads measured during the extrusion at temperatures 338 °C and 342 °C are given in the following table.

**Table 4.1** Extrusion Load in KN at different temperatures and ram speeds

| $T_{extrusion}$ [°C] | Ram Speed (mm/s) | | |
|---|---|---|---|
| | **0.002** | **0.003** | **0.01** |
| **338** | 1.5±0.25 | 2±0.25 | 4.25±0.25 |
| **342** | 1±0.25 | 1.5±0.25 | 3.75±0.25 |

Note that in the Figure 4.9, load increased during the extrusion performed at 346°C especially at 0.01 mm/s ram speed. This is because of the glass billet heated for too long inducing crystallization in the preform. If the billt would be heated for the ideal amount of time(120~150 minutes),there would not be crystallization at 346°C and load would be in the range of 2 kN to 3 kN  for 0.01 mm/s ram speed.
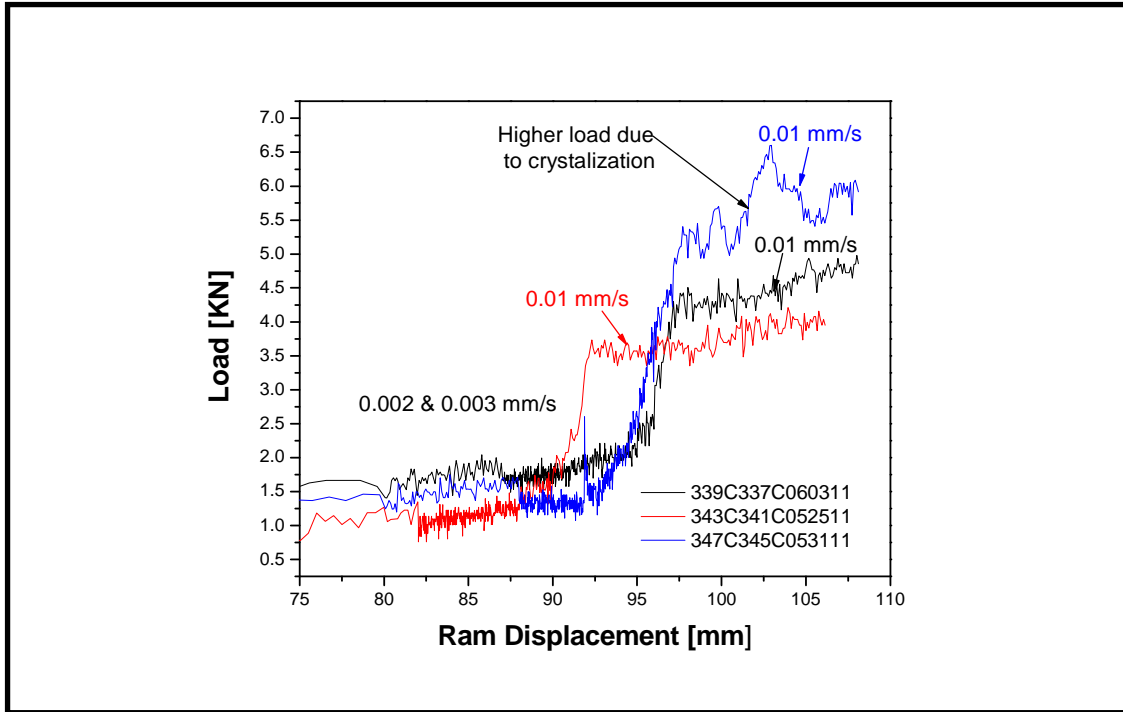
**Figure 4.9** Experimental result of load with respect to ram displacement at temperatures 338°C, 342°C and 346°C with varying ram speeds of 0.002 mm/s, 0.003 mm/s and 0.01 mm/s

Figure 4.10 (a) shows optical microscope images of the cross-sections of tube-preforms extruded at 338, 342 and 346°C at varying ram speeds. From Figure 4.10 (a), the flow lines (FL) can be seen at 338°C at 0.003 mm/s. If the ram speed increased from 0.003 to 0.01 mm/s, FLs are expected to increase in number. This is due to the higher shear rate experienced by the glass near the die walls with increasing ram speeds. Figure 4.10 (b) and (c) shows optical image of the cross-section of the tube preform extruded at 342°C at 0.002 and 0.003 mm/s ram speeds. No FLs were observed. The lower load resulted in the elimination of flow lines. Figure 4.10 (d) shows optical image of the cross-section of the tube preform extruded at 346°C at 0.01 mm/s. Again, No FLs were seen. Since at 346°C at higher ram speed, flow lines were not seen, they would not be expected at lower ram speed as well.
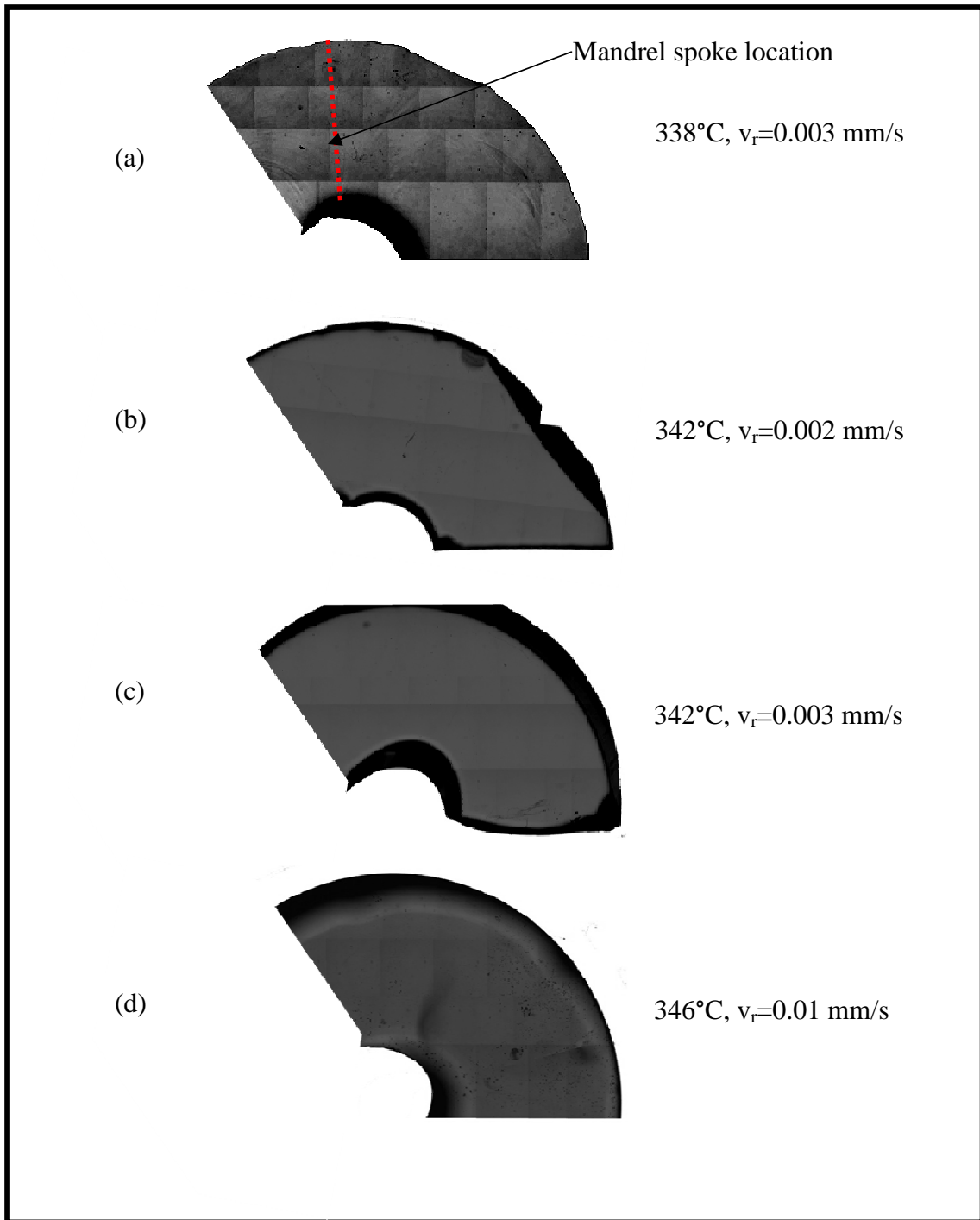
**Figure 4.10** Optical images of cross-sections of tube preforms extruded at temperatures 338°C, 342°C and 346°C with varying ram speeds of 0.002 mm/s, 0.003 mm/s and 0.01 mm/s

Figure 4.10 shows the dependence of FLs on temperature. The FLs were eliminated as

the extrusion temperature increased from 338 to 342°C. FLs could be possible at higher

ram speed 0.01 mm/s at 342°C but the extrudate could not be obtained at those parameters at this point. At 346°C, even for 0.01 mm/s, no FLs were seen. It turns out that as the temperature is increased further, the glass would flow easily without FLs even for higher ram speeds that 0.01 mm/s. But when the temperature increased above 355°C ($\eta < 10^6$ Pa.s), the glass becomes so less viscous that the preform is stretched as in fiber drawing and dimensional integrity is compromised. As shown in Figure 4.11, the preform is stretched to more than a foot of length and its tapered.



**Figure 4.11** Tube preform extruded at 358°C

## 4.7    Discussion

Higher loads lead to greater shear rate and increasing shearing of glass near both the die wall and the mandrel interface, giving rise to more FLs in the extrudate, as shown in Figure 4.10. In all the extruded preforms, the glass flow is laminar while flowing through a convergent channel like the tube or the HF die. The glass that flows through the central part of the channel between the mandrel and die wall experiences the lowest shear and therefore moves the fastest while the glass flowing near the die wall or mandrel surface experiences an opposing friction force. This results in a velocity gradient, the higher

velocity being found at the center of the channel and the slower near or at the outer walls. The resulting flow due to the velocity gradients causes shearing of individual glass laminae with neighboring ones forming layers, the outermost layer (nearest to the die wall) experiencing the highest shear thus the flow lines are captured by the light optical microscope shown in Figure 4.10 (a). These experimental extrusion results and their interpretation are further supported by a simple numerical simulation of the glass extrusion shown in Figure 4.12. This simulation was carried out using DEFORM 2D FEM software for the glass extruded at 340 ˚C at ram speed of 0.003 mm/s.
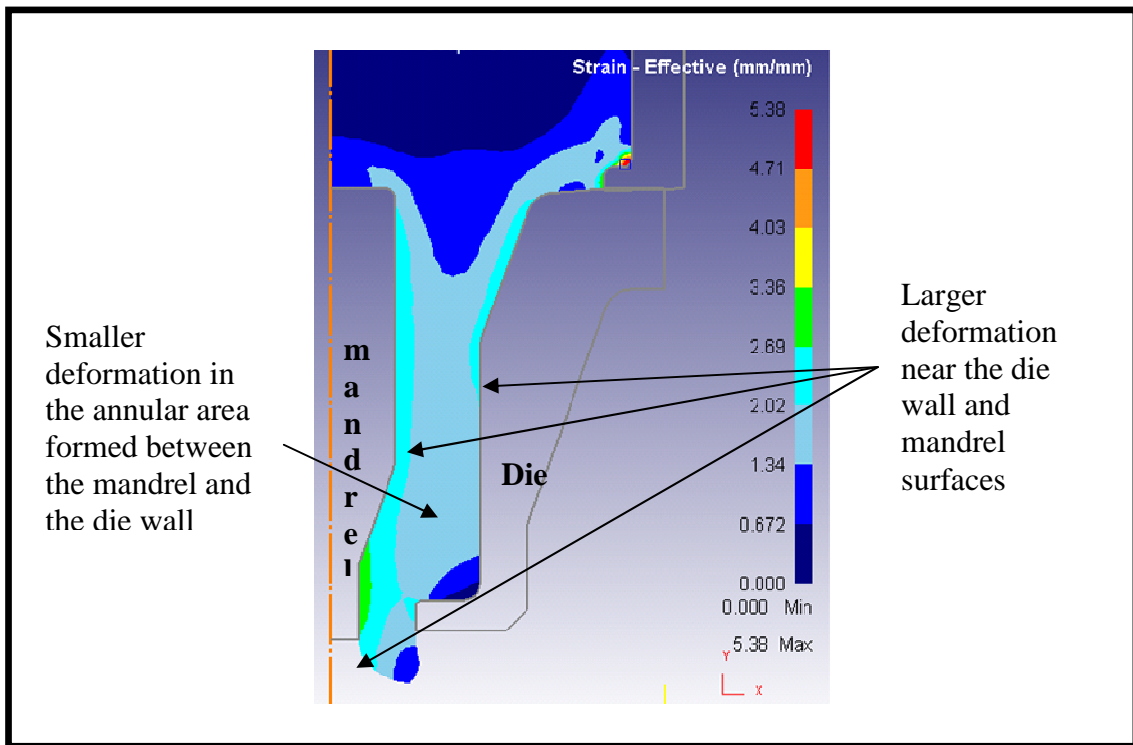


**Figure 4.12**.Axi-symmetric glass extrusion simulation using DEFORM 2D showing localized strains or deformations of glass flowing through the extrusion die. Larger deformations are observed in the glass near the die wall and mandrel surfaces as compared to the glass flowing through the central part of the annular channel between them.

68

The figure shows strain distribution in the glass flowing through the die during the extrusion process. As shown in Figure 4.12, larger deformation is in the glass which is nearest to the mandrel interface and the die wall, while relatively smaller deformation is observed in the glass flowing through the central part between the die wall and mandrel. This explains and supports the observation of a greater number or higher density of shear bands near the die wall and mandrel interface.

The continuous decrease in the extrusion load with increasing temperature (Figure 4.9) is due to the fact that, as the extrusion temperature increases, the viscosity decreases resulting in a lower resistance to glass flow. This suggests that, even though the shear rate is the same in all cases, the magnitude of the shear near the die wall is lower at higher temperature due to the lower value of the glass viscosity, resulting in fewer FLs or as shown in Figure 4.10.

In the case of the preform exhibiting FLs, the extrusion temperature (338°C) was not far enough above the glass transition temperature, $T_g$, where the glass is still in the supercooled liquid state. The flow lines or the shear bands are seen in the preform because the glass structure relaxes at a relatively slower rate and does not have enough time to anneal out the shear bands, thus retaining them even after the preform exits the die. However at higher temperature 346°C, the structure relaxes at a much faster rate than at 338°C and the FLs therefore have sufficient time to anneal out before the glass cools down and fully solidifies. As shown in Figures 4.10 (b), (c) and (d), these tube preforms are without FLs and can provide good optical homogeneity to produce fibers with improved optical performance.

# CHAPTER 5

## Numerical Analysis of Tellurite Glass Flow in the Extrusion of Tube Preforms

### 5.1    Introduction

Tellurite glass possesses advantageous optical properties, first and foremost good optical transmission in the mid-infrared, but also higher linear refractive and much higher nonlinear index and other nonlinear coefficients [3] and stronger and broader rare-earth emission [1] than silica glasses. Most importantly, tellurite glass possesses better thermal stability and chemical durability than the chalcogenide glasses that have been extensively investigated. Finally, because they are soft, and have low melting temperature, tellurite glasses are easier to form than silica. These properties make tellurite glass particularly attractive for mid-IR fibers with a variety of geometries, solid core/clad and microstructured, which can be used in fiber lasers and amplifiers for optical communications or fiber sensors for environmental and bio-medical applications.

Extrusion is a very convenient and versatile method for fabricating tellurite glass preforms because extrusion is a one step, reproducible, high yield process. It is a particularly useful technique for fabricating microstructural preforms with complex profiles such as photonic crystal preforms containing air holes that can be used to tailor the dispersion and polarization properties of fibers, enhance their nonlinearities, and thus open the way for a variety of new optical functionalities.

In our previous paper [38], we reported on the fabrication of round tube and three-spoked HF preforms from bulk tellurite glass with composition $75TeO_2.20ZnO.5Na_2O$ (TZN-75). This composition was chosen because it has good formability and possesses

good optical properties. Optical inhomogeneities in the form of "flow lines" (FLs) were reported at 344°C, increasing in intensity and contrast with increasing ram speeds from 0.002 mm/s to 0.01 mm/s. An optical micrograph of the cross-section of a tube preform is shown in Figure 5.1. FLs result in spatial variations of the refractive index of the glass, which become visible because of the optical contrast between more and less dense parts of the glass in the preform. These FLs are formed due to shearing of the supercooled glass near the mandrel and die wall shown in Figure 5.1 (b). It is interesting to note that the FLs near the die walls are not continuous but form loops between the mandrel supports. These supports are responsible for the formation of the weld lines visible in Figure 5.1 (a). When the extrusion temperature was increased from 344 °C to 360 °C, fewer FLs were seen. Due to low viscosity at 360°C, the viscous glass flowed under its own weight stretching longitudinally thereby showing gradual variation in the diameter and also exhibited variation in the geometrical features in the HF preforms. This was not reported in the paper. The optical inhomogeneity was reduced but at the expense of geometrical integrity.

(a)
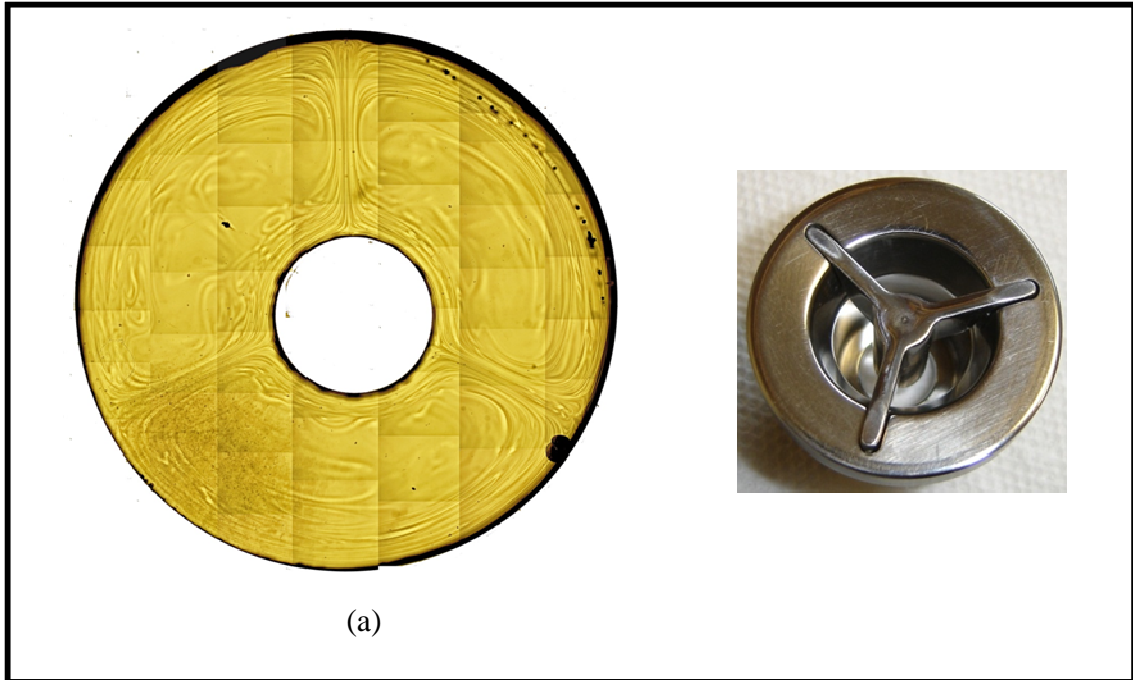
**Figure 5.1** (a) Tube preform with flow lines (b) Extrusion die to fabricate preform shown in (a)

In order to analyze the effect of these FLs on the optical properties of the formed glass, we measured the Rayleigh/Raman scattered light from the billet and compared it with the intensity of the scattered light from the extruded preform. The preform containing FLs scattered more light than the billet because of greater optical inhomogeneities shown in Figure 5.2. More light would be transmitted through the preform and the subsequently drawn fibers if the scattering is minimized. Thus, elimination of flow lines is very important in the fabrication of low loss optical fibers. In this paper, we performed extrusion experiments to produce tube preforms at temperatures 338°C, 342°C and 346°C at ram speeds of 0.002 mm/s, 0.003 mm/s and 0.01 mm/s and report that preforms free of FLs with excellent geometrical integrity were obtained.
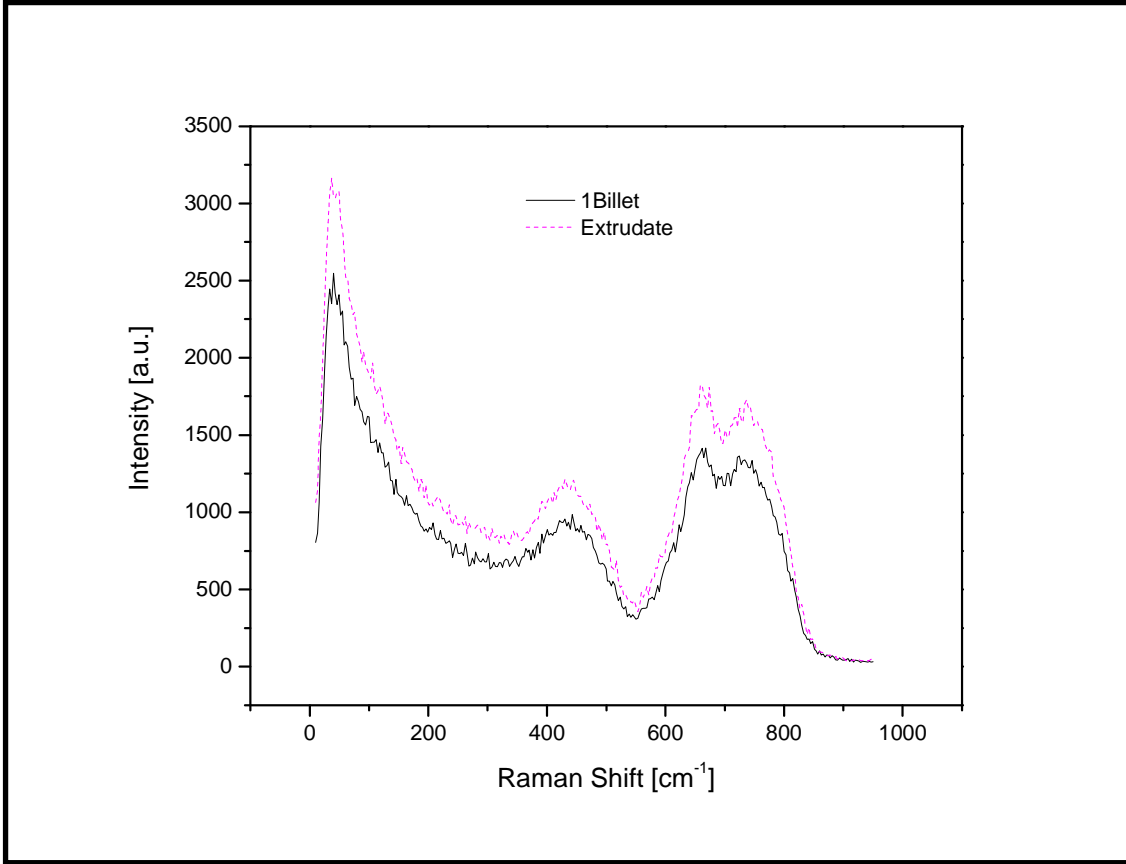
**Figure 5.2** Comparison of scattered light intensities from TZN-75 glass billet and extrudate

We theoretically analyzed the flow of tellurite glass through the extrusion die and developed a numerical model that described the tube extrusion fairly well. Rheological parameters that were used in the development of the model were obtained by performing oscillatory shear tests in a parallel plate configuration. In the modeling, we obtained shear rate and shear stress distribution shown to be directly linked to the formation of flow lines. A deformation map was constructed for the extrusion of TZN-75, which shows the shear stress distribution for given extrusion conditions and helps choose the extrusion parameters for preforms free of FLs.

## 5.2     Materials and Methods

TZN-75 glass preparation along with preparation of TZN-75 billet and samples for parallel plate rheometry tests are described in our previous papers [38, 41]. Steady shear tests were conducted because the steady-state shear rheological properties determine the flow property of the glass and are critical to understanding and modeling extrusion. In our previous paper, we performed steady-state shear tests of TZN-75 using parallel plate rheometry where we measured the viscosity of the TZN-75 glass with respect to shear rate in the glass transformation region from $T_g \approx 307°C$ to $T_x \approx 413°C$. The details of the experiment are given in a previous paper [41]. In steady-state shear tests, the samples can undergo structural deformation or surface crystallization at high temperature and high strain rates. On the other hand, in oscillatory shear tests, the magnitude of the strain remains small and thus the intrinsic rheological properties can be accurately measured. These measurements were useful in obtaining the rheological parameters needed for the extrusion modeling. Before performing dynamic frequency tests to determine the range in which the viscosity of the TZN-75 does not depend on the applied strain, dynamic strain sweep measurements were performed.

### 5.2.1   Flow Analysis of Tellurite Glass through the Tube Extrusion Die

We now describe the flow analysis of viscous TZN-75 glass through the extrusion tube die. The die set is shown in Figure 5.1 (b). The crosss-section of the preform is shown in Figure 5.1 (a). As described earlier, due to the mandrel spokes, the flow is divided into three symmetrical sub-flows, each confined by two mandrel spokes 120° apart and the outer die wall. Thus, the tube extrusion die can be considered to be consisting of three simple tapered rod extrusion dies comprised of two mandrel walls and an outer die wall.

We considered one such die as shown in Figure 5.3 (a). The entry and exit cross-sectional geometric profile of this die were approximated to diameters $D_1$ and $D_2$ respectively using the hydraulic diameter definition:

$$\text{Hydraulic Diameter} = 4*\text{Area/Perimeter} \qquad (5.1)$$

Figure 5.3 (b) shows forces acting on a cylindrical element of the glass flowing through the die. Simple force balance led us to obtain:

$$\frac{\partial P}{\partial z} \equiv P_z = \frac{2\tau}{r}$$

$$(5.2)$$

using assumptions:

1. No variation in $\theta$ direction

2. Steady state $\dfrac{\partial}{\partial t} = 0$

3. Incompressible

4. Fully developed flow $\dfrac{\partial}{\partial z} = 0$

5. No body force

6. Pressure is a function only in the z-direction
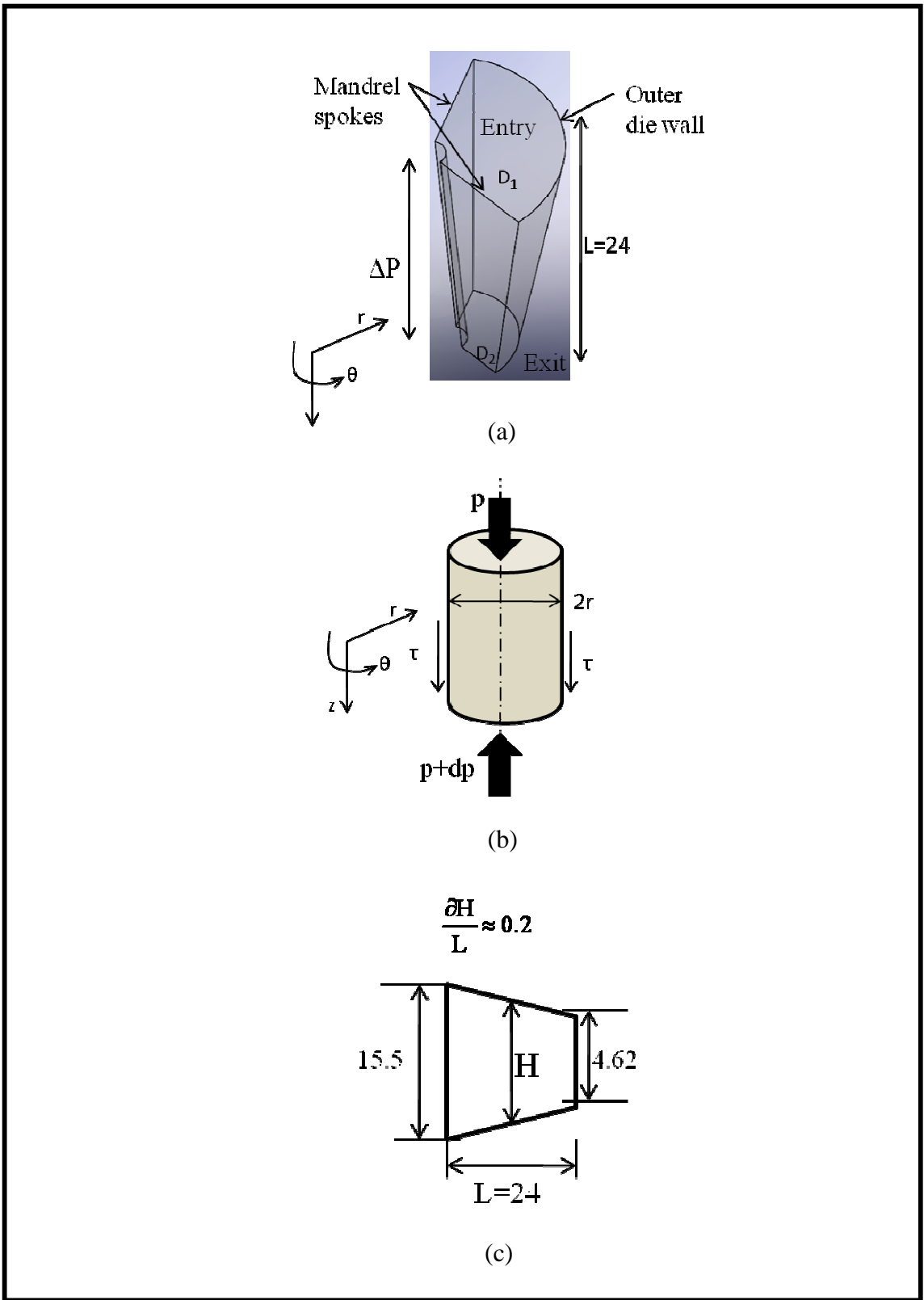
**Figure 5.3** (a) Die section considered for modeling (b) Typical cylindrical element in the glass flow (c) Fully developed flow approximation

Further simplification gives the pressure difference in the flow direction as:

$$\Delta P = \frac{kP_{z1}LD_1}{-3n(D_1 - D_2)}\left[(\frac{D_2}{D_1})^{-3n} - 1\right]$$

(5.3)

where $P_{z1}$ = pressure gradient at die entry

$L$ = die length

$D_1$ = hydraulic diameter at entry = 15.5 mm

$D_2$ = hydraulic diameter at exit = 4.62 mm

$n$ = power law index

$k$ = correction factor equal to 3/5 for the tellurite glass extrusion

Details of the model are given in the reference [43]. For the fully developed flow assumption, small die taper with $\partial H/L$ of 0.2 or less is required. In this case, the die is short and $\partial H/L$ is about 0.45 shown in Figure 5.3 (c). Nonetheless, we considered the approximation of the fully developed flow for the sake of simplification.

From the model, we obtained $\Delta P$ and $P_{z1}$ at the die entry for all given temperatures and ram speeds. The model was compared with the experimental results. The parameters $P_{z1}$, $\Delta P$ calculated from the flow analysis and C and n from the dynamic shear tests were used in the numerical model to derive resulting shear rates and shear stresses in the extrusion die.

### 5.2.2   Formulation of the Numerical Model

We consider the same geometry of the die as shown in Figure 5.4. Here, we consider the Cartesian coordinate system. In the flow analysis discussed in the previous section, we

considered pressure as the function of x alone (flow direction) because we were interested in calculating the pressure difference and pressure gradient along the length of the die. In the numerical modeling, we are interested in calculating velocity u, velocity gradient $\frac{\partial u}{\partial \psi}$ and shear stress distribution at different cross-sections of the extrusion die. Thus, velocity, u=u(y,z) and similarly p=p(y,z) where flow is in x-direction. Note that the extrusion die is tapered and thus the velocity and pressure are going to increase as the diameter is decreased (Figure 5.4). Therefore,

$$u = u_1(y,z) + \varepsilon u_2(x,y,z) \tag{5.4}$$

$$p = p_1(y,z) + \varepsilon p_2(x,y,z) \tag{5.5}$$

where ε is a perturbation parameter.
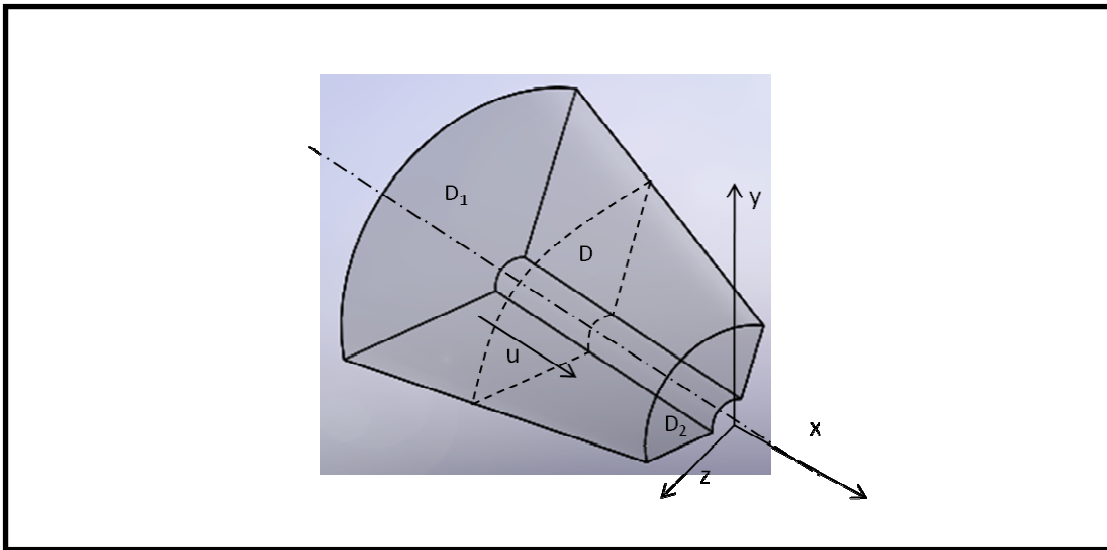


**Figure 5.4** Extrusion die geometry considered for the numerical model

Here, same assumptions were made as in the flow analysis section 5.2.1. With those

approximations, the Navier-Stokes equation was simplified to have the form:

$$\frac{\partial^2 u_2^*}{\partial y^{*2}} + \frac{\partial^2 u_2^*}{\partial z^{*2}} = -16\frac{\dfrac{\partial P_2}{\partial x}}{\dfrac{\partial P_1}{\partial x}}$$

(5.6)

With,

$$\frac{\dfrac{\partial P_2}{\partial x}}{\dfrac{\partial P_1}{\partial x}} = \left[\frac{D_2}{D_1}\right]^{-1-3n}$$

(5.7)

Equation 5.6 was solved using the Partial Differential Equation Toolbox in Matlab. The

relation given equation 5.7 was obtained from the reference [43].

## 5.3　　Results
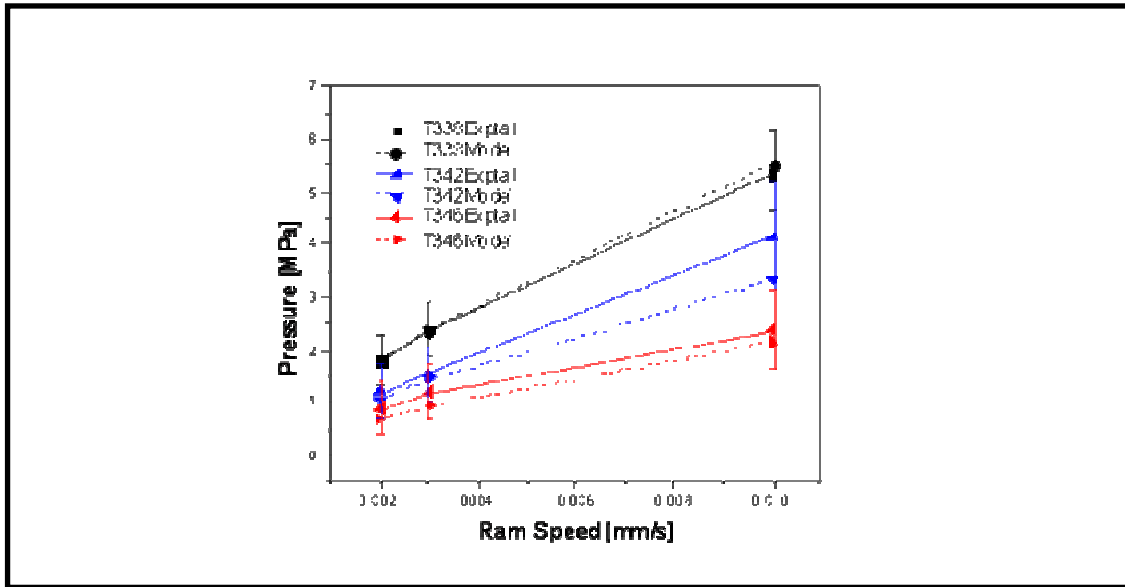


**Figure 5.5** Comparison of experimental results and model for the pressure difference in the extrusion die

The loads were converted into pressure and compared with the model from equation 5.3. The comparison of experimental results and the model are shown in Figure 5.5. Taking into account the correction factor k, the model is in good agreement with the experimental results within the experimental error. The values of the pressure gradient at the given temperatures and ram speeds were used in the numerical model to calculate the shear rate and shear stress distribution within the extrusion die.

Note: If the flow is considered Newtonian (n=1), the calculated pressure gradients and pressure difference values are smaller than that calculated using n equal to 0.7. This will cause the subsequently modeled shear stress and shear rate distribution values smaller compared to the values calculated at n equal to 0.7. These values when compared with the steady and dynamic shear experiments fall clearly within the linear shear stress

regime. The shear stress values calculated using n equal to 0.7 lie within the transition region of linear and non-linear shear stress and therefore more interesting in our case.
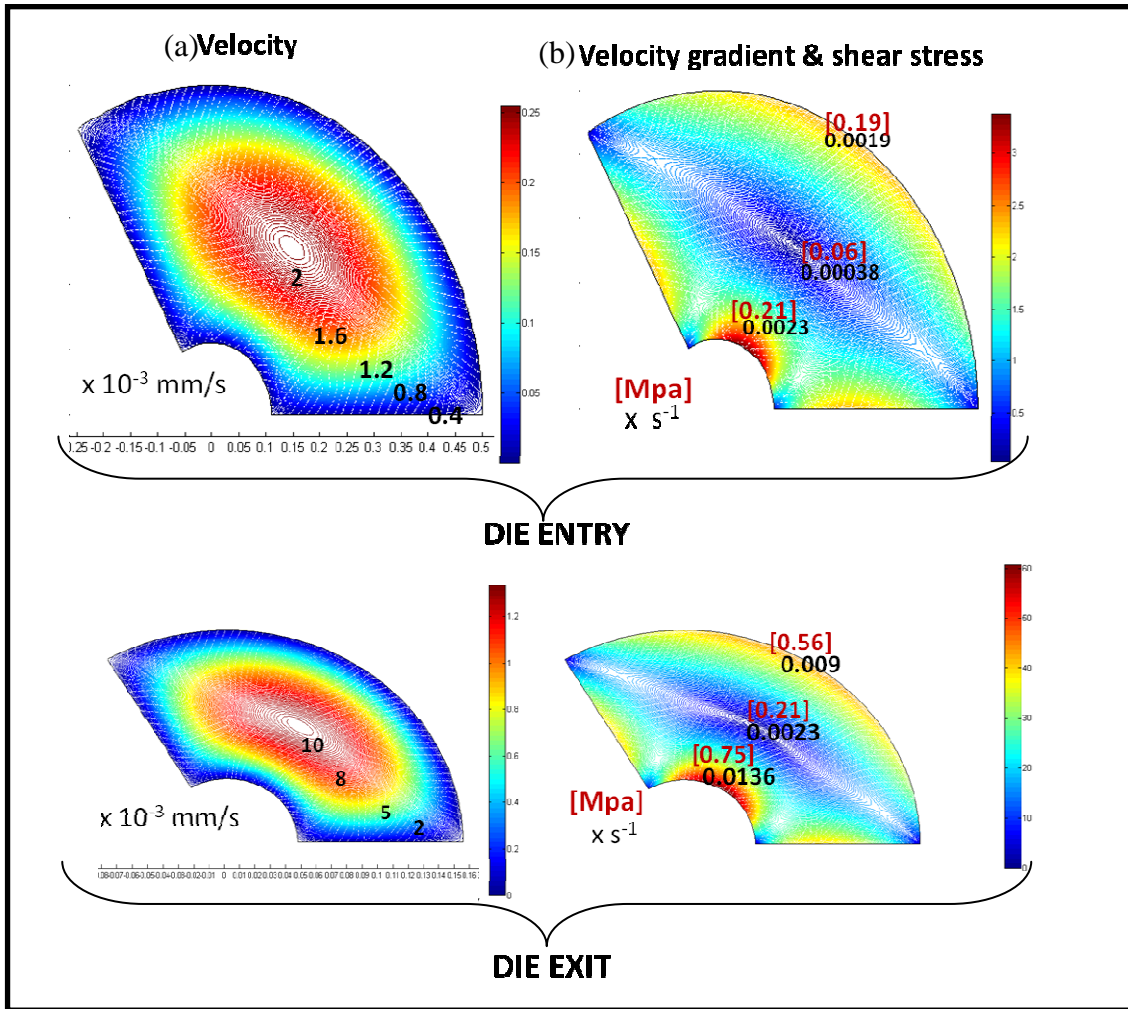


**Figure 5.6** (a) Velocity (b) velocity gradient and shear stress distribution in the entry and exit of the die at 338°C extruded with 0.002 mm/s ram speed.

Figure 5.6 (a) shows velocity (u) and Figure 5.6 (b) shows velocity gradient $(\partial u / \partial \varphi)$ and shear stress $(\tau)$ distribution for 338°C at 0.002 mm/s ram speed at the entry and exit cross-sections of the die. u, $(\partial u / \partial \varphi)$ and $\tau$ increased from entry to exit. The actual $(\partial u / \partial \varphi)$ values were calculated from the dimensionless $(\partial u / \partial \varphi)$ shown in equation 5.8

81

where $\dfrac{\partial P_1}{\partial x}$ was calculated from the flow analysis and using $(\partial u / \partial \varphi)$, the actual $\tau$ distribution was calculated using equation 5.9 where *C* and *n* values were measured from the dynamic shear tests described in chapter 3. The equations are given as following:

$$\frac{\partial u}{\partial \varphi} = \frac{\partial u^*}{\partial \varphi^*} \frac{D}{16\eta}\left(-\frac{\partial P_1}{\partial x}\right)$$

(5.8)

and

$$\tau = C\dot{\gamma}^n$$

(5.9)
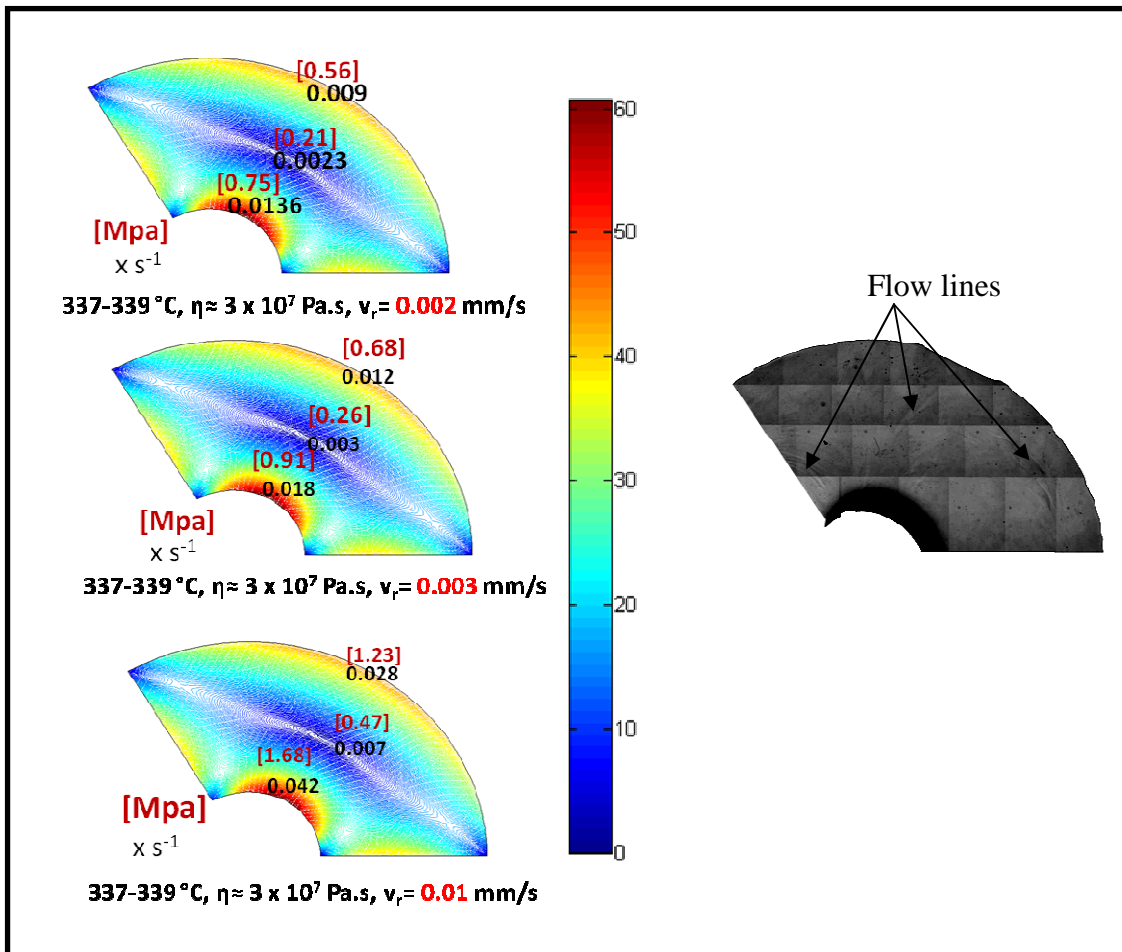


**Figure 5.7** Comparing the flow lines with the shear stress distribution at 338°C

82

As the ram speed increased from 0.002 mm/s to 0.01 mm/s, the largest $\tau$ at the die exit increased from 0.75 MPa to 1.68 MPa shown in Figure 5.7. Similar results of $\tau$ and ($\partial$u/ $\partial\varphi$) increase with the increase in ram speed were found at temperatures 342 and 346°C shown in Figures 5.8 and 5.9 respectively. Although as the temperatures increased from 338 to 346°C, shear rate nearly remained the same but the shear stress decreased.



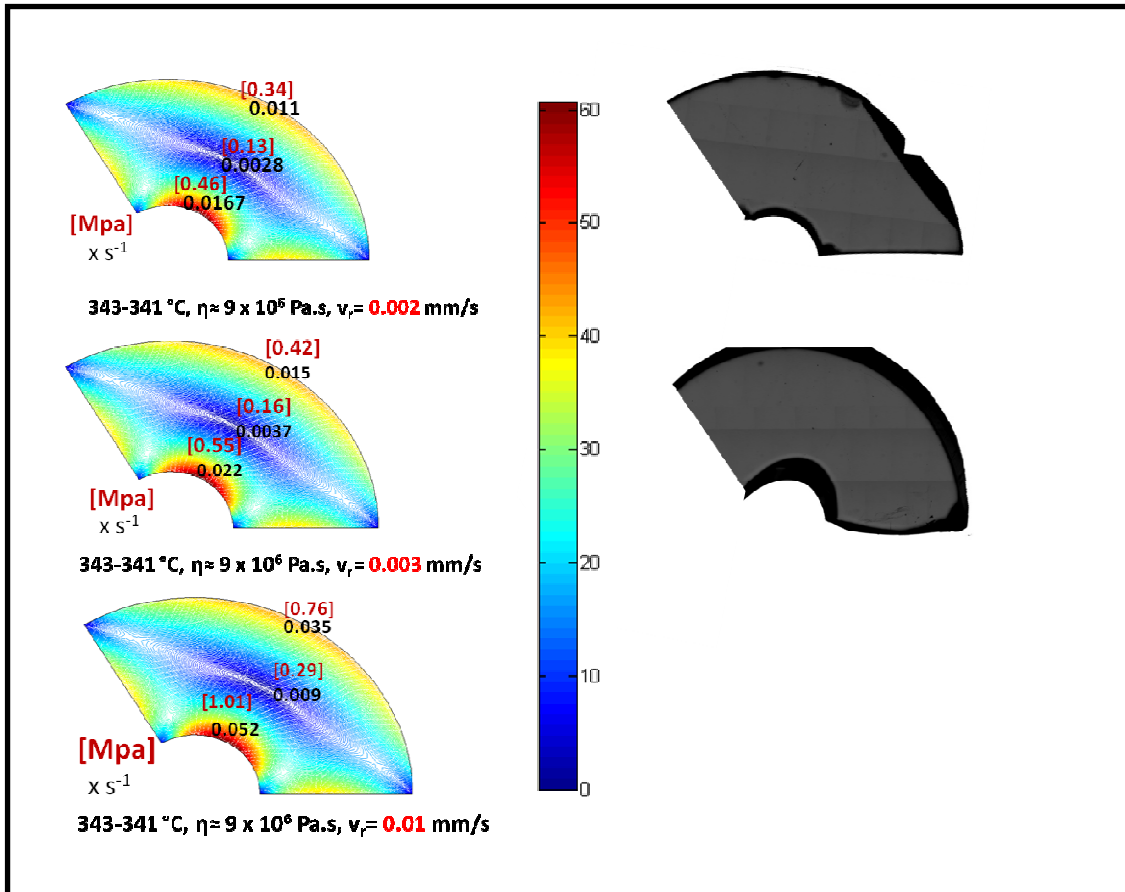**Figure 5.8** Comparing the flow lines with the shear stress distribution at 342°C

The tube preforms extruded at temperatures 338°C, 342°C and 346°C from 0.002 mm/s, 0.003 mm/s and 0.01 mm/s were investigated for existence of FLs. Micrographs of the tube preforms extruded at these temperatures and ram speeds were compared with the

83

modeling results shown in Figures 5.7, 5.8 and 5.9. Flow lines were seen in the preform extruded at 338°C at 0.003 mm/s ram speed. The corresponding largest shear stress at was 0.91 MPa and avarge shear stress near the preform walls was 0.8±0.12 MPa. Thus, shear stress of 0.8±0.12 MPa can be considered to cause flow line formation in the preform. At higher ram speed of 0.01 mm/s, average $\tau$ is approximately 1.45±0.23 MPa and expected to have even higher number of FLs compared to the one at 0.003 mm/s. $\tau$ at 0.002 mm/s ram speed is 0.65±0.1 MPa and the flow lines status is not determined at this point. Although, it was predicted using an extrusion forming diagram which is constructed and described in the later section.

Preforms extruded at 342°C at 0.002 and 0.003 mm/s ram speeds were optically homogeneous i.e. no FLs were present (Figure 5.8). The corresponding average shear stress at 0.002 and 0.003 mm/s ram speed at 342°C are 0.4±0.06 and 0.48±0.07 MPa respectively. These shear stress values can be considered not to induce any FLs. FLs status in the preform at 0.01 mm/s could not be established at this point although the corresponding $\tau$ was calculated to be 0.88±0.13 MPa which was greater than the shear stress observed at 338°C at 0.003 mm/s ram speed thus creating a possibility of FLs presence. This is also predicted using the extrusion forming diagram.

At 346°C, no FLs were observed at 0.003 mm/s ram speed (Figure 5.9) even though the extrusion load was much higher than anticipated due to crystallization. The $\tau$ was 0.29±0.05 MPa. The $\tau$ at 0.01 mm/s ram speed was 0.52±0.07 MPa and thus no FLs expected to be present.

Using the above information for the $\tau$ distribution and the corresponding micrographs of

the preforms with and without FLs, an estimation of the critical $\tau$ to obtain performs free

of FLs could be made by constructing the extrusion flow diagram.
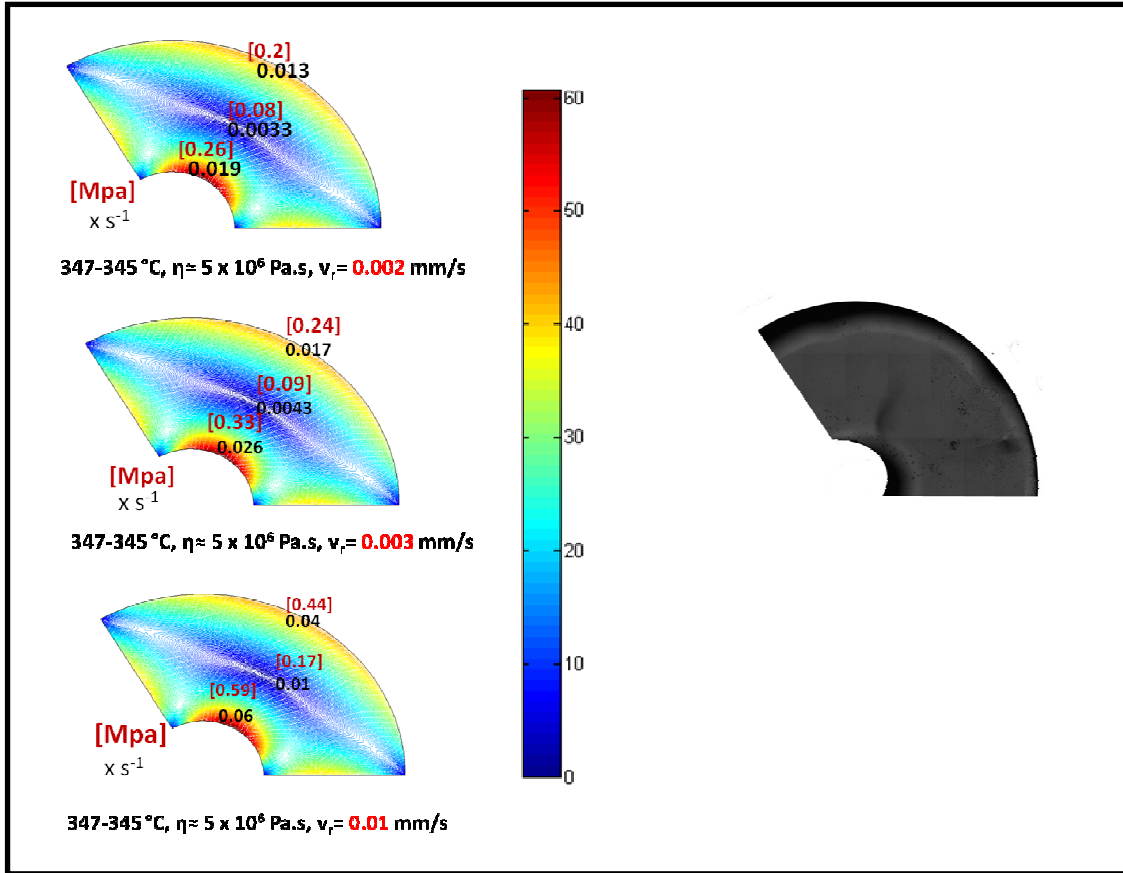


**Figure 5.9** Comparing the flow lines with the shear stress distribution at 346°C

Before constructing the extrusion forming diagram, it was important to compare

the shear stress modeling results with the shear stress obtained through the dynamic shear

tests in order to see in what region the modeled shear stresses lie. Figure 5.10 shows

shear stress obtained through dynamic shear tests at 5% strain. The tests were conducted

for temperatures from 350 to 365°C. Since the extrusion were conducted at temperatures

338, 342 and 346°C, dynamic shear stress results were extrapolated to show shear stresses at 335, 340 and 345 °C as shown in Figure 5.10. Now comparing the shear stress values and the flow lines in the micrographs from the Figures in 5.7, 5.8 and 5.9 with the shear stress results in the dynamic shear test of Figure 5.10, Table 5.1 was created.



**Figure 5.10** Dynamic shear experiment at 5% strain

**Table 5.1** Comparison of shear stress in the numerical modeling and dynamic shear experiments. Flow lines are predicted by observing these shear stress values with the micrographs of preform cross sections shown in Figures 5.7, 5.8 and 5.9.

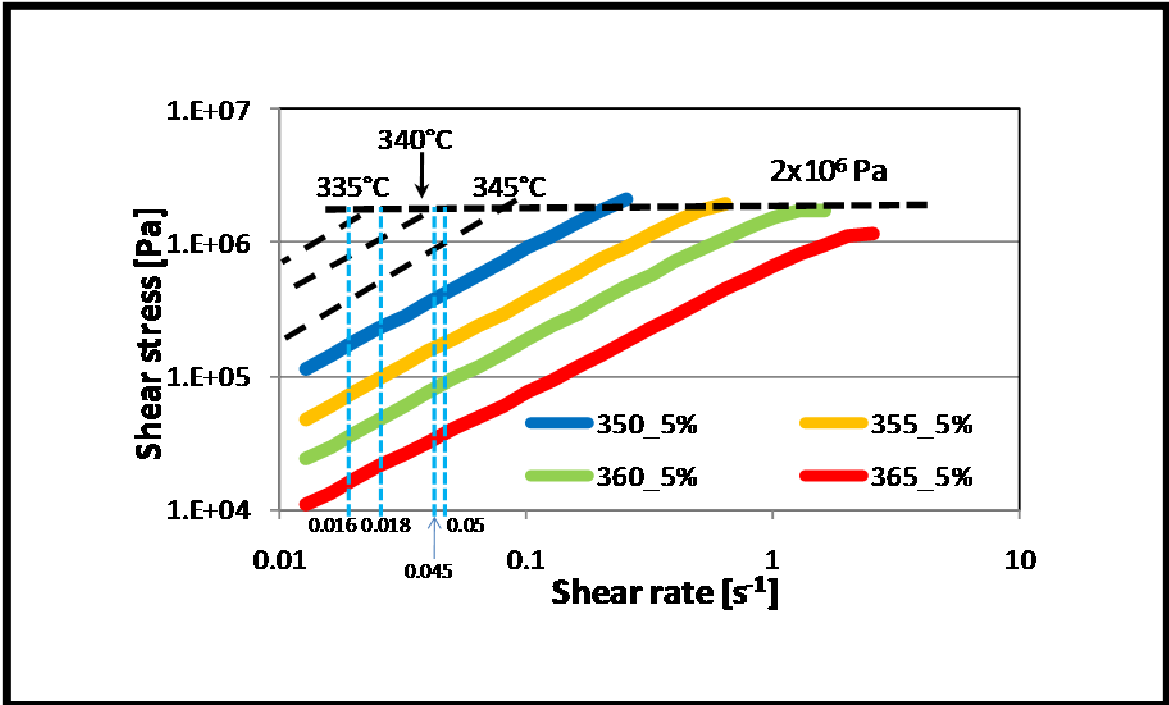| Ram speed [mm/s] | Temperature [°C], shear rate [s⁻¹] | Shear stress [MPa], at 5% strain | Flow lines | Shear stress [MPa], modeling results |
|---|---|---|---|---|
| 0.003 | 338, 0.016 | 0.88 | Observed | 0.8±0.12 |
| 0.003 | 342, 0.018 | 0.56 | None | 0.48±0.06 |
| 0.01 | 342, 0.045 | 1.43 | Likely | 0.88±0.12 |
| 0.01 | 346, 0.05 | 0.85 | Unlikely | 0.52±0.08 |

In Table 5.1, the first and second columns show extrusion conditions, also depicted in Figure 5.7-5.9. For example, 1st row shows extrusion conditions 338°C and ram speed of 0.003 mm/s as shown in Figure 5.7. At these extrusion parameters, flow lines were observed and thus so mentioned in column 4. Shear stress obtained through numerical modeling fiven in column 5 was compared with the shear stress obtained through the dynamic shear stress results obtained through Figure 5.10. Column 2 also denotes the shear rate at which the shear stress was measured and is mentioned in Figure 5.10. In the top two rows of the Table 5.1, judgment were made on the flow lines status whether FLs are present or absent since the micrographs of the preforms extruded at the mentioned conditions are at hand. But in the next two rows, predictions were made on the status of the FLs from the shear stress values obtained from the model as well as from the dynamic shear tests. In the third row at 342°C and ram speed of 0.003 mm/s (refer Figure

5.8), prediction of presence of FLs was likely because of high shear stress calculated through the model and the dynamic tests. Notice the large difference between the shear stress values (1.43 MPa in dynamic testing to $0.88\pm0.12$ MPa from the model); this is addressed in the following paragraph.

When the dynamic shear stress results were compared with the steady shear stress results, steady shear stress was always observed to be less than shear stress in the low strain dynamic shear tests. This is because the strain is high enough in steady shear to break down inter- and intra- molecular association in the glass structure [34]. Thus, the steady shear stress is even smaller than the shear stress values depicted in column 3 of Table 5.1. These values would tend towards the shear stress values obtained through modeling and thus they are employed in constructing the extrusion forming diagram.
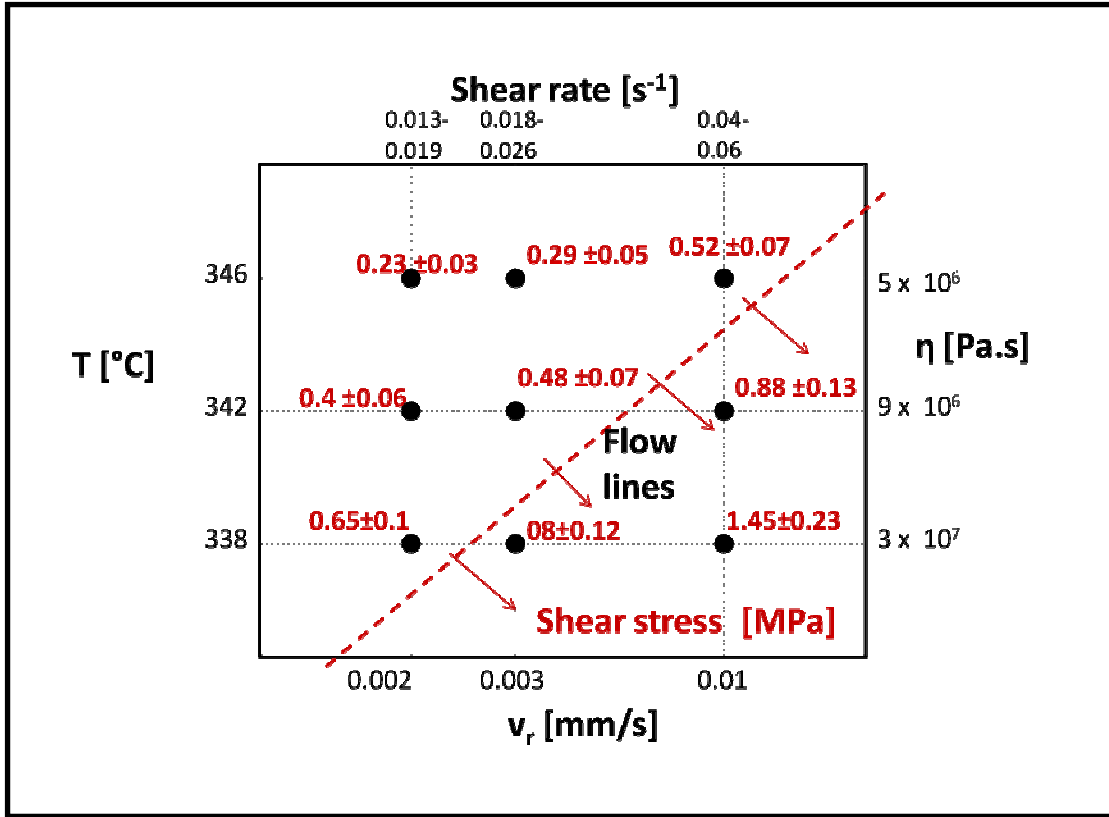
**Figure 5.11** Extrusion forming diagram for TZN-75 showing shear stress distribution at the extrusion parameters predicting flow lines formation

Figure 5.11 shows extrusion forming diagram for TZN-75 glass in which the $\tau$ values corresponding to given extrusion conditions were plotted. It is predicted that the FLs are possible at 342°C for ram speed of 0.01 mm/s but are unlikely at 346°C for the same ram speed. Therefore, a critical $\tau$ line is drawn on the map which marks the line above which homogeneous preforms could be obtained, free of FLs. Thus, the extrusion forming diagram can be a useful tool in the extrusion of TZN-75 in order to obtain tube preforms free of FLs.

## 5.4    Coclusion

Flow analysis of viscous TZN-75 glass through the simplified extrusion die was described. Through the analysis, the pressure gradient and pressure different was obtained at different extrusion conditions and found to be in good agreement with the experimental results. Pressure gradient from the flow analysis and $C$ and $n$ parameters from the shear tests were used in obtaining numerical modeling results which display shear rate and shear stress distribution in the exit of the die and compared the results with the micrographs consisting of FLs.

Flow lines were seen at low ram speeds at 338 ℃ (high viscosity) but homogeneous preforms without FLs were obtained for ram speeds 0.002 mm/s and 0.003 mm/s at 342℃. No FLs were observed in preform extruded at ram speed 0.003 mm/s at 346 ℃. A extrusion forming diagram for TZN-75 depicting the shear stress distribution for the above mentioned extrusion conditions revealed appearance of flow lines above a critical shear stress.

# CHAPTER 6

# CONCLUSIONS

In this dissertation, I find that the TZN-75 glass behaves as shear thinning liquid at high shear rates and its flow behavior can be described using power law with the power law index equal to 0.7±0.1. In extrusion, the glass experiences highest shear near the die wall and mandrel surface, shearing successive layers of glass against one another and resulting in the formation of flow lines at these interfaces. Preforms extruded at elevated temperatures (342 and 346°C) exhibited no flow lines while the ones extruded at lower temperatures (338°C and below) exhibited FLs even at very low ram speeds. FLs increase in number with increasing load and ram speed. FLs are eliminated by increasing the extrusion temperature from 338 to 342 and 346°C. Beyond 355°C ($\eta < 10^6$ Pa.s), the glass has much higher fluidity and therefore the preform elongates distorting its geometrical features and dimensional accuracy.

Formation of FLs is linked to the shear stress exceeding the critical shear stress limit for the TZN-75 glass at particular extrusion temperature, as determined by comparing the numerical model with the rheological test results. The extrusion forming diagram of shear stress distribution for the TZN-75 glass obtained from the numerical model becomes a useful tool showing the range of values of the extrusion parameters that would produce extruded preforms free of FLs. Such performs should result in fibers with much lower loss and better propagation characteristics.

## 6.1    Future Work

- Die geometry was simplified. Immediate future plans include developing a numerical model for a short die with large taper. Also, include plan in the model for the complexity of the longitudinal profile of the die.

- Extend modeling results to holey fiber preform extrusion.

- Mechanism of flow lines formation can be studied at microscopic level using different glass compositions and may be using flow visualization technique such as Particle Image Velocimetry (PIV) to understand the glass behavior in real time.


## ACKNOWLEDGMENTS

# REFERENCES

1.  Marjanovic, S., Toulouse, J., Jain, H., Sandmann, C., Dierolf, V., Kortan, A.R., Kopylov, and A. N., R.G.,, *Characterization of new erbium-doped tellurite glasses and fibers.* Journal of Non-Crystalline Solids, 2003. **322**(1-3): p. 311-318.
2.  Mori, S., Ohishi, Y., Sudo, S.,, *Er doped tellurite glass fiber laser and amplifier.* Electronics Letters, 1997. **33**(10): p. 863-864.
3.  Lin, A., et al., *Solid-core tellurite glass fiber for infrared and nonlinear applications.* Opt Express, 2009. **17**(19): p. 16716-21.
4.  Ebendorff-Heidepriem, H., T.M. Monro, *Progress in the fabrication of soft glass microstructured optical fibres with complex and new structures.* ACOFT/AOS Proceedings, 2006: p. 69-71.
5.  Ryasnyanskiy, A., Lin, A., Belwalkar, A., Guintrand, C., Biaggio, I., Toulouse J., *Nonlinear frequency conversion in bismuth-doped tellurite suspended core fiber.* Optics Communications, 2011. **284**: p. 3977-3979.
6.  Monro, T., H. Ebendorff-Heidepriem, , *Progress in microstructured optical fibres.* Annual Review of Materials Science, 2006.
7.  Ebendorff-Heidepriem, H., , *Extrusion of complex preforms for MOFs.* optical express, 2007. **15**(23): p. 15086-15092.
8.  Ravi Kanth Kumar, V.V., A. K. George, W. H. Reeves, J. C. Knight, P. St. J. Russell, *Extruded soft glass photonic crystal fiber for ultrabroad supercontinuum generation.* Optics Express, 2002. **10**(25): p. 1520-1525.
9.  Kiang, K.M., K. Framption, T. M. Monro, R. Moore, J. Tucknott, D. W. Hewak, D. J. Richardson, H. N. Rutt, *Extruded singlemode non-silica glass holey optical fibres.* Electronics Letters, 2002. **38**(12).
10. Petropoulos, P., H. Ebendroff-Heidepriem, V. Finazzi, R. C. Moore, K. Framption, D. J. Richardson, T. M. Monro, *Highly nonlinear and anomalously dispersive lead silicate glass holey fibers.* Optical Express, 2003. **11**(26): p. 3568-3573.
11. Ravi Kanth Kumar, V.V., A. K. George, J. C. Knight, P. St. J. Russell, *tellurite photonic crystal fiber.* Optics Express, 2003. **11**(20): p. 2641-2645.
12. Xiao, H., *Relationship between Process Parameters and Physical Properties of Optical Tellurite Glass Fiber Preforms Fabricated by Extrusion*, in *Material Science and Engineering*. 2007, Lehigh University.
13. *PROPAGATION OF LIGHT ALONG A FIBER* Wikipedia ,
14. Loucks, R., *Glass relaxation course*. 2010.
15. Braglia, M., C. Bruschi, D. Cavalli, G. Cocito, D. Guojun, J. Kraus, S. Mosso, *Rheology of fluoride glasses.* Journal of Non-Crystalline solids, 1997. **213 & 214**: p. 325.
16. Wikipedia *Tellurium oxide.* ,
17. Kozhukraov, V., Burger, H., Neov, S., Sizhimov B., Polyhedron, 1986. **5**(771).
18. Sakida, S., Hayakawa, S., Yoko T., Journal of Non-Crystalline Solids, 1999a. **243**(13).
19. Wang, J., *Glass viscosity and structural relaxation by parallel plate rheometry using a thermo-mechanical analyser.* Mater. Lett., 1997. **31**: p. 99-103.

20. Delben, J.R.J., A.A.S.T. Delben, S. L. Oliveira, Y. Messaddeq, *A viscosity model for fluorochloroindate glasses.* Journal of Non-Crystalline solids, 1999. **247**: p. 14.
21. Yakakind, A., N. Ovcharenko, D. Semenov, Opt. Mech. Prom., 1968. **35**: p. 34.
22. Tatsumisago, M., S. Lee, T. Minami, Y. Kowada, *Raman spectra of TeO2-based glasses and glassy liquids: local structure change with temperature in relation to fragility of liquid.* Journal of Non-Crystalline solids, 1994. **177**: p. 154.
23. Hieber, C.A., and H.H. Chiang, *Shear rate dependence modeling of polymer melt viscosity.* Polym. Eng. Sci., 1992. **32**(14): p. 931-938.
24. Aho, J., and S. Syrjala, *On the measurement and modeling of viscosity of polymers at low temperatures.* Polym. Test., 2007. **27**: p. 35-40.
25. Dyre, J.C., *Source of non-Arrhenius average relaxation time in glass-forming liquids.* J. Non-Cryst. Solids, 1998. **235**(237): p. 142-149.
26. Varshaneya, A., *Fundamentals of Inorganic Glasses*. 2006, Sheffield: Society of Glass Technology.
27. Bourhis, E., *Glass Mechanics and Technology*. 2007, Weinheim: Wiley-VCH. 90.
28. Sehgal, J., J. Non-Cryst. Solids, 1999. **253**: p. 126.
29. Kiczenski, T.J., E. Hammarsten, D. Wilkerson, M. Affatigato, and S. Feller, *A study of selcted physical properties of alkali germanate glasses over a wide range of composition.* J. Non-Cryst. Solids, 2000. **272**(1): p. 57-66.
30. Wright, B.M., and J.E. Shelby, *Phase separation and the mixed alkali effect.* Phys.Chem.Glasses, 2000. **41**(4): p. 192.
31. Angell, C.A., K.L. Ngai, G.B. McKenna, P.F. McMillan, and S.W. Martin, *Relaxation in glass forming liquids and amorphous solids.* J. Appl. Phys., 2000. **88**(6): p. 3113.
32. Webber, P.J., and J. A. Savage, *Measurement of the viscosity of chalcogenide glasses by a parallel plate technique.* J. Mater. Sci., 1981. **16**: p. 763-766.
33. Braglia, M., S. Mosso, G. Dai, E. Billi, L. Bonelli, M. Baricco, and L. Battezzati, *Rheology of tellurite glasses.* Mater. Res. Bull., 2000. **35**: p. 2343-2351.
34. Chenxu, Y., Sundaram, G.,, *Correlation of dynamic and steady flow viscosities of food materials.* Applied rheology, 2001. **11**(3): p. 134-140.
35. Tatsumisago, M., T. Minami, Y. Kowada, and H. Adachi, *Structural change of rapidly quenched binary tellurite glasses with composition and temperature.* Phys.Chem.Glasses, 1994. **35**(2): p. 89-97.
36. Komatsu, T., R. Ike, R. Sato, and K. Matusita *Mixed alkali effect in tellurite glasses and change in fragility.* Phys. Chem. Glasses, 1995. **36**(5): p. 216-221.
37. Ding, Y., V. N. Novikov, and A. P. Sokolov, *Influence of molecular weight on fast dynamics and fragility of polymers.* Macromolecules, 2004. **37**: p. 9264-9272.
38. Belwalkar, A., Xiao, H., Misiolek W. Z., Toulouse Jean, *Extruded tellurite glass optical fiber preforms.* Journal of Materials Processing Technology, 2010. **210**: p. 2016-2022.
39. Srinivasan, R., Gunasekara, J.S., Gegel, H.L., Doraivelu, S.M., *Extrusion through controlled strain rate dies.* Journal of Materials Shaping Technology, 1990. **8**: p. 133-141.

40.     Lu, J., *Deformation behavior of the Zr41.2Ti13.8Cu12.5Ni10Be22.5 bulk metallic glass over a wide range of strain-rates and temperatures.* Acta Materialia, 2003. **51**: p. 3429-3443.

41.     Belwalkar, A.A., W. Z. Misiolek, J. Toulouse, *Viscosity of the optical tellurite glass: 75TeO2-20ZnO-5Na2O.* Journal of Non-crystalline Solids, 2010. **356**: p. 1354-1358.

42.     Feng, X., Montro, T., Finazzi, V., Moore, R., Framption, K., Petropoulos, P., Richardson, D., *Extruded singlemode, high-nonlinearity, tellurite glass holey fibre.* Electronics Letters, 2005. **41**(15).

43.     Fenner, R., *Principles of polymer processing*.

# BIOGRAPHICAL SKETCH

**Author:**          Amit Ajit Belwalkar

**Degree:**          PhD candidate in Mechanical Engineering and Mechanics

**Date:**          September 2011

**Date of Birth:**          January, 1980

**Place of Birth:**          Mumbai, India

**Undergraduate and Graduate Education:**

- Doctor of Philosophy in Mechanical Engineering
  Lehigh University, Bethlehem, PA,  September 2011

- Master of Engineering in Mechanical Engineering
  Widener University, Chester, PA, 2006

- Bachelor of Engineering in Mechanical Engineering,
  University of Mumbai, India, 2001

**Major:**          Mechanical Engineering

**Vita:**

After graduating from University of Mumbai in 2001, Amit Belwalkar worked as a piping stress analyst at Toyo Engineering India Limited for one year. He decided to pursue further education and came to Widener University, Chester, PA for Master's degree in Mechanical engineering where he worked under the guidance of Prof. Zhongping Huang on nanoporous membrane for biofiltration applications. While finishing his Master's degree, he interned at Southco Inc. as a design draftsperson. After successfully finishing the Master's degree, Amit decided to pursue a doctorate degree in the same field and enrolled at Lehigh University under the guidance of Prof. Wojciech Misiolek. For the first year, Amit worked as an intellectual property business analyst at Small Business Development Center at Lehigh University. After finishing the biomembrane project, Amit joined the group of Prof. Toulouse at the beginning of year 2008 in the Physics department. Since then, he worked on the research involving improving the glass extrusion technology to make better quality preforms for enhancing the performance of tellurite glass optical fibers.